# Sustainable Manufacturing of Carbon Nanomaterials for Energy Storage Applications

By

Anna Douglas

Dissertation

Submitted to the Faculty of the

Graduate School of Vanderbilt University

in partial fulfilment of the requirements

for the degree of

DOCTOR OF PHILOSOPHY

in

Interdisciplinary Materials Science

May 10, 2019

Nashville, Tennessee

Approved:

Cary Pint, Ph.D.

Rizia Bardhan, Ph.D.

Douglas Adams, Ph.D.

Greg Walker, Ph.D.

Jason Valentine, Ph.D

ACKNOWLEDGEMENTS

I would like to first and foremost thank my advisor, Dr. Cary Pint for patiently and deliberately teaching me to be the researcher and entrepreneur I am today. Your passion for solving important and real challenges with bold and exciting new ideas is inspiring. Thank you for encouraging me towards an entrepreneurial path and for walking the start-up journey with me. I truly would not be where I am today without you, and I am so very grateful for all your efforts and guidance throughout the last 5 years. Further, I would like to thank the members of my dissertation committee including Dr. Rizia Bardhan, Dr. Douglas Adams, Dr. Greg Walker, and Dr. Jason Valentine for agreeing to give their time towards the improvement of my work and for their insightful comments.

I would like to thank members of the Pint lab, past and present, who have greatly enhanced my graduate study experience through stimulating scientific discussions, experimental guidance and contributions, and dear friendship throughout my time at Vanderbilt. To Dr. Rachel Carter, Dr. Mengya Li, and May Ou – one of the greatest treasures of the last 5 years has been your steadfast friendship and encouragement. It has most certainly shaped the way I view work, life, and the balance of it all. I'd like to extend many thanks to Dr. Rachel Carter for training me in the laboratory, setting an example of a scientific leader I aspire to be like, and for becoming one of my very best friends; to Dr. Mengya Li for the most satisfying reaction to any scenario and continued companionship in Knoxville; and to May Ou for her intentionality and the most welcoming couch in Nashville to crash on these last 2 years. I'd like to specifically thank the levitating frog problem for catalyzing my friendship with Dr. Nitin Muralidharan. Further, my graduate studies wouldn't have been the same without my colleagues Dr. Landon Oakes, Dr.

Andrew Westover, Dr. Adam Cohn, Dr. Keith Share, Deanna Schauben, Kate Moyer, Janna Eaves, John Waugh, Murt Zohair, and the undergraduate students I've been privileged to mentor including Siyuan (Dominic) Jiang and Katie Hornbeck.

I would like to graciously thank Dr. Rizia Bardhan and all of the Bardhan group members for generous use of their laboratory instruments and space for synthesis experiments, and to Sarah Ross, Dr. Dmitry Koktysh, Dr. Anthony Hmelo, Dr. Alice Leach, and all the VINSE staff who have been tremendously gracious with their time and efforts.

I also want to express my sincere thanks to our collaborators at Oak Ridge National Laboratory including Dr. Dave Geohegan, Dr. Ilia Ivanov, Dr. Chris Rouleau, Dr. Alex Puretzky, Dr. Gyula Eres, Dr. Dale Hensley, Michael Pannell, and Anna Klug for welcoming me into your group, sharing your laboratory space, and for all your help and efforts over the last 2 years. I would also like to thank the Innovation Crossroads team who have extended valuable support including Tom Rogers, Kelly Wampler, Dr. Beth Connerty, Dan Miller, and Dr. Gary Rawlings.

Further, I would like to acknowledge all of the teachers and mentors who have guided me to this point in my life. I wouldn't be in this position today if it weren't for the efforts of my mentors recognizing a scientific passion in myself and encouraging and supporting that passion. I'd like to specifically thank Dr. Johnny Evans and Dr. Laura Singletary for being dear mentors during my time at Lee University and for always believing in my potential, and I'd also like to extend sincere thanks to Dr. Mary Ann Meador for taking a chance on me to do chemistry and materials research in her group at NASA Glenn when up to that point I had only mathematical training. The efforts of my mentors and teachers have been a great source of strength throughout my academic journey to this point, for which I am eternally grateful.

I could not have completed my research without generous funding support from the NSF Graduate Student Research Fellowship, DOE Entrepreneurial Fellowship, and Sandberg Stichting Foundation – I am so very grateful for this support which has allowed me to study and research projects I am so passionate about.

I would like to extend heartfelt thanks to my parents, Hugo and Kathy Sandberg, for their support in every aspect and at every stage of my life. I would not be who I am today without your unconditional love and encouragement. To my siblings, Aaron and Molly Sandberg – thank you for pushing me to be my best but always loving me regardless.

Finally, I would like to deeply and sincerely thank my best friend, teammate, confidant, and my one true love. Scott, you have traveled this journey alongside me for the last 5 years and done everything you can to encourage and support me. Thank you for accompanying me to late-night and weekend lab visits and being a true partner at home – your understanding and tender spirit in seasons of ups and downs have truly carried me. Thank you for your flexibility, adaptiveness, and willingness to go wherever this adventure takes us. Over 3 years ago we vowed that where there is love, nothing is too much trouble, and there is always time. I could not be more grateful to you for living this truth every day.

TABLE OF CONTENTS

Page

LIST OF FIGURES

Page

# LIST OF PUBLICATIONS

Portions of this dissertation have been drawn from the following publications:

1. **A. Douglas**, R. Carter, L. Oakes, K. Share, A.P. Cohn, and C.L. Pint, "Ultrafine iron pyrite ($FeS_2$) nanocrystals improve sodium-sulfur and lithium-sulfur conversion reactions for efficient batteries," ACS Nano 9, 11156-11165 (2015)

2. **A. Douglas**^, N. Muralidharan^, R. Carter, K. Share, and C.L. Pint, "Ultrafast triggered transient energy storage by atomic layer deposition into porous silicon for integrated transient electronics," Nanoscale 8, 7384-7390 (2016) (^equal contributing first authors)

3. S. Licht, **A. Douglas**, J. Ren, R. Carter, M. Lefler, and C.L. Pint, "Carbon nanotubes produced from ambient carbon dioxide for environmentally sustainable lithium-ion and sodium-ion battery anodes," ACS Central Science 2, 162-168 (2016)

4. **A. Douglas**, et al. "Stable Sodium-Ion Battery Anode Using $SnO_2$ Nanoparticles and Thin Films Confined in Porous Silicon Templated Mesoporous Carbon," *in preparation*

5. **A. Douglas**, C. L. Pint, "Electrochemical Growth of Carbon Nanotubes and Graphene from Ambient Carbon Dioxide: Synergy with Conventional Gas-Phase Growth Mechanisms," ECS Journal of Solid State Science and Technology, 6, M3084-M3089 (2017)

6. **A. Douglas**, R. Carter, N. Muralidharan, L. Oakes, C. L. Pint, "Iron catalyzed growth of crystalline multi-walled carbon nanotubes from ambient carbon dioxide mediated by molten carbonates," Carbon, 116, 572-578 (2017)

7. **A. Douglas**, N. Muralidharan, R. Carter, C. L. Pint, "Sustainable Capture and Conversion of Carbon Dioxide into Valuable Multiwalled Carbon Nanotubes Using Metal Scrap Materials," ACS Sustainable Chemistry & Engineering, 5, 7104-7110 (2017)

8. **A. Douglas**, R. Carter, M. Li, C. L. Pint, "Toward Small-Diameter Carbon Nanotubes Synthesized from Captured Carbon Dioxide: Critical Role of Catalyst Coarsening," ACS Applied Materials & Interfaces, 10, 19010-19018 (2018)

9. **A. Douglas**, K. Moyer, M. Pannell, C. L. Pint, "Electrochemical Pinning of Catalyst Particles by High Current Density to Mitigate Catalyst Coarsening," *in preparation*

10. **A. Douglas**, K. Moyer, J. Eaves, Michael Pannell, C. L. Pint, "Toward Sustainable Manufacturing of Lithium-Ion Batteries: Utilization of Carbon-Negative Carbon Nanotubes and Earth-Abundant Lithium Iron Phosphate for Low-Carbon Batteries," *in preparation*

# Chapter 1

## Introduction

### 1.1 Motivation

The rise of the industrial revolution has brought much of our modern-day necessities and luxuries, fueled by electrical power on demand. Never before in history have we experienced such a high standard of living, and we must credit the innovations developed during the industrial revolution for the technologically-mature society we live in today. However, since this time, the concentration of atmospheric carbon dioxide ($CO_{2atm}$) has been rising exponentially year after year, and the increased concentration of $CO_{2atm}$, predominantly due to anthropogenic activities such as fossil fuel consumption, challenges the promise of long-term human sustainability on Earth. The rate of increase in anthropogenic $CO_2$ emissions has more than doubled to over 2.5% from 2000–2014, compared to the previous 1.1% for the period from 1990–1999, as a result of our ever-increasing population and rising demands for energy and materials to power our standard of living.[1] If this rate of emissions remains constant over the next 40 years, the atmospheric concentration of $CO_2$ will be over double pre-industrial levels.

The effects of rising $CO_2$ levels is widespread, but includes rising sea levels that have already begun to impact communities,[2] increased severity and frequency of natural disasters,[1] acidification of oceans that threatens oceanic life and our food supply from oceans,[3] melting icecaps that impact local ecosystems,[1] and public health concerns such as increased rates of heat strokes and vector-based viruses that now have the ability to travel farther due to warmer temperatures[4]. This impact of $CO_2$ on global climate change has attracted the attention of researchers in efforts to develop

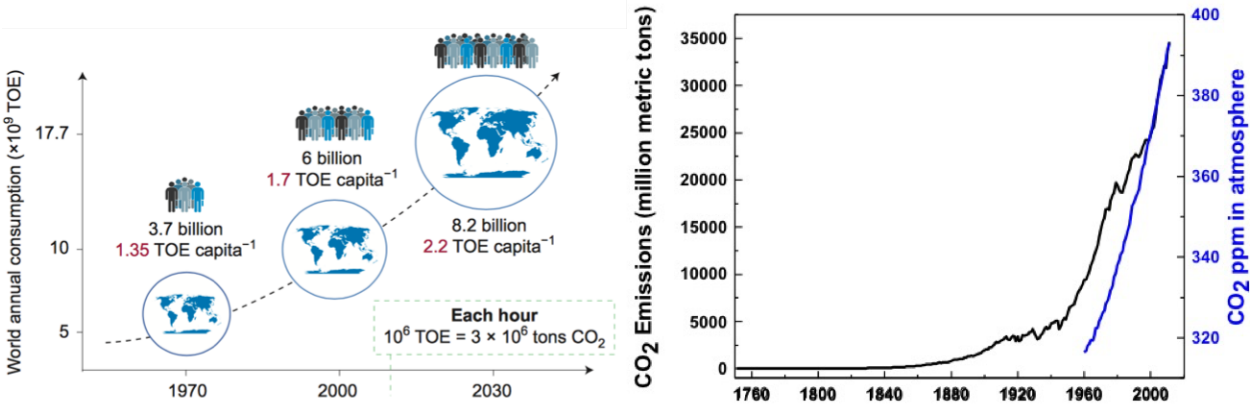


**Figure 1** left - world population growth and increased demand for energy, right - $CO_2$ emissions and $CO_2$ ppm in atmosphere. Left panel reprinted with permission from Springer

technologies that can achieve a reduction in $CO_{2atm}$ to a level of sustainability.[5-8] Renewable energy sources is one specific approach, even though for established centralized power grids, such as that in the United States, only a low abundance of intermittent energy production can be managed without a significant onboarding of grid-scale energy storage such as low-cost batteries which are today still too expensive for widespread adoption into the grid. Additionally, limitations to widely proposed carbon storage techniques include the volume of available storage sites (depleted oil and natural gas reserves) and high probability of leaks.[1]

As a result, sustaining today's modern society and standard of living has become an existential challenge that is only solved through a combined approach towards addressing the needs to (1) lower $CO_2$ and other greenhouse gas (GHG) emissions, and (2) remove existing atmospheric $CO_2$ to restore the natural balance in our ecosystem. Technological advancements in electrochemical energy storage has the capability to address the former of these through the electrification of many industries which are today powered by fossil fuels (such as the transportation industry, which today contributes ~ 28% of $CO_2$ emissions in the United states). To achieve this, lithium-ion batteries (LIBs) are poised to enable electrification due to their unmatched energy and power densities among energy storage technologies, and their applicability to a range of uses including grid-scale

energy storage (where cost drives implementation), and electric vehicles (EVs, where gravimetric and volumetric performance is a key enabler). However, cost and performance improvements to LIB technology are slowing towards their theoretical limit, motivating a significant thrust in energy storage research to develop new materials and chemistries to power us into the next wave of technological innovation. Beyond building better batteries to reduce $CO_2$ and other GHG emissions towards a net-zero emission economy model, recent reports have highlighted the critical need to also remove $CO_2$ from the atmosphere to avoid irreversible climate change in the near future.[9] To achieve this, technologies for the capture and storage of atmospheric $CO_2$ must be developed and are being actively explored by academics, government entities, and companies alike.

## 1.2 Need for better performing and more sustainable energy storage

### *1.2.1 State of lithium ion batteries*

The traditional LIB relies on a layered metal oxide cathode and a graphite anode which is separated by an electron-inhibiting, ion-conducting polymer separator immersed in an organic liquid electrolyte saturated with $Li^+$ ions. Each electrode is typically cast onto current collectors from a slurry with conductive additives and polymeric binders that support electrical conductivity and bind the materials together. The LIB is fully discharged upon fabrication, and is externally charged *via* current, where the cathode is oxidized and $Li^+$ ions are shuttled across the cell and intercalate between the carbon layers at the graphite anode. This system relies on the intercalation of $Li^+$ ions between electrodes due to their layered structures, and results in an extraordinarily high degree of stability, with commercial cells demonstrating > 15,000 cycles. However, this core

chemistry is performance-bottlenecked by the high volume expansion and significant mass required to host $Li^+$ ions through the intercalation mechanism (1 $Li^+$ stored for every 6 Carbon atoms and 1 metal oxide molecule), with many next-generation materials offering improvements in energy density through increased capacity or higher voltages. Moreover, the high cost of LIBs is primarily driven by the materials used in the active energy-storing electrodes, and with a DOE target of $125/kWh by 2020,[10] a change in materials choices is imperative. Currently used cobalt-based metal oxide cathodes have garnered recent attention due to questionable labor practices and rising prices of raw materials (which have nearly quadrupled in the last two years, from $22 to $81/kg) as a result of limited natural resources and exponentially increasing demand to supply our rising battery production.[11] Additionally, the high energy requirement to synthesize and process materials that are implemented into batteries has warranted critical assessment of cradle-to-gate life cycle analyses, which have highlighted that due to the high energy requirement to produce batteries for EVs, even under the best case scenario with zero-emissions energy sources deployed to charge EVs, the environmental benefit of switching to an EV compared to a conventional gasoline-burning engine is only realized after hundreds of cycles.[12] This, compounded with a consistent trend of rising $CO_2$ emissions from the production of batteries, results in the potential for *increased* transportation-related emissions if EV adoption growth and limited onboarding of renewables into our grid both as projected, and our LIB materials remain unchanged. Moving towards more earth-abundant and lower-cost battery materials (Figure 2) will be critical for the long-term sustainability of battery production.

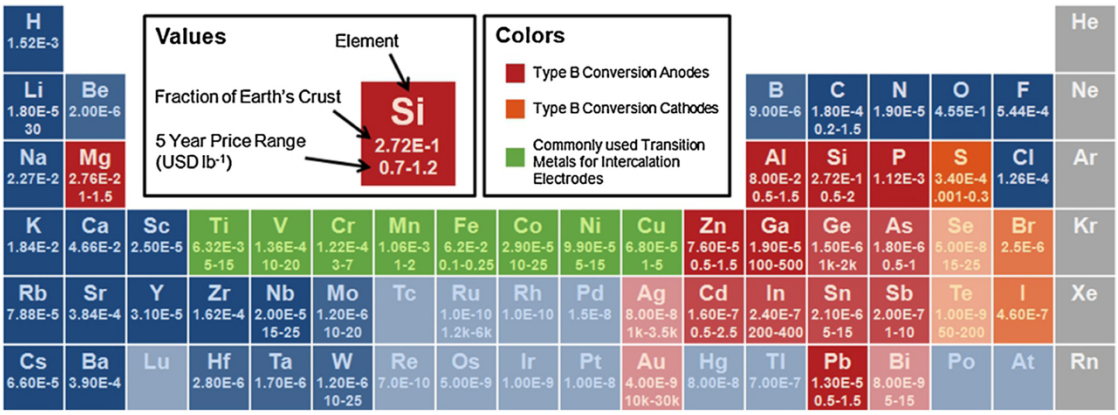


**Figure 2**. Abundance and price of elements that may host Li as electrodes. Reprinted with permission from Elsevier.

*1.2.2 Motivation for using Fe, S, Na, and $CO_2$-derived C materials in batteries*

When considering emerging beyond lithium-ion chemistries that can help address the need for materials that can store more energy per unit mass and help achieve cost, energy, and $CO_2$ footprint reductions to LIB manufacturing, sulfur-based conversion reactions stand out among promising candidates. In contrast to intercalation reactions, conversion reactions involve the chemical transformation of one or more of the atomic species into a host lattice to form a new compound. Metal sulfides exhibit conversion reactions with lithium or sodium metal atoms, and have been at the forefront of both fundamental and applied battery systems. Particularly, $FeS_2$ (pyrite, "fool's gold") is an exciting material for LIBs because of its high earth abundance, low toxicity, and low raw material cost, as it is a common by-product of coal production. It exhibits a high theoretical capacity of 894 mAh/g due to the storage of four lithium ions per $FeS_2$ via a conversion reaction that results in Fe and $Li_2S$ (or $Na_2S$ in the case of sodium storage). One exciting aspect of studying $FeS_2$ is its ability to undergo the conversion reaction with both $Li^+$ and $Na^+$ ions. This is particularly interesting as many researchers are focusing significant efforts on

studying sodium-ion batteries due to sodium's higher earth abundance and lower cost compared to lithium.[13, 14]

When considering sustainable choices for cathode materials, Fe-based materials such as $FeS_2$ and $LiFePO_4$ (LFP) stand out with extremely high earth abundancy (iron is 100X more abundant than cobalt). LFP also requires much less energy to synthesize the materials and results in less $CO_2$ and other GHG emissions when comparing to cobalt-based cathodes.[15] Despite a lower working voltage, LFP is commercially used today in LIBs and remains an exciting material from an environmental standpoint.

On the anode side, a variety of carbon-based structures have been studied in battery applications and are an exciting class of materials due to their high electrical conductivity, high surface area, tunable surface properties, low density, high earth abundance, and low cost. Beyond currently-employed graphite anodes, many nanostructured carbon materials such as graphenes and carbon nanotubes have been investigated for their use as LIB anodes, though high volume manufacturing of these materials remains a challenge in terms of cost, scalability, and environmental impact of the gas-phase processes used today to produce carbon nanomaterials.[16]

In this spirit, throughout this dissertation, we combine sustainable earth-abundant materials such as Fe, S, Na, and $CO_2$-derived C into battery materials for next-generation energy storage with the ability to lower $CO_2$ emissions associated with battery production which will be critical as we transition towards a fully electrified and renewable-energy generated economy.

## 1.3 Need for $CO_2$ capture and utilization

### *1.3.1 Introduction to $CO_2$ conversion*

To address the rising levels of atmospheric carbon, recent efforts have considered the capture of $CO_2$ from release points, such as power plants, and conversion into chemicals including formic acid, methanol, CO, and ethylene.[17] In this technique, $CO_2$ acts as the chemical feedstock for the manufacturing of useful chemicals and provides the potential for a viable secondary market for otherwise pollutant gases, which are normally expensive to sequester. However, these routes for $CO_2$ conversion are bottlenecked by the cost of operation versus the perceived economic benefit to society, and these low-value materials produced at low efficiencies, often from expensive catalyst materials, undermine the rationale of this approach. These issues can be resolved with the development of techniques that capture and convert atmospheric $CO_2$ into more valuable materials that can be developed into high-value products.

As $CO_2$ is the most oxidized form of carbon, no natural chemical destruction mechanism exists for the decomposition of $CO_2$. In contrast to the hydrogenation of $CO_2$ into hydrocarbons and alcohols, liquid-phase electrochemical splitting of $CO_2$ into its individual elemental constituents has been investigated beginning with aqueous electrolytes. However, low solubility of $CO_2$ in aqueous solution and similar reaction potentials for water splitting were problematic. $CO_2$ splitting in room temperature ionic liquids (RTILs) has been studied for their attractive electrochemical window and high solubility of $CO_2$, but the high cost and toxicity of RTILs makes their commercial adoption impractical.[18] In contrast to these methods, molten carbonates boast low cost and high ionic conductivity with a low vapor pressure, and have been proven as viable

electrolytes for the capture and electrochemical splitting of $CO_2$ dating back now seven decades.[19] This method relies on the decomposition of dissolved $CO_2$ between two biased electrodes, where elemental carbon is captured at the cathode, and the resulting structures of the deposited carbons are largely dependent on process parameters including electrolyte, current density, and electrode materials.[20-26] The equations that govern this process are:

$$Li_2CO_3 \rightarrow Li_2O+C+O_2 \quad [1]$$

$$Li_2O+C_2O \rightarrow Li_2CO_3 \quad [2]$$

The net equation from equations 1 and 2 is:

$$CO_2 \rightarrow C+O_2 \quad [3]$$

*1.3.2 Carbon nanomaterials and $CO_2$ conversion*

Among naturally occurring elements, carbon is one of the most widely used in modern technological applications. Carbonaceous materials including activated carbons, graphite, carbon black, and biomass are used extensively in chemical production,[27] electricity generation,[28] fuel production,[28] and in the construction of energy storage devices including lithium-ion batteries and supercapacitors.[29, 30] The last 25 years have been lauded as perhaps the most exciting for carbon researchers due to the emergence of nanostructured carbon materials with extraordinary mechanical, thermal, and electronic properties that cannot be replicated in other known materials. This era began with the discovery of $C_{60}$ fullerene in 1985 and resulting Nobel Prize awarded to Curl, Kroto, and Smalley. Further, this was continued as the emergence of graphene led to the 2010 Nobel Prize awarded to Geim and Novoselov elucidating the global excitement for these materials. Shown in Figure 3, nanostructured carbons including fullerenes, carbon nanotubes (CNTs), and graphene are all based on the same hexagonally arranged carbon unit that is either

rolled or planar. Since their 1991 discovery by Ijima,[31] CNTs are the only nanostructure that have reached large-scale industrial production, with the main consumer applications today in polymer reinforced composites for automotive, defense, and spacecraft applications.[32-34] Ongoing research for the use of CNTs for applications in medicine,[35] electronics,[32] energy storage,[36, 37] membranes for water desalination,[38] gas sensors,[39] and coatings,[40] demonstrates strong interest in these emerging sectors of CNT applications.

Specifically for CNTs, over two decades of ongoing research has revealed a series of catalytic growth and growth termination mechanisms that are to a large part understood. Concepts critical to the catalytic growth of CNTs have been highlighted as precursor chemistry,[41] catalyst composition and/or oxidation state,[42] catalyst size,[43] physical and chemical properties of catalyst supports,[44-46] growth temperature,[47-49] and physical processes during growth such as Ostwald

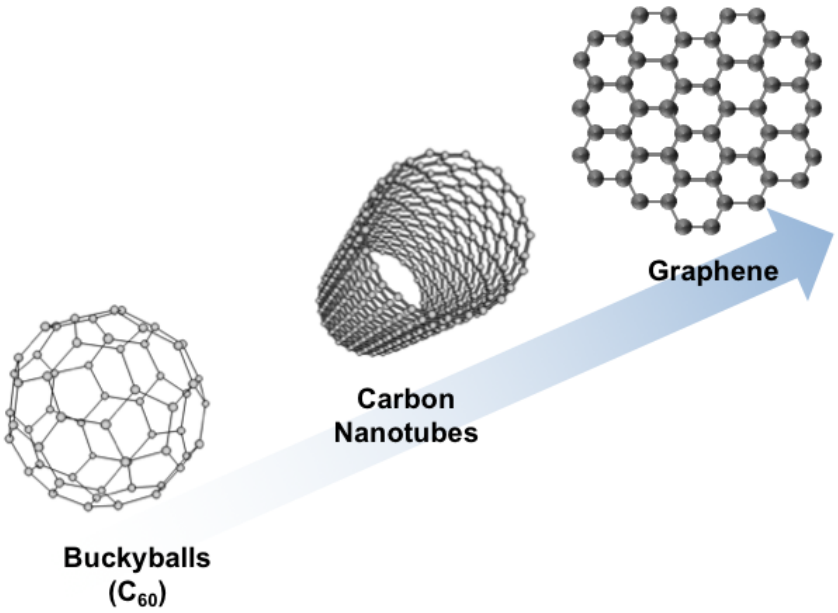


**Figure 3**. A brief schematic timeline highlighting the evolution of different carbon nanomaterials.

ripening, catalyst diffusion, and mechanically driven collective growth termination processes.[50-53]

In contrast to this mature field, the growth of carbon nanostructures from the liquid-phase electrochemical reduction of $CO_2$ remains only a new field of research, with the most recent work demonstrating growth of large-diameter (>100 nm) CNTs[54] and few-layer graphene flakes from $CO_2$ conversion.[25, 26] These initial works demonstrate the capability to leverage $CO_2$ as a precursor in carbon nanostructure growth, even though forward-looking efforts to achieve high quality, precisely tuned materials such as single-walled CNTs or single-layered graphene at high yields will require control of the process beyond the systems-level approaches reported so far. This presents an exciting frontier that exists at the intersection of these two communities – those who have studied the mechanistic details of catalytic processes relating to nucleation and growth of nanostructures, and those who are focused on systems-level directions to develop platforms which can address important global issues.

### *1.3.3 Synergy between $CO_2$ conversion and CNT synthesis*

Of the methods utilized to convert precursor gases into CNTs, including laser ablation, arc discharge, chemical vapor deposition (CVD), and flame synthesis, CVD is by far the most widely used for its versatility and simplicity.[55-59] Briefly, a hydrocarbon gas is passed over the surface of a catalytic nanoparticle (CNT) or surface (graphene) which promotes the dissociation of the gas and allows for diffusion of carbon intermediates into the metal. The particle/surface provides a nanoscale template for the precipitation of graphitic carbon, and hence the nucleation and growth of the CNT or graphene material.[59] Nickel, iron, and cobalt are specifically three of the most common catalysts for CNT growth by CVD, though over two decades of research, many other elements and elemental alloy combinations have been proven suitable.[56] At the intersection of $CO_2$ conversion and CNT growth lies the relatively unexplored field of electrolytic conversion of

$CO_2$ into CNTs, which utilizes the decomposition of $CO_2$ between two electrodes, where elemental carbon is captured at the cathode and can be utilized to grow specific nanostructures depending on the surface of the cathode. We observe that the role of catalytic behavior is critical in both electrochemical conversion of $CO_2$ and gas-phase growth of CNTs, and the only discussion so far on growth of CNTs from $CO_2$ indicate that this process is also driven by catalytic processes.[54, 60] Notably, the electrodes are comprised of bulk conductive materials that contain all of the primary catalyst materials used in gas phase CNT growth studies, but efforts have yet to isolate correlations between catalyst properties and CNT growth characteristics. Moving forward toward using electrochemical $CO_2$ splitting for the highly efficient growth of precisely tuned carbon nanostructures is likely to greatly rely on the ability to merge fundamental growth mechanisms by researchers in the carbon synthesis community with the new challenges that arise for growth at a solid-liquid interface in an electrochemical system.

The structural characteristics of CNTs grown by CVD methods strongly depend on the experimental conditions under which they are prepared, including catalyst properties such as size,[61, 62] composition,[42, 63-66] reduction techniques,[56, 67] migration and particle ripening,[50-53] and catalyst support layers;[44-46] and global parameters such as time,[56] temperature,[47-49] and rate of carbon source.[56] These are shown in Figure 4.

Whereas many of the structural effects of these parameters are well understood in gas-phase CNT synthesis methods, they are virtually unexplored in the liquid-phase $CO_2$ electrolysis for CNT growth. For example, a strong correlation between the size of the catalyst particles used in CVD and the diameter of the resulting CNTs is often observed and has been studied with *in-situ* TEM techniques.[68-70] This understanding has been the basis of controlling the size distribution

of the catalyst particles as the most standard way to tune the CNT diameter distribution, which is

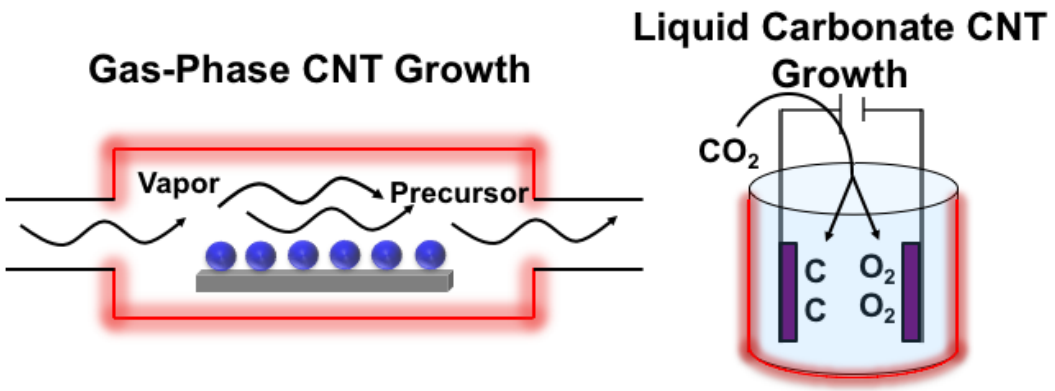


| Growth Parameters | CVD gas-phase | Carbonate liquid-phase |
|---|---|---|
| Carbon flux | Gas flow rate<br>Effects catalyst poisoning | Current density<br>??? |
| Time | CNT yield | CNT yield<br>Quality? |
| Catalyst diameter | CNT diameter | ??? |
| Catalyst reduction | Yield/quality | ??? |
| Ostwald ripening | 2-dimensions | 3-dimensions? |
| Catalyst materials | Diameter<br># of walls | ??? |
| Temperature | Carbon solubility in metal | C or CO deposition |
| Substrate and support | CNT length | Must conduct $e^-$ |

**Figure 4**. Schematic illustration of gas-phase CNT growth and liquid carbonate CNT growth with a table of parameters that influence CNT growth with correlation to each technique.

most commonly achieved by tuning the thickness of the deposited catalyst, the coarsening rate, or its evaporation during thermal treatment processes prior to growth.[55] While we anticipate a similar trend to carry over into the liquid-phase growth process and likely be accelerated by the liquid phase medium, such effects remain fully unknown about this new system. Further, dynamic processes of catalysts have demonstrated that in two dimensions across the surface of the growth support, the high surface free energy of metal nanoparticles will instigate Ostwald ripening and catalyst coarsening.[50-53] Similarly, in molten carbonate (melting point ~ 750°C) electrochemical growth takes place at a similar temperature as gas phase processes, but mechanisms such as

Ostwald ripening will now occur at the solid-liquid interface, instead of the solid-gas interface, yielding intriguing new roles for well-studied and characterized mechanisms.

Similar to catalyst size, catalyst composition is well known to dictate the carbon diffusion through the metal nanoparticle, and result in dictating the number of walls and diameter of resulting CNT structures. The ability of transition metals to bond with carbon atoms increases with the number of unfilled d-orbitals, and thus metals without d-vacancies in their electron configuration display a negligible affinity for carbon. Metals with few d-vacancies such as Ni, Fe, and Co exhibit finite carbon solubility, which makes them ideal candidates for CNT catalysts.[55] It is generally accepted that small diameter iron catalysts are the most ideally suited for growth of small diameter single-walled CNTs, due to their unique carbon diffusion properties.[58] Once again, as the electrochemical processes often employed for carbon growth rely on (conductive) metal electrodes, often composed of Fe-rich steels, nickel, or other metals, this presents an opportunity to understand how metal nanoparticles can form at the solid-liquid interface and evolve over time to enable CNT growth. Similarly interesting is the reduction processes in electrochemical growth, since catalyst reduction with $H_2$ in the gas phase prior to CNT or graphene growth is a critical step to achieve high quality materials. Until now, researchers employing electrochemical methods to grow a broad range of carbon nanomaterials have carried out no notable microscopic investigation of the substrate properties that can be correlated with nucleation and growth of the carbons and answer these questions for electrochemical growth processes. This is an exciting area to explore, and provides a direct connection between traditional gas-phase CNT growth and electrochemical growth techniques.

Whereas catalytic properties are some of the most influential parameters affecting CNT growth, global parameters such as time, temperature, carbon flux, and substrate choices can also

have a large role in the structural properties of the CNTs produced. For example, carbon flux in traditional gas phase CNT growth processes is controlled by the partial pressure and flow rate of carbon precursors in the reaction system, whereas in liquid phase growth it is controlled by the current density, which dictates the rate of $CO_2$ splitting between electrodes. The development of models, such as the Puretzky model,[49] to study the relationship between carbon flux, diffusion and precipitation, and effects of catalyst poisoning under conditions of high carbon flux have led to a mechanistic understanding of the influence on gas-phase CNT growth, however this remains a new and interesting idea for electrolytic growth of CNTs. As carbon solubility is a function of temperature, gas phase processes are greatly influenced by the system temperature. For example, the solubility of carbon in iron at 700°C is ~0.1 at.%, whereas at 800°C it is ~4 at.%.[55] However in liquid phase $CO_2$ reduction, as observed theoretically[71] and experimentally[24] in many studies of temperature effects in $CO_2$ electrolysis, the deposition of C is favored below 950°C, above which CO is preferential. In this new CNT growth mechanism, the global parameter of temperature not only likely influences carbon solubility into catalyst particles, but dictates the chemical species which is deposited at the cathode altogether. As time of growth increases in both CNT synthesis techniques, CNT yield increases. Some studies using electrochemical growth processes have speculated on the role of time on synthesis products,[72] but careful time-dependent studies are critical in characterizing the electrode-catalyst-carbonate interface evolution and its impact on the growth. On a similar note, whereas many studies of gas phase CNT growths have focused on the effect of substrate and catalyst support materials,[45] no work has looked at the effect of different substrates for liquid carbonate $CO_2$ electrolysis growth. In fact, the most traditionally utilized substrate for gas phase growth, silicon, corrodes in molten carbonate electrolytes and thus alternative substrates are necessary. The biggest qualification a substrate must demonstrate to be

suitable for liquid-phase CNT growth are conductivity and chemical stability within the molten carbonate electrolyte.

*1.3.4 Towards structural control of electrochemical CNT growth*

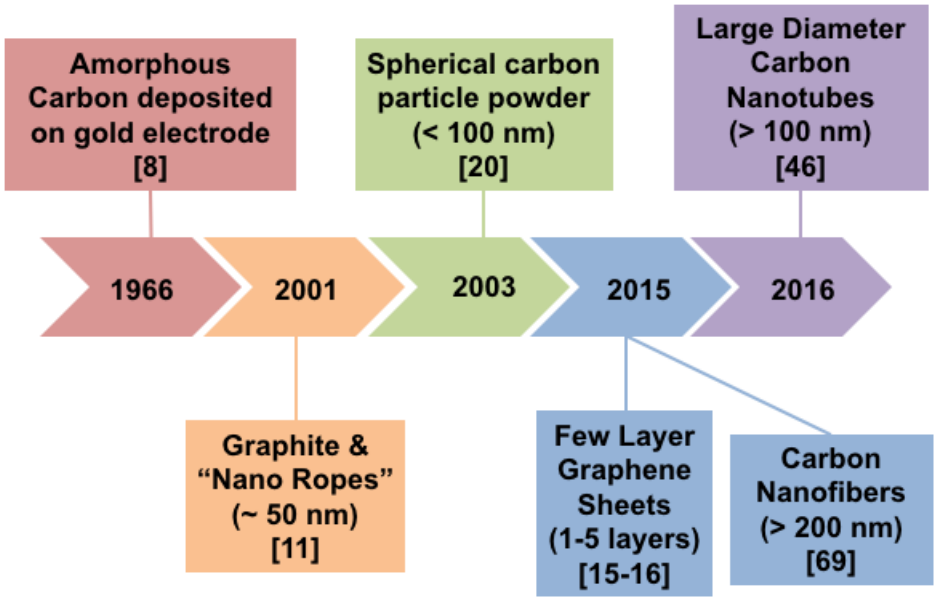


**Figure 5**. Schematic showing a timeline of CO2-derived carbon nanostructures ranging from the discovery of the general process (1966) to the most recent discovery of large diameter CNTs, few layer graphene sheets, and carbon nanofibers growing using this technique.

A brief timeline for the history of structures produced through $CO_2$ electrolysis is given in Figure 5, with corresponding SEM images in Figure 6. The first report of carbon deposition via $CO_2$ electrolysis in fused molten carbonates in 1966 resulted with a thin layer of structurally uncharacterized carbon deposited onto cathodes of gold, palladium, platinum, silver, and stainless steel.[19] This carbon was likely structurally similar to the spherical carbon powders observed in 2003, and shown in Figure 6a, consisting of carbon particles ~100 nm.[30] However, 2001 marks the first observation of carbon deposits which structurally resemble the extraordinary nanocarbons

grown from gas phase and studied today, with the observation of graphite (Figure 6b) and "nano ropes" (Figure 6c) of ~50 nm by Kaplan *et. al.*[73] The authors comment that the observed "nano ropes" are parallel carbon nanofibers bound together, though speculation of how the different carbon nanostructures are formed in electrolysis is not detailed in the report. In more recent years, the observation of higher quality carbon nanostructures has been studied, with the growth of few-layer graphene sheets (<5 layers)[25, 26] (Figure 6d) and carbon nanofibers with diameters >200 nm (Figure 6e)[60] in 2015, and more recently carbon nanotubes with diameters >100 nm (Figure 6f)[54] in 2016. These works begin to build upon mechanistic understandings gained from gas phase growth techniques, and start to bridge the gap between gas phase growth of carbon nanostructures and $CO_2$ electrolysis. The growth of CNTs and nanofibers has been carried out utilizing a corrosive Ni anode, and in this system it is presumed that the corrosion of the Ni is the basis for the catalyst. However, while these works demonstrate the promising intersection between traditional gas phase synthesis concepts and electrochemical growth techniques, further efforts to achieve the growth of high quality structures including small-diameter and single-walled CNTs, single layer graphene, and vertically aligned CNTs through the electrolysis of $CO_2$ will require future efforts that forge a distinct interface between these two growth processes.

Figure 7 illustrates the current state of carbon structures grown from $CO_2$, including large diameter multi-walled CNTs >100 nm in diameter, and few layer graphene sheets 1–5 layers thick. As modern society is tasked with the challenge of finding technologies for $CO_2$ sequestration to reduce the threat of global climate change, the most economically viable solution is the utilization of $CO_2$ as chemical feedstock for the production of high-value materials which can be utilized in

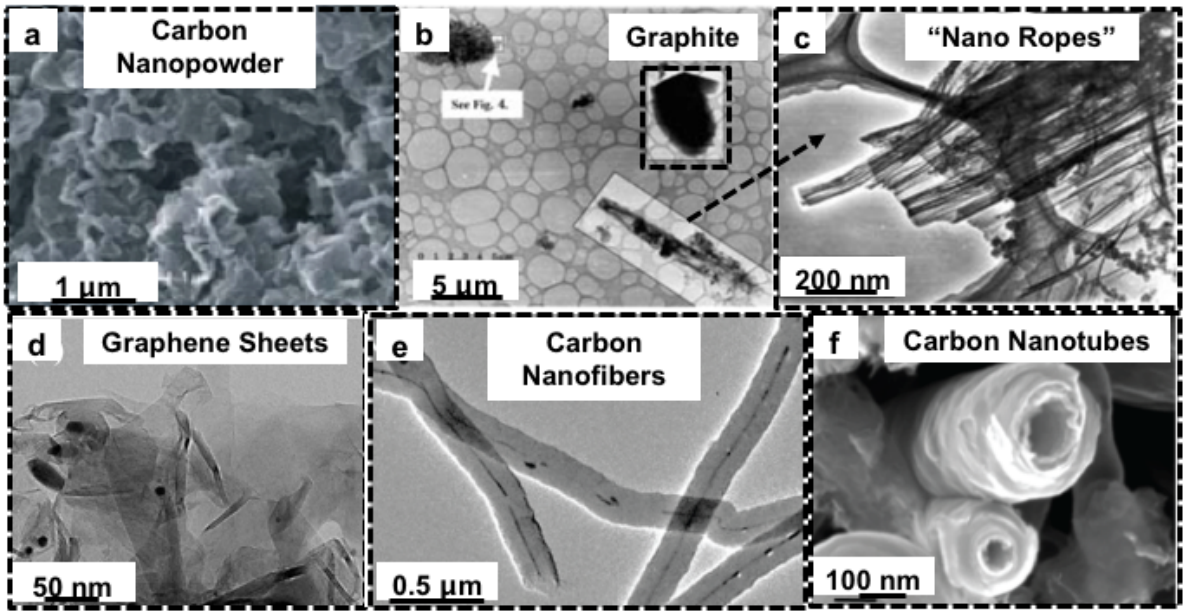


**Figure 6**. SEM and TEM images showing CO2-derived carbon nanostructures including a) carbon nanopowder, b) graphite, c) "nano ropes," d) graphene sheets, e) carbon nanofibers, and f) carbon nanotubes.

a variety of modern consumer applications. We envision the ability to leverage the understanding from decades of CNT growth, applied to this system, in order to achieve carbon structures grown from $CO_2$ that have extremely high technological relevance, including single layer graphene, single-walled CNTs, and vertical CNT arrays.

*1.3.5 Impact of $CO_2$-derived carbon nanomaterials*

Achieving the electrolytic growth of these structures at the beginning of their widespread commercial adoption provides a route toward $CO_2$-negative manufacturing of applications that are based on these carbon nanomaterials. Such applications can include structural composites for clean energy applications such as wind turbines, lightweight materials ideally suited for aircraft, spacecraft, and even sporting equipment, and energy storage applications including batteries and supercapacitors. A CNT or carbon sequestration researcher may naturally approach this vision

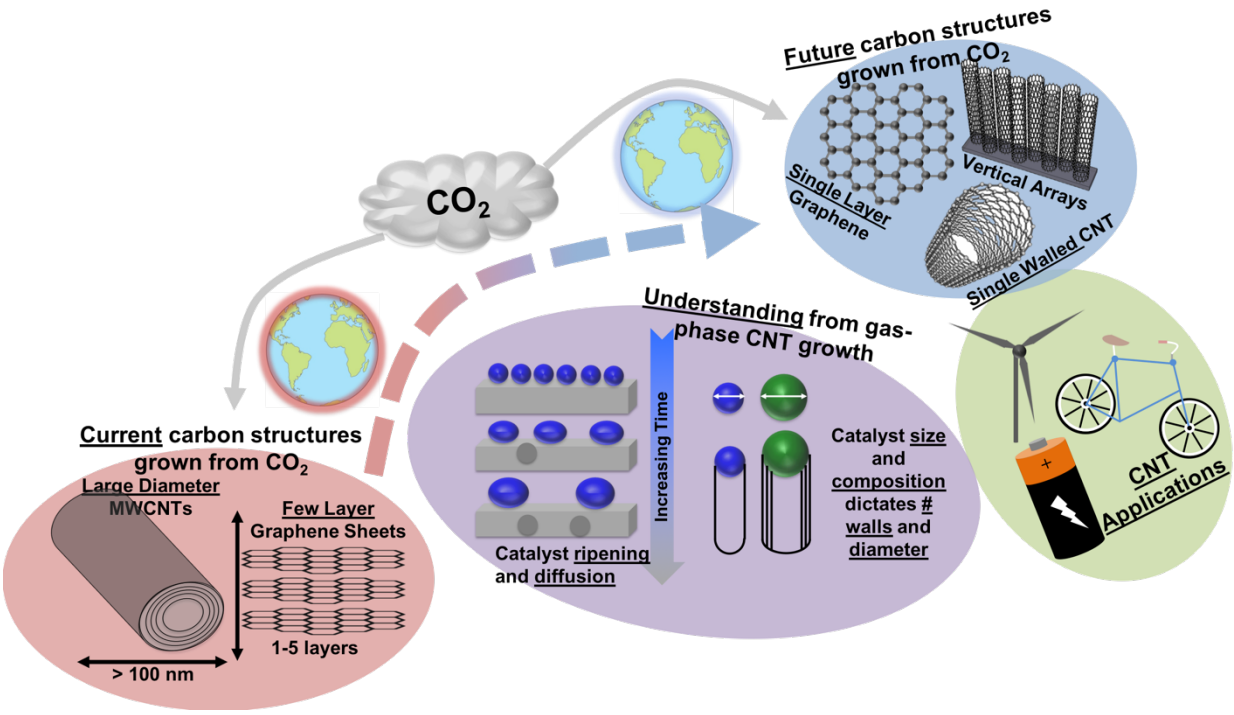


**Figure 7**. Schematic illustration showing the current types of carbon nanostructures grown from CO2 and how bridging an understanding from gas-phase CNT growth to this technique can enable highly controlled carbon nanomaterials such as single-walled CNTs and single-layer graphene, which can be used in high performance applications

with some skepticism, noting the disparity between the small size of the market for carbon nanostructured materials versus the vast amount of carbon which has been emitted into our atmosphere and resides in the form of $CO_2$. One may argue that the modest research efforts of a few passionate scientists are not likely to *solve* the climate change problem from materials produced in the laboratory. However, we argue that two important scenarios give true meaning to the vision of this approach.

First, if the estimated market figures for five key carbon products: graphene, carbon fibers, CNTs, activated carbon, and carbon black, are individually normalized by their average selling prices, we can estimate a total mass of carbon from these materials that is currently manufactured into various applications. The electrochemical conversion of $CO_2$, which can allow for the production of these carbon materials using recycled carbon dioxide, would result in a net reduction

of annual carbon emissions in the United States by an estimated ~5%. We estimate this based on the projected market sizes and average selling prices for carbon fiber ($7.51 Billion, $10/lb),[74] CNTs ($8.1 Billion, $10/gram),[75] carbon black ($28.05 Billion, $560/lb),[76] graphene ($2.1 Billion, $2.50/gram),[77] and activated carbon ($10.15 Billion, $350/ton),[78] and use these figures to estimate a total mass of carbon that is manufactured into various applications. If we replace currently employed manufacturing techniques to utilize electrochemical conversion of $CO_2$ to produce these five key carbon structures using wasted $CO_2$ as the chemical feedstock, we can estimate the amount of $CO_2$ captured from the atmosphere for this manufacturing, and calculate an estimated net emissions reduction.

Secondly, if visions of predecessors such as Profs. Smalley, Curl, and Kroto become realized and materials such as high quality carbon nanotubes and graphene could be produced at competitive cost, this would lead to penetration of carbon nanostructures into markets where carbon-based materials are highly ideal, but not currently commercialized as active materials, such as in high performance electronics, batteries, supercapacitors, sensors, and optics, among others. Such broader penetration into these markets would yield a greater achievable impact of emissions reduction for $CO_2$-derived synthesis processes. This highlights that, at minimum, this approach has the capability to impact emissions and environmental sustainability, and motivates this as a new platform to intersect systems-level synthesis approaches that are sustainable with synthesis mechanisms that have been well-studied. Further, this approach overcomes limitations of other $CO_2$ capture and conversion approaches that produce low-value products, and presents a new frontier for carbon researchers to apply a framework of understanding of synthesis methods and mechanisms to a process capable of generating functional carbon materials from a freely available global pollutant.

Beyond these two arguments, it is noteworthy to discuss the carbon footprint of this technique compared to other $CO_2$ conversion technologies. As many conversion techniques hinge on low efficiencies that undermine the value of their approach, we highlight the high Coulombic efficiency of this technique (moles of electrons into the electrolysis divided by moles of carbon collected at the cathode) is consistently measured at > 90% and approaches unity. Because of this high efficiency, nearly all electrical energy is coupled into the 4 electron process to produce carbon, and the carbon impact approaches negative as the energy blend utilized to power the process moves towards carbon neutrality. Coupled with highly efficient thermal management of the high temperature reactor for the electrochemical growth of CNTs from $CO_2$, the total carbon dioxide impact per kWh of electricity used to drive electrolysis approaches a theoretical maximum of 0.309 $kg_{CO2}$/kWh. Whereas the average US energy blend today emits 0.458 $kg_{CO2}$/kWh, as our grid shifts towards a larger onset of renewable energy sources, the energy balance favors carbon negativity of the electrolysis process. For example, in the state of Washington where a large portion of the grid is supported by hydroelectric power, the carbon impact per kWh of electricity produced is 0.095 $kg_{CO2}$/kWh, resulting in *a net $CO_2$ negativity* of 25.4 kg $CO_2$ for every 10 kg CNTs produced using this technique.

## 1.4 Dissertation organization

This dissertation is organized as follows:

**Chapter 2** studies the effect of nanostructuring a commonly-utilized battery material, $FeS_2$, into ultrafine nanoparticles with an average diameter twice the diffusion length of iron. Due to the conversion reaction mechanism that takes place between $FeS_2$ and $Li^+$ or $Na^+$ ions, we discover

the ability to engineer nanoparticle size to allow full utilization of the $FeS_2$ active mass compared to surface-only conversion that takes place with bulk $FeS_2$ powders.

**Chapter 3** demonstrates the use of large-diameter CNTs grown via molten carbonate electrolysis as an anode for both $Li^+$ and $Na^+$ batteries and studies the difference in behavior between straight, less defective CNTs and highly disordered tangled CNTs.

**Chapter 4** investigates the growth of CNTs using electrochemical reduction of $CO_2$ mediated by molten carbonate electrolysis, and demonstrates for the first time the activation of catalysts solely derived from cathode materials *via* an inert anode enabled by atomic layer deposition coatings.

**Chapter 5** demonstrates the use of this technique towards the purification or consumption of scrap metals, with the growth of CNTs using catalytic materials that arise as either impurities in brass or as the bulk of iron-based scrap steels.

**Chapter 6** studies pre-deposited catalytic films of materials on non-catalytic surface to grow CNTs, and observes the effect of catalyst size on resulting CNT structure. This work also studies the phenomena of Ostwald ripening through a variety of growth times and finds the effects of Ostwald ripening to be exacerbated in the liquid-phase media compared to typically-observed behavior in gas-phase CVD growth.

**Chapter 7** illustrates a new platform for deriving a sustainability index for prospective battery materials, and highlights the use of $CO_2$-derived CNTs as both active cathode materials and conductive additives at the cathode side, coupled with earth-abundant LFP cathode materials.

# Chapter 2

## Ultrafine Iron Pyrite ($FeS_2$) Nanocrystals Improve Sodium Sulfur and Lithium Sulfur Conversion Reactions for Efficient Batteries

Adapted from: **A. Douglas**, R. Carter, L. Oakes, K. Share, A.P. Cohn, and C.L. Pint, "Ultrafine iron pyrite ($FeS_2$) nanocrystals improve sodium-sulfur and lithium-sulfur conversion reactions for efficient batteries," ACS Nano 9, 11156-11165 (2015) *with permission from the American Chemical Society*

### 2.1 Introduction

Over the course of the past decade, nanostructured materials have been widely used in energy storage and conversion electrodes to improve and optimize chemical storage processes.[79-81] Among the numerous advantages that nanostructured materials bring is the capability to engineer the size and shape of active storage building blocks to balance chemical kinetics of metal-ion intercalation reactions, yielding improved utility of active material,[82-84] less mechanical pulverization during cycling,[85, 86] and better power capability.[84, 87] However, it is not evident that these benefits scale down to nanostructures exhibiting length scales that lead to quantum confinement phenomena, such as quantum dots, where the particle size is comparable to the Bohr radius. Many of the most studied nanostructured materials for metal-ion batteries, such as silicon,[88-91] exhibit alloying or intercalation reactions where the metal ions shuttle through a solid-electrolyte interphase (SEI) layer to store charge within the interior of the storage material. In these materials, reports have emphasized the detrimental effect of ultrafine nanoscale materials due to the dominance of the SEI layer on inhibiting reversible storage.[92, 93] In the particular case of silicon, researchers have emphasized that SEI layer growth upon cycling in ultrasmall nanostructures can

deactivate the active storage material, leading to lower capacity and shorter cycling lifetimes than larger nanoparticles.[92] Similar observations have been made with other intercalation or alloying storage materials as well, including antimony and tin nanocrystals, indicating that nanostructures that are too small may not be advantageous for metal-ion storage.[94, 95] Recent work by He et al. shows the same trend for antimony that has been previously observed for silicon, where a nanocrystal size of 20 nm greatly outperforms those of 10 nm and bulk powder in terms of capacity, rate capability, and reversible cycling.[94]

In contrast to intercalation or alloying reactions, where metal atoms are reversibly shuttled in and out of a host lattice, conversion reactions involve the chemical transformation of one or more of the atomic species into a host lattice to form a new compound.[96] An example of this is the conversion of a metal disulfide, $MS_2$, into a conversion product involving metallic domains (M) and $Na_2S$ or $Li_2S$ compounds that can be reversibly formed.[97] Ultrafine nanoparticles (~2-10 nm) have been assessed for their capability to reversibly store charge through conversion reactions, including ZnO,[98] $SnO_2$,[99] CoO,[100] and $Co_3O_4$,[101] even though reasoning for why this differs from that observed in nonconversion reactions has not been identified or discussed.

In this spirit, the metal sulfides, which exhibit conversion reactions with lithium or sodium metal atoms, have been at the forefront of both fundamental and applied research in battery systems. Recent work by McDowell et al. has demonstrated lithium conversion reactions in metal sulfides to be dictated by the crystal structure of the host lattice as well as the diffusion length of metals during cation exchange to form $Li_2S$ products.[97] As Cu (in $Cu_2S$) exhibits long diffusion lengths, Fe (in $FeS_2$) is limited to shorter diffusion lengths (LD = $10^{-17}$ $cm^2$ $s^{-1}$ at 100 °C or ~$10^{-18}$ $cm^2$ $s^{-1}$ at room temperature[102]) still inaccessible by most nanostructures. Thus, rational approaches to nanostructuring electrode materials can strongly impact the kinetics and thermodynamics of

cation-exchange chemical storage transformations. Whereas most studies on metal sulfides are focused on the transition metal dichalcogenides,[97, 103, 104] $FeS_2$ (cubic pyrite, "fool's gold") is a highly promising material that has not been widely studied for secondary battery systems. $FeS_2$ is particularly attractive for energy storage technology due to its earth abundance, low toxicity, and low raw material cost.[103, 105] As $FeS_2$ is a common byproduct of coal production, it has been a stable, low-cost cathode material employed in off-the-shelf commercial lithium primary battery technology. Only recently has iron pyrite been investigated for secondary lithium ion batteries owing to a high theoretical capacity of 894 mAh/g[106] that comes from the storage of four lithium ions per $FeS_2$ via a conversion reaction to Fe and $Li_2S$.[107, 108] Studies have also recently shown that iron pyrite is a suitable material in a rechargeable sodium ion battery[109, 110] and that the sodium undergoes the same conversion reaction to form Fe and $Na_2S$.[111, 112] The conversion reaction within both sodium and lithium devices using pyrite leads to rapid degradation of active bulk storage material,[113, 114] which has been improved by nanostructuring into nanocubes[83] and nanowires[84] with features greater than 50 nm.

In this work we explore the sodium and lithium conversion of ultrafine $FeS_2$ nanoparticles, with a tight size distribution centered around ~4.5 nm, which is in the size regime where strong quantum confinement effects are observed.[115] Compared to nonconversion storage processes, we identify the ultrafine character of the nanoparticles to have a beneficial role in storage of sodium and lithium. This is due to ultrafine nanoparticles having a size comparable to the diffusion length of iron during a conversion reaction, leading to reversible and efficient cation exchange, a feature that is inhibited in larger nanocrystals or bulk materials. This "pins" conversion products to localized nanodomains, stabilized by the poor diffusion kinetics of Fe during cation exchange, and

poses a synergy between $FeS_2$, one of the most stable and earth abundant battery materials, and ultrafine "quantum dot" nanoparticles.

## 2.2 Experimental Details

### *2.2.1 $FeS_2$ Synthesis*

Iron(II) chloride tetrahydrate ($FeCl_2*4H_2O$, 99%), sodium thiosulfate pentahydrate ($Na_2S_2O_3*5H_2O$, 99.5%), thioglycolic acid (TGA, 99%), and anhydrous ethanol were purchased from Sigma-Aldrich. E-pure deionized water (18.2 MΩ 3 cm) was obtained from a Millipore Milli-Q system. All chemicals were used as received without any further purification. In a typical synthesis following a method previously described and modified from Bai et al.,[116] 0.123 g (1.15 mmol) of $FeCl_2*4H_2O$ was dissolved in 45 mL of dimethyl sulfoxide (DMSO) and 180 μL (2.60 mmol) of TGA. This solution was placed in a three-necked flask fitted with a valve and was deaerated by bubbling of 99.99% nitrogen for 30 min. A second solution of 0.725 g (2.93 mmol) of $Na_2S_2O_3*5H_2O$ (Aldrich) in 10 mL of 18 MΩ deionized water under a $N_2$ atmosphere was dissolved under a nitrogen atmosphere and dropwise added into the solution while stirring and continuously purging the reaction media with nitrogen for 15 min. The nanoparticles were allowed to grow and crystallize under conditions of continuous reflux at 139 °C for 4 h. Upon completion, the NPs were separated from the reaction media by centrifugation and purified several times with methanol. The final products were dried under vacuum at 60 °C for 6 h and stored under an Ar atmosphere.

*2.2.2 Na- and Li- Ion Battery Device Fabrication and Electrochemical Testing*

Half-cell devices were assembled in an Ar glovebox using 2032 stainless steel coin cells (MTI). For the sodium ion batteries, the $FeS_2$ NPs were dispersed in a slurry with conductive carbon black and PVDF binder at a ratio of 3:1:1, respectively. The slurry is assembled as a cathode material with a 2500 Celgard separator saturated with 1 M NaPF6 in diethylene glycol dimethyl ether (DGM) (Sigma-Aldrich) separating the cathode material from pure sodium foil (Sigma-Aldrich). The same procedure is followed for the lithium ion batteries, using lithium (Sigma-Aldrich) as the counter electrode and, for the electrolyte, 1 M LiPF6 in 1 g/1 mL of ethylene carbonate (EC) and diethyl carbonate (DEC). The devices were tested utilizing a Metrohm Autolab multichannel testing system. Cyclic voltammetry was performed at room temperature on the devices between 0 and 3.0 V at a constant scan rate of 0.1 mV/s, and galvanostatic charge-discharge measurements were carried out for constant currents ranging from 0.1 to 1 A/g. Cycling studies were performed at 0.1 A/g.

*2.2.3 Ex-Situ TEM and Raman Analysis.*

Batteries were cycled twice and left in a fully sodiated state to characterize products of sodiation. For TEM analysis, electrode materials from disassembled coin cells were scraped onto amorphous carbon TEM grids inside the Ar glovebox and subsequently imaged using an FEI Osiris TEM at a beam voltage of 200 kV and a screen current of 1.3 nA. For Raman spectroscopic preparation, electrodes from disassembled coin cells were placed between two glass slides with an O-ring around the steel disc inside the Ar glovebox. The sides of the glass slides were clamped with binder

clips, and the airtight system was then utilized for *ex-situ* Raman experiments. Raman measurements were performed on a Renishaw inVia microscope using 532 nm laser excitations.

## 2.3 Results and Discussion

To date, there have been few works performed on ultrafine nanoparticles for energy storage, and despite the promise anticipated for such materials, there has yet to be both fundamental and applied advances for quantum dot, or generally quantum-confined nanocrystal scale materials, in batteries. In this study, our focus is on the use of $FeS_2$ due to the extensive use of $FeS_2$ in commercial lithium primary battery applications. The combination of $FeS_2$ materials with sodium-containing electrodes represents a realizable and cost-effective platform that captures the cost/performance promise of sodium-sulfur batteries[117] while simultaneously overcoming the operation limitations of such systems. To approach this effort, we focused on the wet chemical synthesis of $FeS_2$ nanoparticles at sub-10 nm length scales through addition of aqueous sodium thiosulfate pentahydrate salts added dropwise into solutions containing iron(II) chloride tetrahydrate and thioglycolic acid.[116] This led to the formation of crystalline $FeS_2$ nanoparticles with diameters between 2 and 9 nm. Transmission electron microscopy (TEM) and corresponding fast Fourier transform (FFT) show the crystalline and ultrafine nature of the nanoparticles (Figure 8a). TEM and FFT indicate a measured lattice spacing of 2.7 Å, which is consistent with the (200) plane of iron pyrite.5 ImageJ image analysis software was used to assess the size distributions of nanoparticles evident in multiple TEM images (Figure 8b)[118] to obtain a log-normal distribution of nanoparticles with sizes between 2 and 9 nm and an average diameter near ~4.5 nm. This size range of $FeS_2$ nanoparticles is comparable with the Bohr radius (~1.3 nm) and hence correlates

with the size regime in which quantum confinement effects are observed,[115] evidenced by optical characterization.

We further analyzed the ultrafine particles through Raman spectroscopy, with 532 nm laser excitation (Figure 8c). Two prominent peaks (339 and 378 $cm^{-1}$) are observed that are indicative of the presence of S-S bonds and agree with other literature reports of nanoscale $FeS_2$ materials.[83, 84] The stretch mode observed near 339 $cm^{-1}$ is due to displacement of S atoms perpendicular to the S-S bond (Eg), and the mode near 378 $cm^{-1}$ is due to in-plane S-S stretching vibrations (Ag). A third peak that we attribute to the Tg symmetry mode is also visible at ~420 $cm^{-1}$. The absence of peaks around 210 and 280 $cm^{-1}$ confirms the absence of FeS in the synthesized sample. Likewise, the absence of Raman peaks around 386 and 323 $cm^{-1}$ indicates a lack of marcasite, orthorhombic

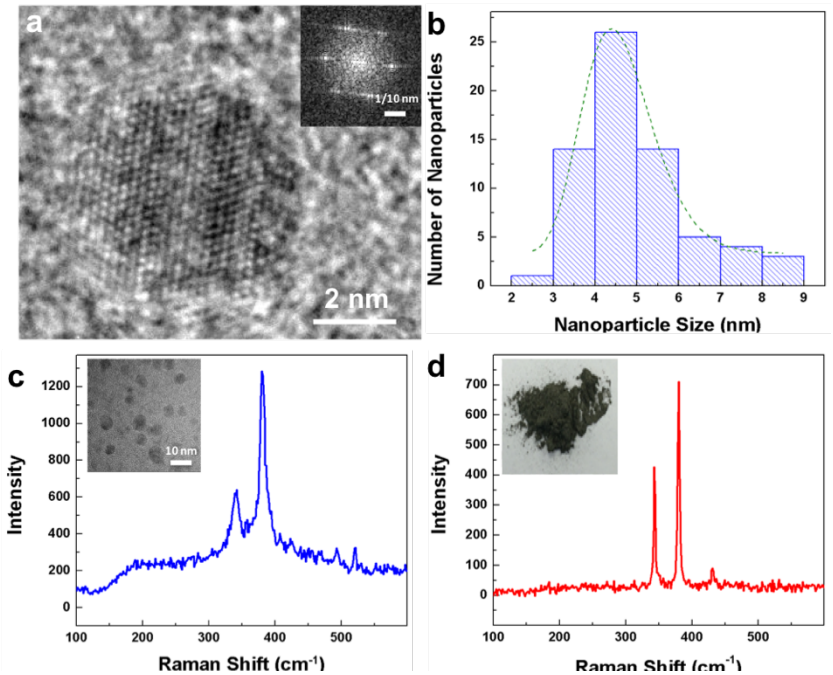


**Figure 8**. (a) Representative TEM image of synthesized $FeS_2$ nanoparticle with inset showing FFT diffraction pattern of crystalline structure; (b) particle size distribution with log-normal fit based on TEM image analysis; Raman spectra taken with 532 nm excitation for (c) ultrafine $FeS_2$ nanoparticles with SEM inset and (d) bulk $FeS_2$ powder with inset of image of purchased powder.

$FeS_2$, and confirms the synthesized structure of pyrite $FeS_2$.[84] The Raman spectra of the ultrafine $FeS_2$ are compared to bulk $FeS_2$ (Figure 8d), as our study uses bulk $FeS_2$ material as a benchmark to compare and understand the role of ultrafine nanostructuring on the observed performance and material characteristics. The Raman peaks from the bulk $FeS_2$ powder match well with those of the nanoparticles and are shifted ~3 $cm^{-1}$ due to the difference in surface to bulk ratios. Size distributions of the bulk $FeS_2$ materials based on SEM analysis indicate a distribution peaked near ~1 μm, with an average particle size of ~1.9 μm. To assess the electrochemical performance of $FeS_2$ nanoparticle devices, we combined $FeS_2$ ultrafine nanoparticles, carbon black, and PVDF into a slurry and cast it onto a stainless steel electrode. This electrode was combined with either sodium or lithium electrodes, pressed into a coin cell, and tested in a half- cell configuration with either $NaPF_6$/DGM or $LiPF_6$/EC-DEC electrolytes for sodium ion and lithium ion cells, respectively. Whereas our primary focus is on sodium ion batteries, we performed a series of experiments comparing ultrafine nanoparticles and bulk $FeS_2$ powder electrodes in the context of both sodium ion and lithium ion batteries to understand the general effect of ultrafine particles on both observed conversion reactions.

The sodium and lithium storage behavior of $FeS_2$ ultrafine nanoparticles was assessed through both cyclic voltammetry (CV) and galvanostatic cycling experiments, with comparison to electrodes composed of bulk $FeS_2$ electrode materials (Figure 9). In all cases, CV curves were recorded at a constant rate of 0.1 mV/s, starting from the open circuit voltage and cycling between 0.001 and 3 V vs $Na/Na^+$. The first, second, and third CV cycles for both bulk powder (Figure 9a,b) and nanoparticle devices (Figure 9c,d) are shown with corresponding galvanostatic chargedischarge curves inset. For Na-$FeS_2$ devices (Figure 9a,c), we observe three evident $Na^+$ insertion peaks for bulk powders near 2.1, 1, and 0.25 V and two peaks for ultrafine nanoparticle

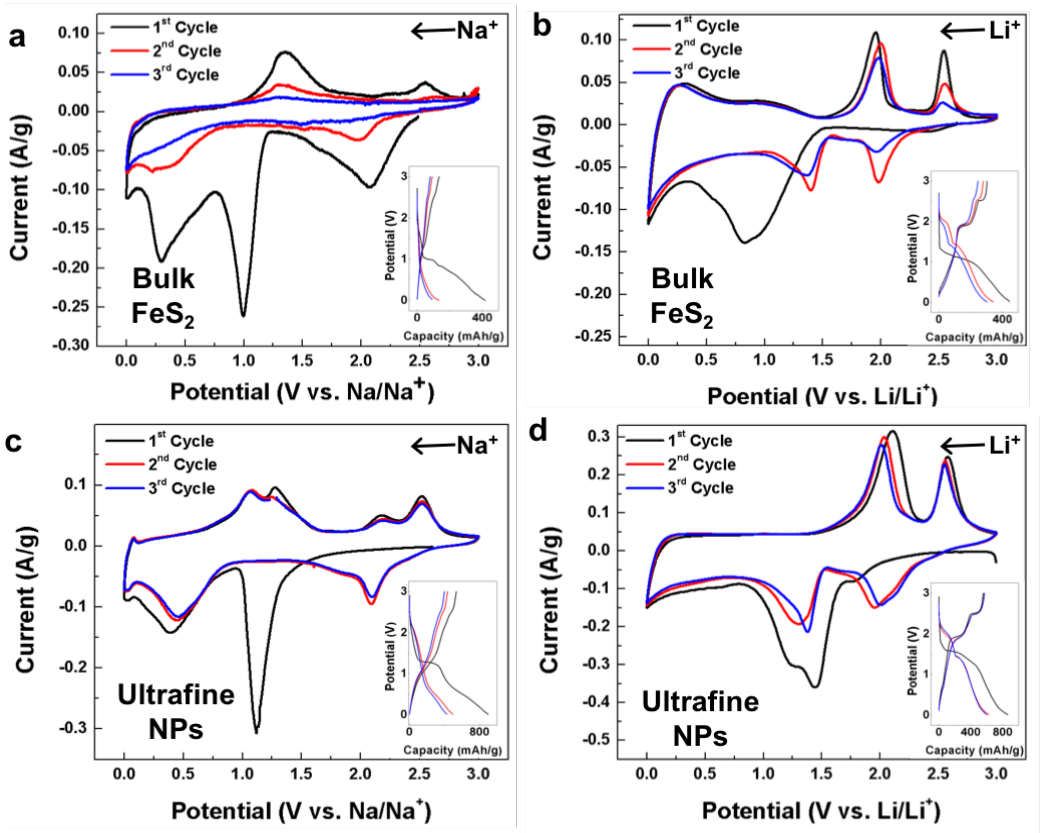


**Figure 9**. Electrochemical characterization of Na-FeS2 and Li-FeS2 cells. Cyclic voltammetry (CV) at 0.1 mV/s scan rats for (a) bulk FeS2 Na+ cells, (b) bulk FeS2 Li+ cells, (c) ultrafine FeS2 nanoparticle Na+ cells, and (d) ultrafine FeS2 nanoparticle Li+ cells. In all cases, the first three insertion-extraction cycles are shown and galvanostatic charge-discharge data for the first, second, and third cycles at 0.1 A/g are inset.

devices near 1.1 and 0.4 V. Subsequent $Na^+$ extraction occurs through a series of two peaks in both cases, near 1.25 and 2.25 V. We infer these peaks are due to $Na^+$ intercalation at high voltages to form $Na_xFeS_2$ ($x < 2$), then subsequent conversion at lower voltages to form Fe + $Na_2S$.[109, 112] This is in turn reversed in a similar manner through the reaction of Fe + $NaS_2$ at lower voltages to form $Na_2FeS_2$ and the removal of sodium at higher voltages to form $Na_{2-x}FeS_2$ ($0 < x < 2$). In both cases, the peak near 1 V is irreversible and precedes a lower voltage conversion transformation. Inset galvanostatic charge-discharge curves taken at 0.1 A/g for first, second, and third cycles indicate

similar features to the CV curves, with reversible capacities near 500 mAh/g for nanoparticles and 300 mAh/g for bulk powders. Notably, first discharge profiles also indicate irreversible capacity in both cases that we attribute to initial intercalation and SEI formation that precede the conversion process. Additionally, CV curves shown in Figure 9a for bulk electrodes exhibit significant degradation of all peaks after three CV scans at slow scan rates of 0.1 mV/s, leading to a capacitive storage signature, whereas the $FeS_2$ ultrafine nanoparticles exhibit excellent stability of observed conversion reaction peaks over three cycles. This supports a consistent theme of this work that elucidates the reversible cycling in ultrafine nanoparticles and irreversible processes in bulk powder electrodes. Notably, the trends observed for $Li^+$ insertion and extraction mirror that of $Na^+$ (Figure 9b,d), except with a conversion reaction that produces Fe + $Li_2S_6$,[107, 109, 119-122] through an intercalation process to form $Li_{2-x}FeS_2$ ($0 < x < 0.8$) (~2.6 V),[84, 105, 112, 123] which is reversed in a similar manner to that observed with $Na^+$.[83] Further, similar to that observed for $Na^+$ devices, CV curves indicate compromised cycling performance over three CV cycles for bulk electrodes and reversible redox conversion storage over three CV cycles for ultrafine nanoparticles.

Whereas the clear differentiation between cyclability in bulk electrode materials and ultrafine NPs is evident in Figure 9, cycling and rate capability studies on all samples were performed for sodium ion and lithium ion cells and are presented in Figure 10.

A characteristic feature of bulk $FeS_2$ cycling is a rapid loss of capacity in the first few cycles, accompanied by poor charge efficiency, not as apparent for ultrafine NPs. Additionally, in both cases the ultrafine NP cycling performance stabilizes, whereas the bulk cycling performance consistently declines over 30 cycles. For $Na^+$ cells, we observe ultrafine NP electrodes to exhibit 64% of the initial discharge capacity (relative to second cycle) over 30 cycles, with only a 6% decline of capacity between cycle 10 and 30, indicating stable cycling performance.

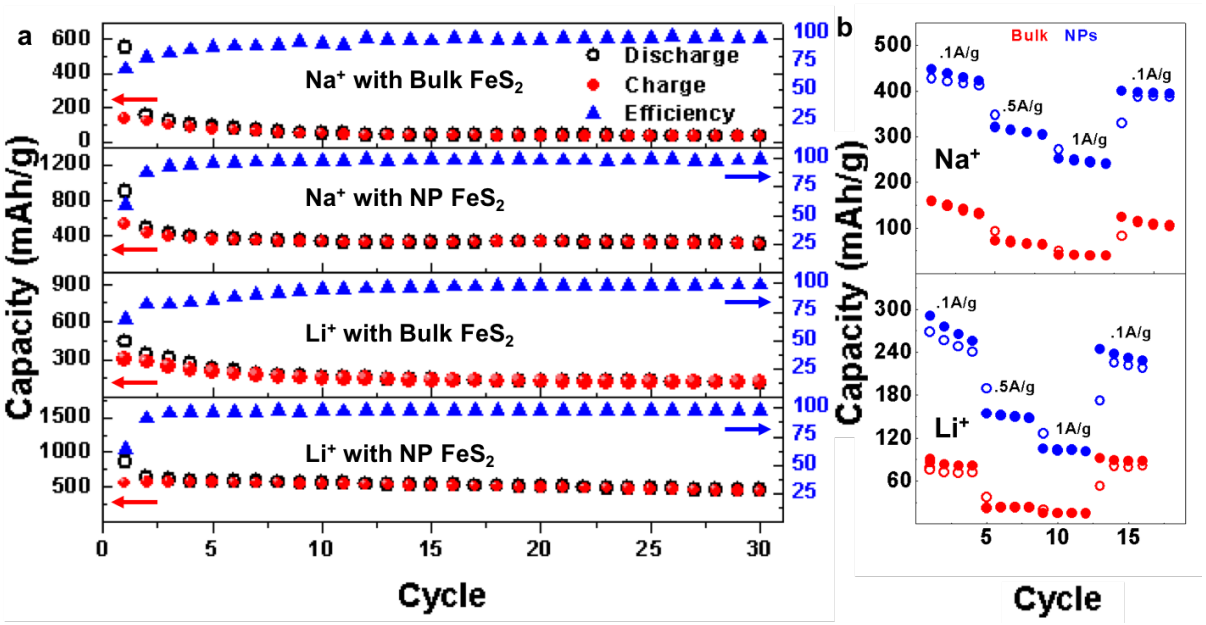


**Figure 10**. (a) Cycling performance and charge efficiency of bulk and ultrafine nanoparticle devices in Na FeS2 and Li FeS2 cell configurations, using galvanostatic cycling at 0.1 A/g, and (b) performance of devices with higher galvanostatic charge discharge rates

This is compared to bulk electrodes, which exhibit a 79% total loss (maintaining only 21% of the second cycle capacity) in capacity over cycling, with 36% capacity loss in the last 20 cycles. Notably, this trend also holds for $Li^+$ cells, where the ultrafine NP electro- des maintain 72% of initial (second cycle) capacity after 30 cycles, whereas bulk electrodes only retain 34%. As expected, the $Na^+$ cells indicate a more significant divide between cycling performance of ultrafine NP electrodes and bulk material electrodes due to the larger size of Na ions. Additionally, these trends hold for rate capability studies (Figure 10b), where cycling up to 1 A/g was achieved. Due to SEI formation in the first cycle that precedes a chemical transformation occurring in subsequent cycles rate-limited by the mass diffusion of Fe in $FeS_2$ (LD ≈ 10x18 $cm^2$ $s^{-1}$), the bulk materials exhibit virtually negligible capacity at higher rates of 1 A/g in both cases, whereas the ultrafine $FeS_2$ NPs exhibit stable capacities of >250 and >100 mAh/g for both $Na^+$ and $Li^+$ cells cycled at 1 A/g, respectively. This provides support for good rate capability that is enabled by short Fe

diffusion lengths in the ultrafine nanocrystals. Furthermore, it is important to note that an absolute comparison of capacity in our $FeS_2$ ultrafine NP electrodes relative to other reports utilizing intermediate-sized nanostructures (e.g., 40-50 nm) indicates results that are in some cases slightly improved[112] or in other cases slightly lower.[84] However, given the importance of size-limited mass diffusion occurring during cation-exchange processes, it is important to design experiments to decouple (i) fundamental size- or shape-dependent characteristics of these processes and (ii) properties at the device level that are related to electrode processing. In this manner, the comparison between ultrafine NPs and bulk particles presents a size comparison extreme enough to clearly distinguish the difference in size on this cation-exchange process.

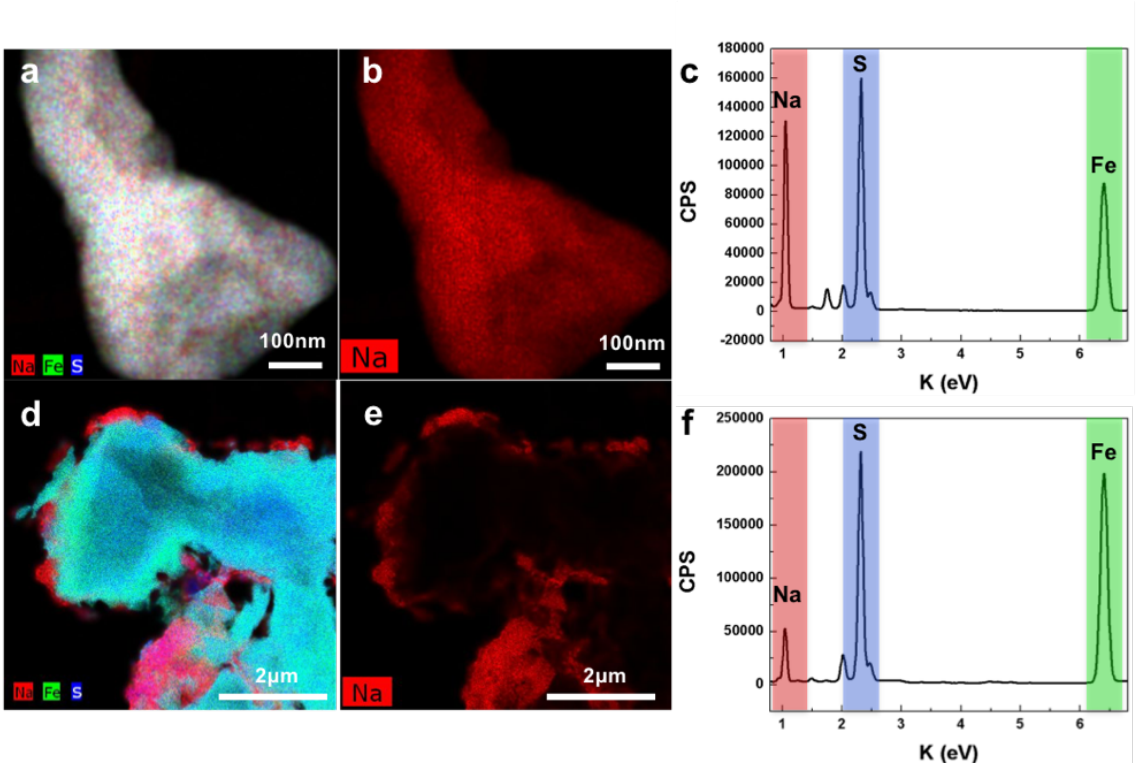


**Figure 11**. (a) STEM EDS map taken after sodium insertion of an agglomerate of NPs; (b) Na isolation in the same agglomerate; (c) X-ray spectra of NPs; (d) STEM map of bulk powder; (e) Na-only map of image in (d); and (f) elemental spectra of bulk powder.

At this point, electrochemical analysis indicates a consistent picture where ultrafine $FeS_2$ NPs outperform bulk $FeS_2$ electrode materials on all fronts of capacity, cyclability, and rate capability, but mechanistic understanding differences in these two electrode materials remain elusive. We therefore performed both ex-situ scanning transmission electron microscopy energy dispersive X-ray spectroscopy (STEM EDS) analysis (Figure 10) and *ex-situ* Raman spectroscopic analysis (Figure 11) to understand the mechanistic role that ultrafine NPs play to enable this improved performance. In both cases we focused our efforts on Na ion cells because in this system the ultrafine $FeS_2$ NP electrodes exhibit the greatest benefit toward cycling and rate capability in comparison to bulk $FeS_2$ electrodes.

In the first case, we performed STEM analysis on $FeS_2$ electrodes after two subsequent charge-discharge cycles in $Na^+$ cells. Shown in Figure 10a is a representative STEM EDS map of cycled $FeS_2$ nanocrystals that contain multiple $FeS_2$ ultrafine NPs. The cluster contains a uniform distribution of Na, Fe, and S elements evenly distributed throughout the material, indicative of the formation of a uniform chemical conversion process that occurs throughout the material. Individual EDS maps further support sodium distribution through the cluster of ultrafine NPs, indicating that Fe diffusion out of the sulfur anion sublattice and cation-exchange with Na uniformly occur throughout the structure. Comparing the X-ray spectra obtained from EDS maps (Figure 10c), the ratio of Na/Fe is 1.48. On the other hand, the EDS maps of flakes containing bulk $FeS_2$ materials after two cycles tell a different story, where the conversion products are not uniformly distributed through the material, and separate domains containing Na and $FeS_2$ can be identified (Figure 10d), with an elemental Na/Fe ratio of 0.26. Separate EDS maps (Figure 10e) indicate that sodium conversion products are produced only near the surface of the bulk material flake, leaving the interior material in the flake unreacted. Also apparent from the composite EDS

map is Fe-rich domains and a slight elemental concentration gradient between the interior and exterior of the bulk flake. Collectively, these two observations immediately highlight a marked difference in the mechanistic nature of the storage processes in ultrafine nanoparticles and bulk materials.

To further support the TEM analysis, we performed *ex-situ* Raman spectroscopic mapping of both bulk and ultrafine NP $FeS_2$ electrodes after two charge-discharge cycles (Figure 11).

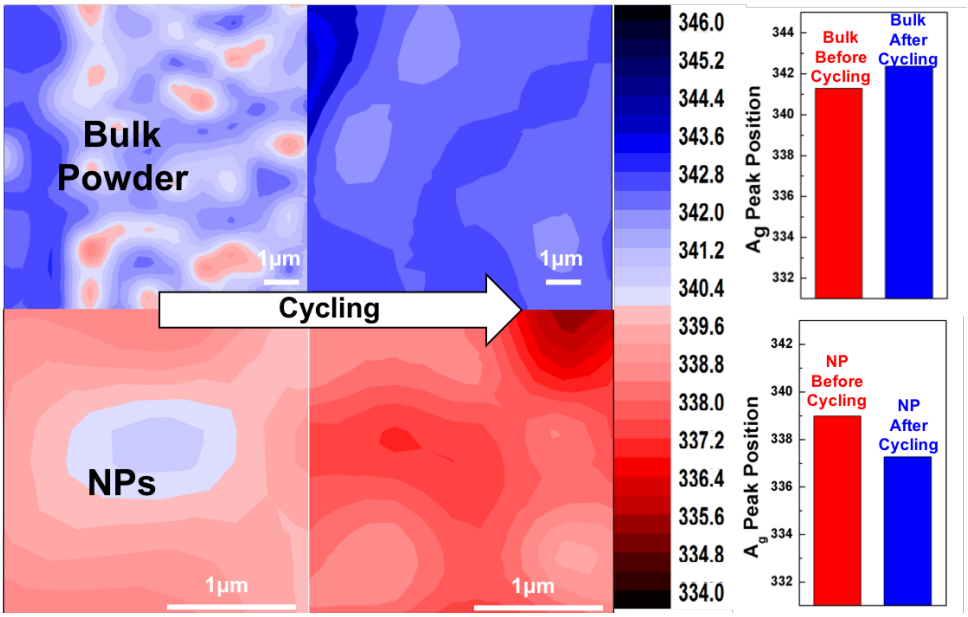


**Figure 12**. Raman spectroscopic mapping of the Ag peak in bulk FeS2 (top) and ultrafine FeS2 NPs (bottom) after cycling in a Na FeS2 cell configuration. Each map is a compilation of >200 independent Raman scans. (Right) Average position of the Ag peak based on data in maps.

Each map is a compilation of >200 individual Raman spectroscopic scans over an area from tens (NPs) to hundreds (bulk) of micrometers. To analyze the effect of $Na^+$ cycling in these materials, we studied the position of the Ag mode that corresponds to S-S stretch modes occurring normal to the in-plane $FeS_2$ S-S bond configuration. As $Na^+$ enters into the pyrite structure along the (111)

direction,[109] the $Na^+$ intercalates between the S layers and converts the material from $FeS_2$ to Fe + $Na_xS$, yielding a shift in the Ag peak position. In the case of bulk electrodes, we observe an average (statistical) blue shift of ~1 $cm^{-1}$, whereas for ultrafine NP electrodes, we observe an average red shift of ~2 $cm^{-1}$. This indicates a greater absolute effect of Na interaction with ultrafine NPs relative to bulk consistent with greater capacity measured in electrochemical data (Figure 9) and elemental scans of Na in *ex-situ* TEM (Figure 11). Second, the observation of blue-shifted (bulk) versus red-shifted (NP) modes averaged from statistically relevant maps indicates a different physical environment in the electrode materials following cycling. In the case of bulk electrodes, a blue shift can be interpreted as a compressive strain that is imposed on normal S-S stretch modes,[124] likely due to the formation of irreversible surface-bound products that remove Fe cations from the $FeS_2$ bulk, yielding vacancy-mediated uniform compressive stress on the $FeS_2$ crystal. However, in the case of ultrafine NPs, we observe oppositely red-shifted Ag modes, which indicate expansion-related stresses on unconverted $FeS_2$. As remaining, unconverted $FeS_2$ will exist in close proximity to converted products, these stresses are anticipated to arise from nanoscale interfaces between converted $Na_2S$ and $FeS_2$, as the unit cell for $Na_2S$ is larger than $FeS_2$ (a = 0.652 nm for $Na_2S$ versus a = 0.542 nm for $FeS_2$).[125] These conversion products pinned directly at strained interfaces of unconverted materials offer a rapid kinetic pathway for complete conversion or efficient reversal transformations. This is in contrast to flakes of bulk electrode materials, where conversion products are isolated at the electrode-electrolyte surface, requiring conversion and reversal processes mediated by atomic diffusion, both observations in agreement with *ex-situ* TEM analysis. A picture therefore emerges that emphasizes the advantageous properties of ultrafine NPs in Na- (or Li-) sulfur conversion reactions, which is generally illustrated schematically in Figure 13.

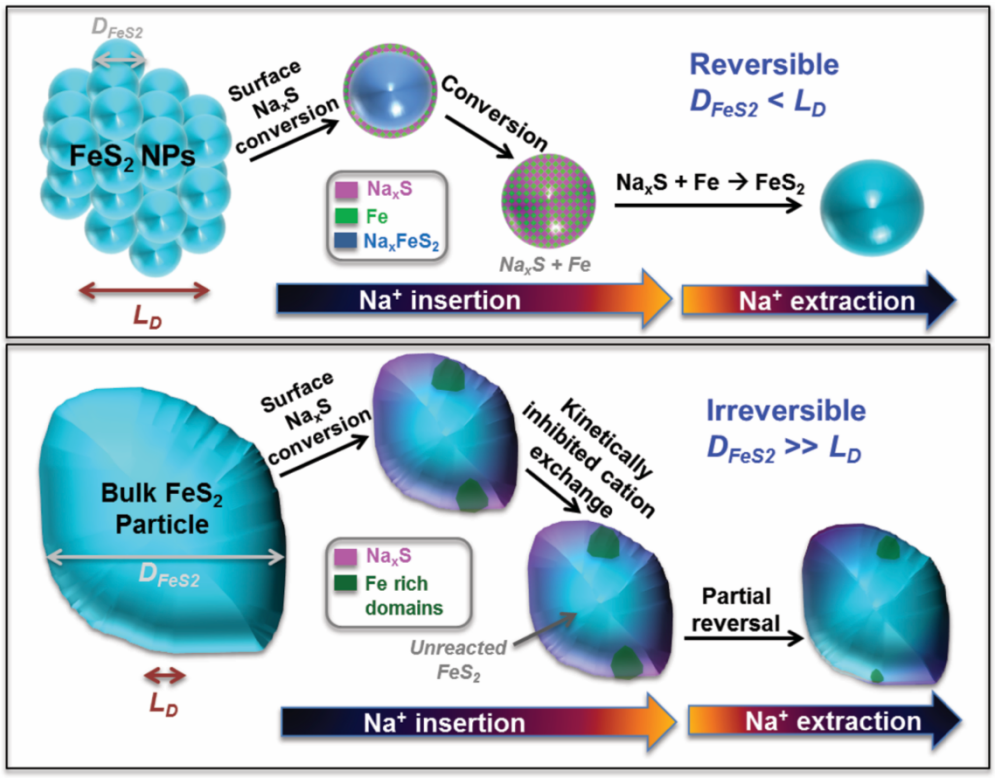


**Figure 13**. Scheme illustrating the benefit of using ultrafine NPs in sodium-sulfur conversion systems and the kinetic and thermodynamic limitations that make cycling of bulk electrode materials irreversible and ultrafine nanoparticles reversible. LD corresponds to the diffusion length of Fe ions to perform cation exchange, and $D_{FeS2}$ is the diameter of the FeS2 bulk or nanoparticle.

In comparison to alloying or intercalation reactions where metal ions simply shuttle in and out of host storage materials, conversion reactions involve the chemical transformation of a host lattice into products that must be kinetically and thermodynamically accessible to achieve reversibility. For bulk $FeS_2$ electrode materials, where the diffusion length of Fe during the cation- exchange reaction is orders of magnitude smaller than the size of the bulk crystallite,[97] chemical conversion processes are confined to the surface of the crystallite and mediated by the diffusion of both Fe and S species to the surface from the crystallite interior. This leads to 100-500 nm sized clusters of $Na_xS$, as evidenced by TEM (Figure 11) and the formation of Fe-rich domains where Fe

diffusion can occur only from a limited distance from the surface of the particle. The concentration gradient from unconverted but Fe-depleted $FeS_2$ results in an $FeS_x$ crystallite under vacancy-induced compressive strain (Figure 12) and kinetic barriers toward reverse chemical transformations. As large $Na_xS$ conversion products and Fe-rich domains form on the surface to minimize the Gibb's free energy, these domains require greater energy over longer times to overcome entropic barriers for reversal. This is consistent with the first extraction peak positions observed in CV scans (Figure 9), which indicate a greater overpotential for bulk powder electrodes and an increase in overpotential for bulk electrode $Li^+$ cells upon successive cycling between the second and third cycles. This is in contrast to ultrafine nanoparticles, where the overpotential decreases with cycling in all cases. This indicates that stable conversion products and long diffusion lengths for reversal ultimately present barriers toward stable, reversible cycling. Simply nanostructuring the electrode material; an approach effective for intercalation or alloying reactions; does not necessarily overcome these constraints since the Fe diffusion length during the cation-exchange reaction remains a limiting factor until the $FeS_2$ nanoparticles achieve length scales less than ~10 nm based on previous insight from *in-situ* TEM measurements. This is notably a size regime where SEI layer effects dominate, and most often prohibit, performance in intercalation or alloying storage reactions. However, we argue that ultrafine $FeS_2$ NPs provide clear mechanistic advantages in this regime. First, due to the short diffusion length of Fe during cation exchange, Fe and $Na_xS$ form domains that maintain short separation distances due to the pinning of Fe species near con- version products. This is evidenced through *ex-situ* TEM and through *ex-situ* Raman analysis that indicates tensile strain in unconverted $FeS_2$ for ultrafine NPs, an effect that can occur only for strained interfaces in nanoscale domains. This means that reversal reactions are kinetically accessible, unlike storage in bulk $FeS_2$. Previous reports have elucidated

the necessity for ultrafine sizes in cation-exchange processes with CdSe nanocrystals,[126] even though such concepts have never been applied to storage reactions in battery systems. Second, the conversion products form at length scales comparable to the ultrafine NPs, compared to length scales of hundreds of nanometers for bulk materials. This means that the high free energy from ultrafine conversion domains minimizes the entropic barrier for reversal, yielding lower overpotentials and thermodynamic properties that facilitate reversible cycling. Overall, this presents a design route for electrode materials undergoing chemical conversion reactions where rational nanostructuring is a powerful tool to produce electrode structures that can store and release energy without adverse effects from size- and potentially shape-dependent kinetic and thermodynamic constraints.

## 2.4 Conclusion

We demonstrate that ultrafine $FeS_2$ nanoparticles bring mechanistic advantages for batteries that store charge through chemical conversion reactions. Electrochemical characterization of ultrafine $FeS_2$ NPs compared to bulk $FeS_2$ materials indicates improved capacity, improved cycling, and better rate capability for $FeS_2$ NPs. *Ex-situ* TEM and Raman data for Na-$FeS_2$ cells indicate this improvement is due to overcoming the significant kinetic and thermodynamic constraints of chemical conversion that is based upon a particle size comparable or smaller than the Fe diffusion distance during cation exchange and the formation of pinned nanoscale converted domains that facilitate chemical reversal. These limiting mechanisms for sodium-sulfur and lithium-sulfur conversion processes are more complex than alloying or intercalation storage reactions widely studied for metal-ion batteries and specifically highlight the benefit of ultrafine or quantum dot length-scale nanoparticles for reversible and efficient storage.

Not only does this provide a route to match low-cost materials with high-capacity sodium-sulfur (or lithium-sulfur) based conversion storage reactions, but it opens up a pathway toward a new size regime for the design of chemical storage systems. As a significant effort has been placed on understanding the manifestation of quantum mechanical phenomena in nanocrystals and quantum dots toward applications in recent years, we anticipate an exciting research area existing at the intersection of quantum-confined nanostructures and energy storage or conversion processes where kinetics and thermodynamics ultimately dictate performance. This is compounded by our results that demonstrate, for the first time, that mechanistic processes occurring during sodium-sulfur and lithium-sulfur chemical conversion reactions are enhanced by nanostructures that have features at this length scale.

# Chapter 3

## Carbon Nanotubes Produced from Ambient Carbon Dioxide for Environmentally Sustainable Lithium-Ion and Sodium-Ion Battery Anodes

Adapted from: S. Licht, **A. Douglas**, J. Ren, R. Carter, M. Lefler, and C.L. Pint, "Carbon nanotubes produced from ambient carbon dioxide for environmentally sustainable lithium-ion and sodium-ion battery anodes," ACS Central Science 2, 162-168 (2016) *with permission from the American Chemical Society*

### 3.1 Introduction

A key challenge for atmospheric carbon capture and conversion technologies is the cost of operation or materials versus the perceived economic benefit to modern society. Issues such as stable carbon storage ultimately establish a cost and practicality bottleneck for many carbon capture processes.[127] Such issues can be resolved with the development of techniques that synergistically capture and convert atmospheric emissions into materials that can be developed into high-value products.[128] This produces a secondary market for greenhouse gas emissions and provides an economic value to pollutants that otherwise challenge the promise of long-term human sustainability on Earth.

In this manner, the elemental constituents of carbon dioxide, the most notable greenhouse gas, involve carbon and oxygen, which are foundational elemental building blocks for technological systems. Specifically, carbon-based materials are widely used in applications. One of the most notable applications of carbon is for anodes in lithium-ion (Li-ion) batteries, which are the principal rechargeable battery for electric vehicles (EVs) and consumer electronics.[129-131]

Commercial Li-ion batteries most commonly rely on anodes produced with graphite that exhibit a theoretical Li-anode capacity of 1 Li: 6 C, or 372 mAh g−1,[131] and an observed capacity of 280−320 mAh g−1.[132] Because of the greater Earth abundance of Na compared to Li (2.3% vs lithium's 0.0017% in the Earth's crust), recent efforts have also focused on carbon-based anodes for Na-ion battery systems.[14, 133, 134] A key challenge has been the low capacity of Na in crystalline carbons (32−35 mAh g−1) which can be improved by introducing defects into the lattice or engineering the electrode−electrolyte interface to facilitate solvent-assisted intercalation.[13, 135, 136] Whereas other materials besides carbon can form low-potential compounds practical for Na-ion and Li-ion anodes, such as Si and Sn,[134, 137] issues of rapid capacity fade, solid-electrolyte interphase vulnerability,[138] and existing commercial manufacturing infrastructure relevant to carbon-based anodes all present numerous technological challenges in transitioning battery systems away from carbon-based electrodes. Most recently, efforts to combine carbon-based Earth-abundant electrode materials, such as banana peels and peat moss, with sodium-ion batteries has been forward progress in this research area.[139, 140]

In this report, we build upon the solar thermal electro- chemical process (STEP),[60, 71, 141, 142] which is designed to convert greenhouse gas carbon dioxide into a useful carbon commodity. This technique uses inexpensive electrode materials (galvanized steel cathode and a nickel anode) and molten carbonate electrolytes that are heated and powered using concentrated photovoltaic (CPV) cells that convert sunlight into electricity at 39% efficiency. STEP has been shown to function effectively with or without solar powered operation to electrolytically split water, carbon dioxide, or metal oxides,[143] produce STEP carbon,[60] produce STEP ammonia and STEP organic,[144-146] and produce STEP iron or cement.[147-149] Here we show that this process can be used as a sustainable synthetic pathway for defect-controlled CNT and CNF materials, which exhibit

excellent performance in the context of lithium-ion and sodium-ion battery anode materials. This presents a sustainable route to convert carbon dioxide into materials relevant to both grid-scale and portable storage systems.

## 3.2 Experimental Details

### *3.2.1 CNT synthesis*

In this study CNTs are grown by DC electrolysis from (natural isotope abundance) CO2 dissolved in 750 °C molten Li2CO3 with, or without, added Li2O. A 100 mL Ni crucible serves as both container and (O2 generating) anode, and immersed 10 cm2 galvanized steel as the cathode. Following an initial low current (0.001 A for 0.5 h) step to grow Ni nucleation sites on the cathode, CNTs are grown on an immersed 10 cm2 galvanized steel cathode at 1 A for 1 h. Two types of nanostructures are generated: straight CNTs that are grown in electrolyte without added Li2O, and tangled CNTs that are grown when 4 m Li2O has been added to the electrolyte. After growth, cathodes are removed from the electrolyte, cooled to room temperature, and the carbon products are removed from the cathode wires. Finally, the carbon product is washed in a dilute 1M HCl wash to remove residual carbonate salts, solvent-exchanged to water through subsequent centrifugation cycles, and dried at 60 °C overnight.

### *3.2.2 Li- and Na- ion anode half-cell preparation*

For Li-ion cells, CO2-derived CNT electrodes were cast into a slurry with conductive carbon black and PVDF binder (3:1:1 ratio). This electrode was then combined with a separator, 1 M LiPF6 in

EC/DEC electrolyte, lithium metal foil, and pressed into a 2032 coin cell. Galvanostatic charge−discharge tests at rates were carried out at rates of of 100 mA/g.

## 3.3 Results and Discussion

The technique utilized to produce CNTs and CNFs from the STEP process is illustrated in Figure 14. The control of diffusion conditions during electrolytic splitting of $CO_2$ in molten lithium carbonate leads to either filled CNF or hollow CNT nanostructures, and control of oxide and transition metal concentration leads to tangled or straight fibers. This gives a level of control on the synthesized carbon nanostructures critical for battery applications. Specifically, the $^{13}CO_2$ and $Li_2{}^{13}CO_3$ CNF (Figure 14B) and 99% 12C on the CNT (Figure 14C) illustrated are grown under similar conditions, but diffusion restraints of the heavier isotope allow more frequent Ni nucleation points, which can tend to fill the interior of the tube nanostructure. Similarly, both straight CNTs (Figure 14D) and tangled CNTs (Figure 14F) can be produced. The straight CNTs shown are grown without added oxide. Using this process, larger diameter CNTs can be obtained by pulsing the formation current for 9 min on (at 1 A) and 1 min off. The tangled CNTs shown are grown in high electrolytic oxide DC conditions.[60]

Raman spectroscopic analysis was carried out to study the degree of graphitization of the synthesized carbon nanostructures. In Figure 14, the Raman spectrum exhibits two sharp peaks observed at 1350 and 1580 $cm^{-1}$, which correspond to the disorder-induced mode (D band) and the high frequency $E_2g$ first order mode (G band) that correspond generally to $sp^3$ and $sp^2$ hybridized carbon species, respectively.

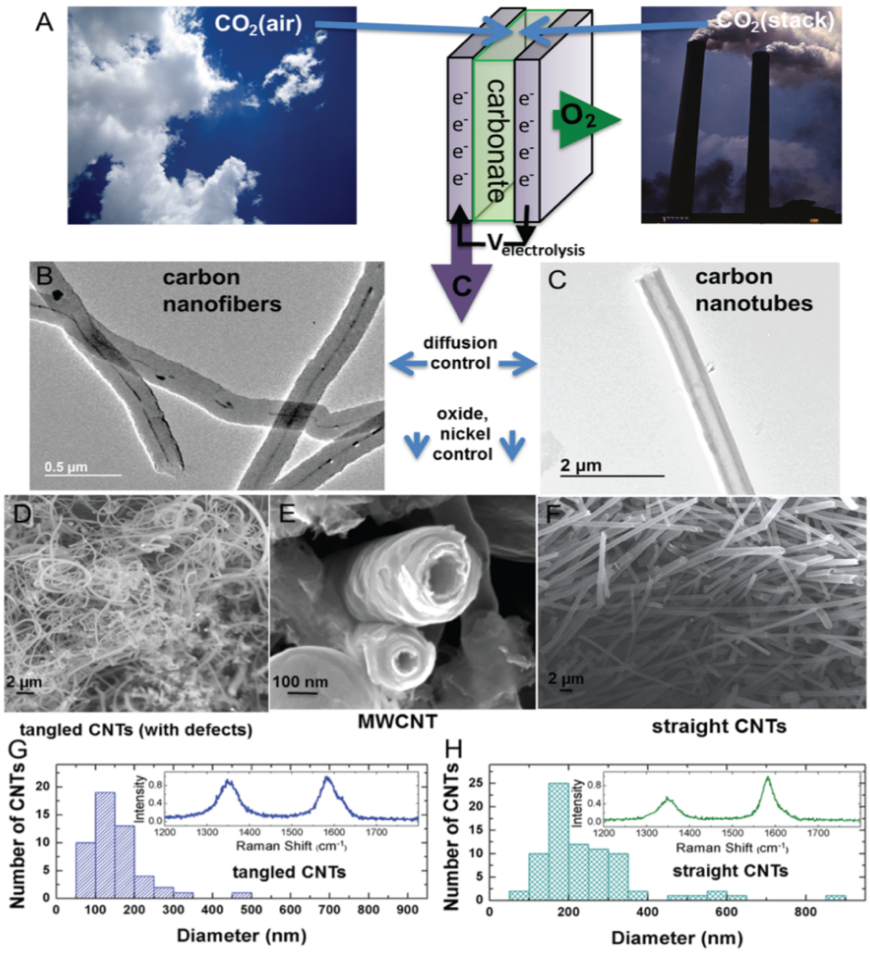


**Figure 14.** (A) Concept of high yield electrolytic synthesis of carbon nanostructures from dissolved air or smokestack concentrations of CO2 in molten lithiated carbonates. During CO2 electrolysis, transition metal deposition controls the nucleation and morphology of the carbon nanostructure. (B-C) SEM images depicting the different CNT products formed by controlled diffusion. SEM in (B) is from $^{13}C$, and SEM in (C) is grown from natural abundance CO2. (D-F) SEM images showing different CNT morphologies formed based on either the addition of Li2O (D- tangled, defective) or the absence of Li2O (F- straight, less defective). (E) Edge-on high magnification view of STEP CNTs. (G, H) Diameter distribution of straight (G) and tangled (H) CNTs based on image analysis of SEM images, and Raman spectra of CNTs as used in this study and synthesized at 750 °C from natural abundance $^{12}C$.

The intensity ratio between the D band and G band ($I_D/I_G$) is an important parameter to evaluate the graphitization and hence the total relative ratio of defective carbons in the material. As shown in Figure 14, the $I_D/I_G$ ratio for tangled CNTs is significantly higher than straight CNTs, the latter

of which is consistent with commercial hollow carbon nanofiber samples.[150] As we show in this study, synthetic control of the D:G ratio in a carbon material is useful to engineer the intercalation properties of carbon-based electrodes. Furthermore, based on a collection of SEM images of the as-grown tangled and straight CNTs, size distributions of the CNT materials were assigned based on ImageJ analysis software.[151] Size distributions indicate that the tangled CNTs exhibit a slightly overall smaller CNT diameter than the straight CNTs; however, all CNTs in this study are in a size range that is ideal for battery materials. The sizes of CNTs in this study (1) minimizes electrolyte consumption due to SEI formation in comparison to smaller nanostructured carbons and (2) enables full accessibility of the carbon material to alkali ion diffusion in thick, 3D electrode slurries.

To demonstrate the capability to transform $CO_2$ into a usable carbon material that can be assessed for energy storage applications, two types of CNTs, straight and tangled, were developed into electrodes, combined into half-cells along with electrolyte and a separator and pressed into coin cells for electrochemical testing. For Li-ion cells, $CO_2$-derived CNT electrodes were cast into a slurry with conductive carbon black and PVDF binder (3:1:1 ratio). This electrode was then combined with a separator, 1 M $LiPF_6$ in EC/DEC electrolyte, lithium metal foil, and pressed into a 2032 coin cell. Cyclic voltammetry tests and galvanostatic charge−discharge tests at rates of 100 mA/g elucidate the storage capability of both tangled (Figure 15A) and straight (Figure 15B) $CO_2$-derived CNTs. The first discharge, which is associated with solid electrolyte interphase (SEI) formation, is isolated from subsequent discharge cycles and plotted relative to the top axis in Figure 15A,B. For both the tangled and straight CNTs, subsequent cycling leads to high Coulombic efficiency (near 100%) and stable performance by the ~15th cycle. In both cases, the reversible capacity on the second discharge is measured near 370 mAh g−1, and this stabilizes near 350 mAh

$g^{-1}$ by the 15th cycle in both cases. To further assess the long- term performance of these materials, we carried out extended cycling tests at 100 mA/g (~C/7.5) rates for 200 cycles, which extended for ~2.5 months of continuous testing (Figure 2C). Here, a distinction between the storage behavior of straight (less defective) and tangled (higher defect content) CNTs emerges. Whereas the capacity of straight CNTs remains virtually unchanged over the cycling process, the storage capacity of the tangled CNTs is observed to steadily increase. After 200 cycles, the tangled CNT capacity is measured as ~460 mAh $g^{-1}$, with the capacity of straight CNTs remaining invariant at ~360 mAh $g^{-1}$. As such increased capacity above 372 mAh $g^{-1}$,[37, 152] and specifically during cycling,[153] has been reported in other studies on carbon nanostructured electrodes, our results imply this effect may be related to defect-induced modification to storage processes over the course of cycling. On the basis of the comparison of straight CNTs to tangled CNTs, the high defect content and torturous bends in the tangled CNTs likely could enable a transition from dilute staging of $Li^+$, which occurs during the formation of $LiC_6$,[154] to a combination of this and a mechanism analogous to pore-filling, which has been observed with other alkali-ion systems with very high defect-containing carbons.[13] The increased capacity over cycling emphasizes the continuous activation of this storage mode, which enables a capacity superior to the maximum alloying capacity of Li in $LiC_6$.

In addition to lithium-ion batteries, we also analyzed these materials as electrodes for $Na^+$ battery anodes. Recent efforts have been focused on $Na^+$ storage mechanisms into carbon materials,[13] and whereas some reports indicate intercalation,[139, 140] often involving solvent cointercalation,[136] defect-containing carbon materials are known to achieve moderate Na+ storage capacities based on a combined intercalation and pore-filling mechanism that only occurs with highly defective materials.[13]

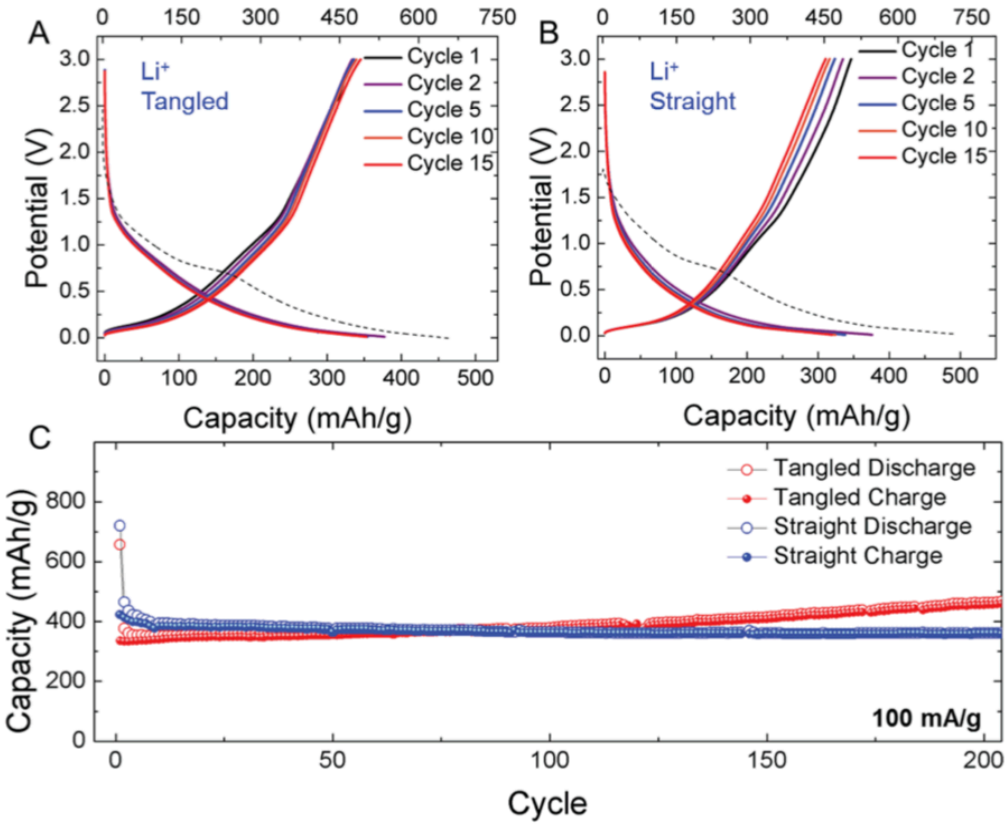


**Figure 15.** CO2-derived Li-ion batteries. (A, B) First 15 galvanostatic charge−discharge profiles for CO2-derived straight and tangled CNTs at a current density of 100 mA/g. The first discharge (dashed line) is longer than subsequent discharge cycles due to SEI formation and is referenced to the top axis in mAh/g. (C) Extended cycling performed at a current density of 100 mA/g over 200 cycles for both straight and tangled CNTs.

In this manner, the ability to modulate the defect density based on the STEP synthesis pathway enables a comparison that can elucidate this effect and highlights a synthetic trajectory toward high performance $CO_2$-derived sodium-ion battery electrodes for grid-scale applications. In this case, the batteries were prepared identically, except the electrolyte was based on 1 M $NaPF_6$ in diethylene glycol dimethyl ether (DGM), and the half-cells were cycled against Na foil counterelectrodes. Unlike the case of Li-ion cells, the Na-ion cells exhibit significantly different storage performance between the straight and tangled CNTs (Figure 16). In this case, galvanostatic charge−discharge data elucidates the straight CNTs to exhibit a reversible capacity that is only

slightly higher than the maximum intercalation capacity of $Na^+$ in crystalline carbons. Whereas the $I_D/I_G$ ratio is ~0.4, which implies a highly defective material relative to crystalline carbon, galvanostatic data indicate that this defect density is still too low to access a significant capacity of stored Na+ in the context of pore-filling mechanism. However, the tangled CNTs, which exhibit a higher ID/IG ratio near 0.9, exhibit reversible capacities over 130 mAh $g^{-1}$, which is ~2× that of the straight CNTs. This implies defects in a CNT material are critical to activate the mechanism for Na+ storage, and this is achieved in the tangled CNTs produced in the STEP process. To further assess the stability of this anode performance, both straight and tangled CNTs were cycled for 600 cycles at a similar rate of 100 mA/g. In parallel to Li-ion cells, this represents ~2.5 months of continuous cycling of the devices. Over the course of this cycling process, the devices show invariant performance with no observed capacity fade, which is improved compared to other defective carbon materials that exhibit storage via the pore-filling mechanism.[155] One possible explanation for this improved performance is a storage capacity that appears to originate mostly from the sloping part of the galvanostatic $Na^+$ insertion curve. Recent work by Bommier et al. has proposed that this sloping region is correlated with defect-activated sodium insertion in hard carbons.[13] This is distinguished from the flat, lower-voltage feature attributed primarily to plating of $Na^+$ on the interior of micropores in the anode. Our results are consistent with this picture since by increasing the defect density of the CNTs, the total capacity of the sloping region in the galvanostatic curves also similarly increases, but notably the flat signature at low voltages remains generally absent. Therefore, our results not only are in agreement with Bommier et al., but the invariant cycling performance observed over 600 cycles (~2.5 months) implies that defect-activated storage is highly reversible and not as prone to the capacity fade observed when sodium insertion occurs primarily through the plating mechanism. This implies that high capacity sodium-

ion batteries with excellent cycling performance can be rationally designed by controlling structural and defect properties of the carbons.

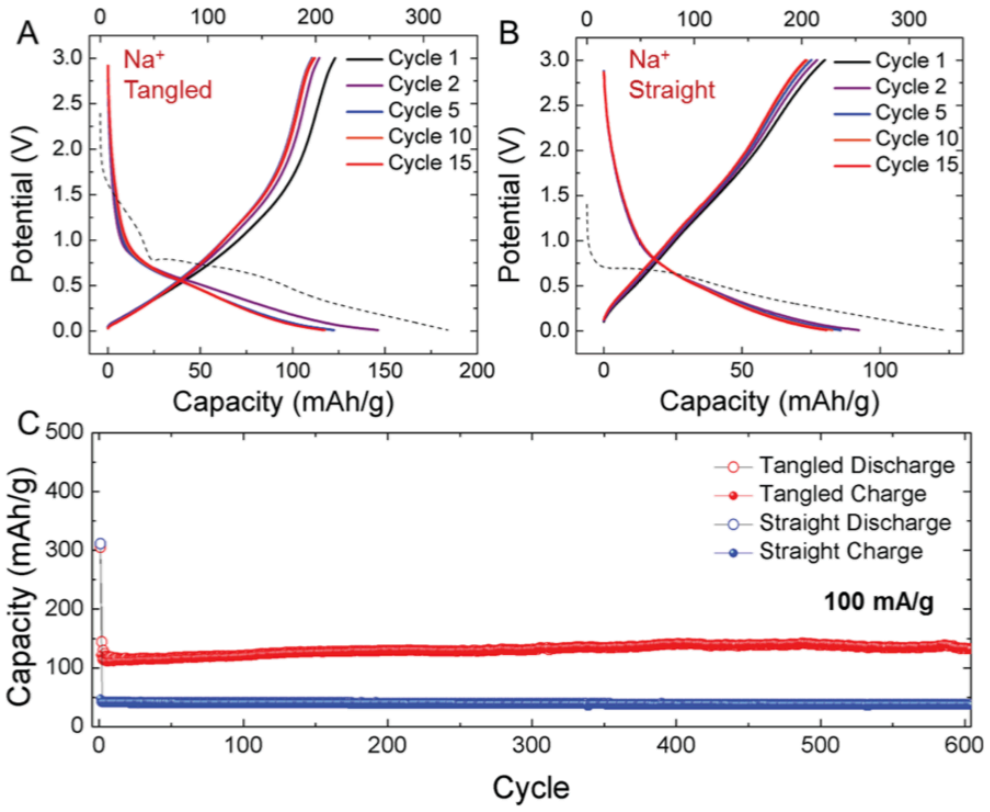


**Figure 16**. CO2-derived Na-ion batteries (A-B) First 15 galvanostatic charge-discharge profiles for CO2-derived straight and tanbled CNTs at current density of 100 mA/g. The first discharge (dashed line) is longer than subsequent discharge cycles due to SEI formation and is referenced to the top axis in mAh/g. (C) Extended cycling performed at current density of 100 mAh/g over 600 cycles for both straight and tangled CNTs.

Overall, electrochemical tests give promise to the function of $CO_2$-derived CNTs as practical anode materials for batteries. This establishes the principle that energy input can transform $CO_2$, which is a global pollutant with adverse environmental impact, into a secondary product that now is associated with an economic value in a thriving technological area. In order to illustrate this point, simple calculations were performed based on available data in the literature to

correlate the average value of $CO_2$ in batteries based upon the total cost per kWh of the battery cell (Figure 17). Unlike routes to transform $CO_2$ into fuels such as methanol, which targets a low-value hydrocarbon commodity, the transformation of $CO_2$ into active battery materials provides a valuation of the $CO_2$ that is associated with the total cost of the battery technology. The U.S. Department of Energy Vehicle Technology Office (FY 2015 Budget Outlook[10]) has set a target of $125 per kWh by year 2022, with an average battery cost of ~$325 per kWh in 2013.

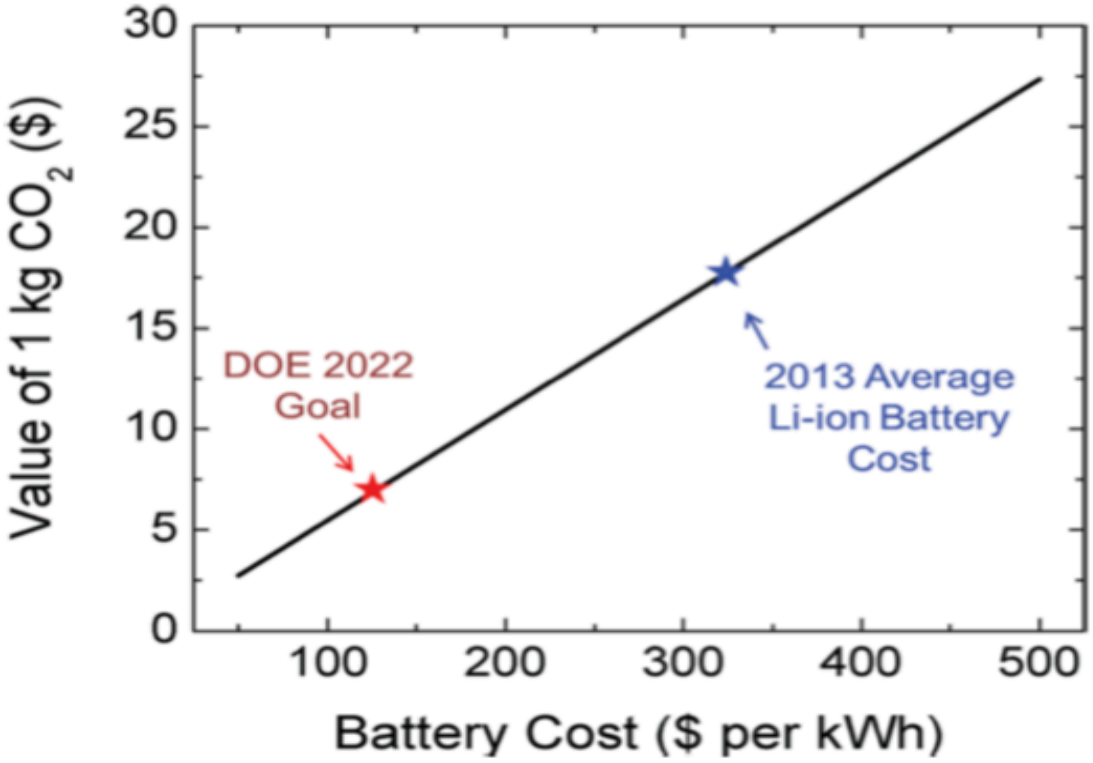


**Figure 17.** Generalized value of 1 kg of CO2 converted into CNT materials for batteries based on the total cost per kWh for the battery. The DOE target of $125/kWh for 2022 and the 2013 average Li-ion battery cost provide a window ranging from ~$5 to $18 of secondary value per kg of CO2. Anode cost relative to the full cell is extrapolated from data reported by David Wood's group,[156] and weight per kWh is extrapolated from a Panasonic 1.5 kWh (52 Ah) module.

These calculations, which are very generalized and can widely vary based on battery manufacturing techniques, battery size, and packaging processes, build upon the assumptions that

(1) ~8% of the total battery cost is associated with the anode,[156] (2) the total mass of anodic carbon in a 1 kWh module is <10% of the total weight of the battery, (3) the mass extrapolated for a 1 kWh module is ~5.3 kg (e.g., Panasonic 18650 type 1.5 kWh modules), and (4) processes to convert $CO_2$ to functional carbon materials transform all carbon into usable material. This explicitly demonstrates an operation window for large-scale processes capable of converting $CO_2$ into carbon-based battery anodes and explicitly demonstrates the principle that $CO_2$ can be associated with economic value in a growing technological sector.

## 3.4 Conclusions

Here we report the transformation of $CO_2$ into low-defect (straight) and higher defect (tangled) CNT materials for use in both lithium-ion and sodium-ion batteries using the STEP process. These battery materials show excellent performance and durability, with no capacity fade measured in over 2.5 months of continuous cycling, corresponding to over 200 cycles and 600 cycles for lithium-ion and sodium-ion devices, respectively. Control on the defect density was observed to be critical to enable capacities that surpass $LiC_6$ in Li-ion cells and overcome the bottleneck of 30−40 mAh/g capacity in sodium-ion cells that is associated with carbon materials. This provides a bridge toward associating economic value to $CO_2$, with a revenue window controlled by the cost of conventional battery technology per kWh.

# Chapter 4

## Iron catalyzed growth of crystalline multi-walled carbon nanotubes from ambient carbon dioxide mediated by molten carbonates

Adapted from: **A. Douglas**, R. Carter, N. Muralidharan, L. Oakes, C. L. Pint, "Iron catalyzed growth of crystalline multi-walled carbon nanotubes from ambient carbon dioxide mediated by molten carbonates," Carbon, 116, 572-578 (2017)

### 4.1 Introduction

The concentration of carbon dioxide in the atmosphere, $CO_{2atm}$, now sits at around 405 parts per million, the highest concentration in history.[1, 2] Due to the relationship between $CO_2$ and global climate change, capture and storage or conversion of carbon dioxide has attracted the attention of researchers in the effort to achieve a reduction in $CO_{2atm}$.[5-8] Sequestration technologies to store $CO_2$ underground are often bottlenecked by the limitations of available reserves (depleted oil and natural gas reserves) and the probability of gas leaks.[1] Similarly, injection of $CO_2$ gas into basaltic rock is promising, but limited by the long mineralization time (>3 years) and energy intensive injection.[157] At present, technologies studied for transforming $CO_2$ include: chemical, photochemical, and biological transformation of $CO_2$ into hydro-carbons and alcohols (including methanol and ethanol).[158, 159] Promising as a drop-in replacement fuel for gasoline, many researchers have concentrated their efforts on the chemical transformation of $CO_2$ into methanol,[160-163] but these low-value hydrocarbons and methanol produced at low system

efficiencies undermine the rationale of this approach. The challenge remains for efficient conversion of $CO_2$ into high-value secondary products.

The electrolytic conversion of $CO_2$ into nanostructured carbons has been investigated beginning with aqueous electrolytes.[164] However, the low solubility of $CO_2$ in aqueous solution and the similar reaction potential of water decomposition made the reaction impractical. Reduction of $CO_2$ was more recently investigated in room temperature ionic liquids (RTILs) due to their attractive electrochemical window and high solubility of $CO_2$, however the high cost and toxicity of RTILs inhibits their adoption in commercial applications.[18] Carbonate melts offer a low cost and high ionic conductivity with a low vapor pressure, and have been demonstrated to be a viable electrolyte for the reduction of $CO_2$. The deposition of carbon onto gold wire electrodes in molten eutectic carbonate electrolytes was first reported in the mid 1960s.[19] Building from early experiments, nanostructured carbon films deposited from low temperature eutectic electrolytes have more recently been investigated using inexpensive working electrodes such as aluminum, Ni, and steel,[20, 21, 23, 24, 73] even though control of carbon products remains a challenge. Energy storage applications such as supercapacitors have utilized high surface area carbon deposited from these low temperature eutectic electrolytes.[158] In the case of pure carbonate electrolytes, recent advances have observed the formation of CO in $Li_2CO_3$ at elevated temperatures(>850 °C),[22] and ultrathin graphite sheets onto steel electrodes in calcium electrolytes.[25, 26]

Owing to their extraordinary mechanical, electrical, and thermal properties, growth of carbon nanotubes (CNTs) has been at the forefront of research for nearly two decades.[31, 165, 166] In past years, comprehensive models of CNT growth have been developed to account for the various factors that impact gas phase surface supported growth, such as precursor chemistry,[41] catalyst composition and oxidation state,[42, 66, 67] catalyst size,[43] catalyst support properties,[44-46]

temperature,[47, 48, 167] and dynamic processes during growth such as Ostwald ripening, metal catalyst diffusion into the support layer, and mechanochemical termination processes.[50-53] Generally, it is accepted that iron catalyst nanoparticles are the most ideally suited for CNT growth, and typical processes achieving high density CNT growth in compact arrays utilize an iron catalyst layer supported by alumina. In contrast, growth of carbon nanostructures from electrochemical techniques remains a new idea, and recent studies leading to the first observation of carbon nanofibers[60] or large-diameter CNTs (>100 nm)[54] have been carried out using a corrosive Ni anode and steel cathode. The first report of carbon nanofibers grown from this process utilized a mixture of carbonates and soluble metal oxides between inexpensive steel cathodes and either Ni or Ir anodes, and found there to be a positive effect from Ni and Zn to grow fibers.[60] In this system, it is presumed that corrosion of the Ni is the basis for the metal catalyst, and no apparent route exists to control the formation of a surface-bound catalyst for CNT growth.[54, 60] Whereas these works have studied the interplay between cathode surfaces and electrodeposited catalysts (in the case of Zn coated cathodes and corroded Ni catalysts), currently no studies have been carried out to correlate catalytic activity in the presence of carbonates to the inherent catalytic properties of the electrode materials themselves. This is especially important since decades of gas phase carbon nanotube growth research has led to unequivocal correlation between catalyst composition, size, and the resulting CNTs that are grown.[167, 168]

While previous works have observed the catalytic activity of in-situ deposited catalysts to grow fibers and large diameter CNTs, here, we provide the first study on electrode processes in electro-chemical growth of carbon nanostructures, building on observations of traditional gas-phase CNT growth processes, which typically use only one active substrate. To control and understand growth, we utilize ALD, cathodes with different surface coatings and Fe metal

composition, and varying anode-cathode current density. Our results indicate the ability to use these concepts to direct the formation of iron-based catalyst nanoparticles to grow high yield (99%) and highly crystalline multi-walled carbon nanotubes with average outer diameter of ~27 nm from ambient carbon dioxide captured from the atmosphere.

## 4.2 Experimental Details

### *4.2.1 Electrode Preparation*

Three different anodes were used in electrolysis experiments. Anodes included untreated Ni wire (Fisher Scientific, 99%, 1 mm diameter), thermally oxidized Ni wire (1 h at 450 °C in air), and Ni wire coated with 500 cycles (~50 nm) of $Al_2O_3$by a Gemstar Arradiance atomic layer deposition (ALD). The thickness of this coating was determined through ellipsometry analysis of $Al_2O_3$ coatings on silicon wafers with a J.A. Woollam spectrometer. To accomplish this, we utilized sequential 28 ms pulses of $C_6H_{18}Al_2$and $H_2O$ with a residence time of 1 s. The cathodes used in these experiments were three different steels: 16 gauge galvanized steel wire (Home Depot), 316 stainless steel shim (Trinity Brand Industries), and 1010 steel shim (McMaster-Carr).

## 4.3 Results and Discussion

The general process of carbon nanotube growth relies on the decomposition of a carbon containing precursor most commonly on the surface of a metal catalyst. Only recently has the growth of carbon nanotubes been demonstrated through liquid phase electrolysis of $CO_2$, and parameters commonly related to traditional CNT growth, such as catalyst composition, carbon flux, and catalyst size, remains elusive without a clear understanding of how these components

originate or evolve. Therefore, the focus of the present study is to elucidate and control these parameters to control CNT growth to achieve high yield and high quality CNT materials from carbon dioxide. The molten carbonate electrolysis technique used to convert $CO_2$ into nanostructured carbon is illustrated in Fig. 18.

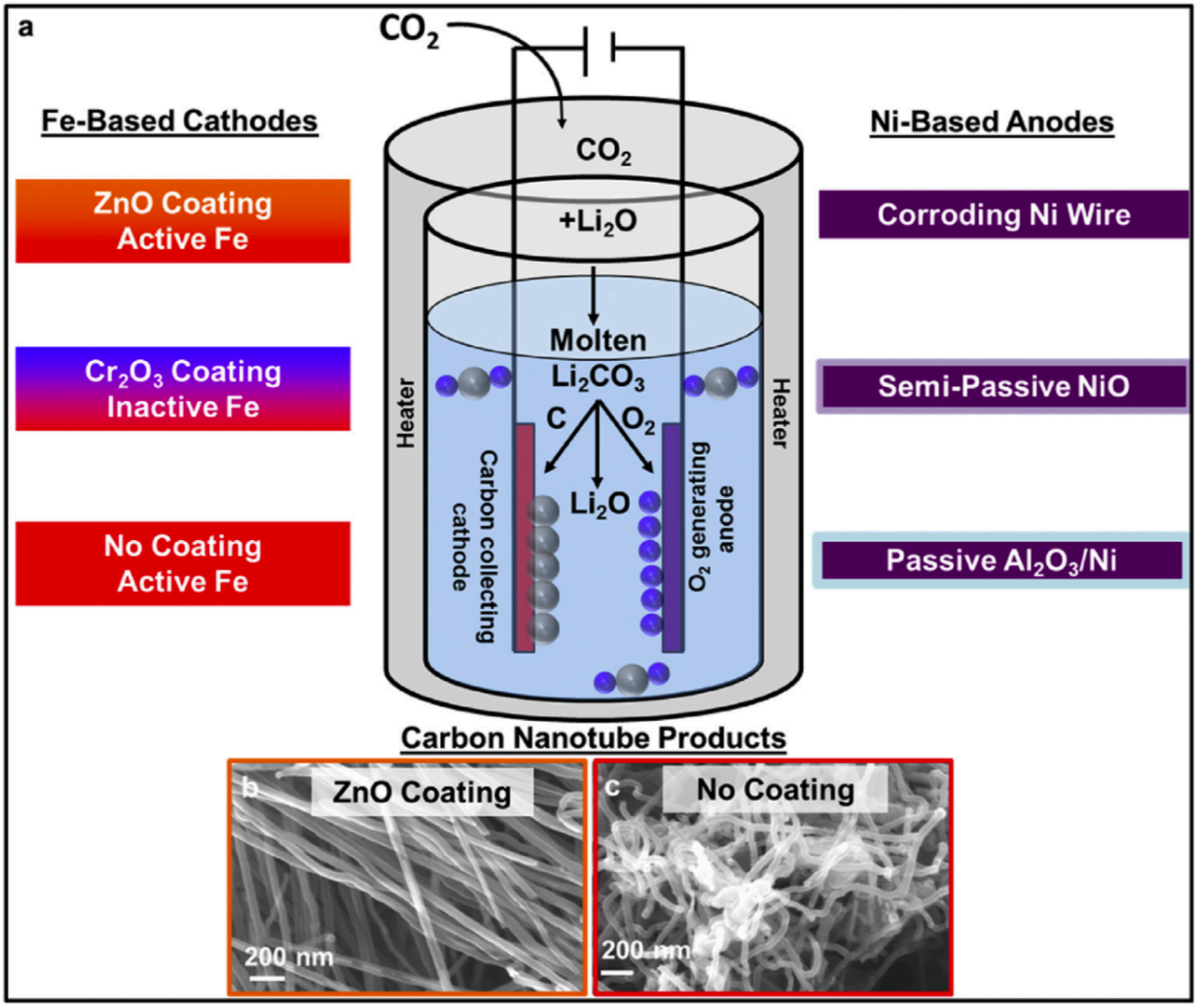


**Figure 18.** (a) Schematic illustration of electrolysis set-up including the different cathodes and anodes utilized in this study, and SEM images of carbon nanotube products grown on (b) ZnO coated (galvanized) steel and (c) uncoated (1010) steel electrodes.

Lithium carbonate was chosen as the electrolyte because of the lower standard reduction potential of C compared to the alkali metal, causing C to deposit onto the cathode rather than Li.[24] Briefly, a constant current is applied across a carbon collecting cathode (steel) and an oxygen-generating anode (Ni). This splits molten $Li_2CO_3$into C, which collects at the cathode, $O_2$ collected at the anode, and $Li_2O$. The remaining $Li_2O$ reacts with ambient $CO_2$ to regenerate $Li_2CO_3$ electrolyte. The equations are:

$$Li_2CO_3 \rightarrow Li_2O + C + O_2 \quad (1)$$

$$Li_2O + CO_2 \rightarrow Li_2CO_3 \quad (2)$$

The net equation from Equations (1) and (2) is:

$$CO_2 \rightarrow C + O_2 \quad (3)$$

This four-electron process converts $CO_2$ to carbon at a theoretical rate of 84 g C/kilowatt-hour at 100% faradaic efficiency and a potential of 1.33 V. Previous works have justified the argument of $CO_2$ capture by molten carbonate electrolytes, and work by Ren *et al*. demonstrated an $^{13}C$ isotope experiment to track $CO_2$ uptake and transformation into carbon nanofibers and large diameter nanotubes.[169] To assess the effect of the electrode on the CNT growth process, three different cathodes and anodes are studied and schematically represented in Fig. 18. The three anodes studied include untreated Ni wire, semi-passive thermally oxidized NiO, and fully passivated $Al_2O_3$ coated Ni wire. The three cathodes studied include galvanized steel, (ZnO-coated, Fe>95%), stainless steel ($Cr_2O_3$coating, 72% Fe), and 1010 steel (99% Fe). Without detailed understanding of the catalytic process, these three electrodes can be coupled with Ni-based anodes to produce a variety of carbon nanostructures including carbon fibers or nanofibers, petaled graphite materials, and carbon nanotubes. However, the lack of understanding of how the anode or cathode impacts the formation of each of these products limits a controlled route to design

the system to optimize tailored growth of one species. In this manner, our efforts herein are focused on tailoring these electrode materials to achieve high yield growth of highly crystalline CNTs (Fig. 18b and c). Whereas no previous experimental efforts have been made to address the catalyst species in molten carbonate electrolysis, it has been hypothesized that Ni corrosion into the electrolyte leads to plating onto the cathode and is responsible for the nucleation of carbon nanofibers (or carbon nanostructures) on the surface.[60] In order to understand the source of the catalyst for CNT growth, we carried out studies aimed to fully deactivate corrosion on the Ni anode in our system by forming passive, uniform coatings of alumina using atomic layer deposition. Whereas previous work demonstrated the inert nature of Ir anodes in molten carbonate electrolytes,[60] we focused on studying the tunable surface properties of Ni anodes, in an effort to utilize inexpensive electrode materials. Three cases were compared: untreated Ni wire, themally oxidized Ni wire, and Ni wire coated with ~50 nm of alumina using ALD. In each case, a current density during electrolysis of 100 $mA/cm^2$ was used and the cathode material was galvanized steel. As shown in Fig. 19, the carbon products obtained by varying the anode are significantly different implying the importance of the anode in steering the catalytic properties.

In the case of an untreated Ni wire anode material, the growth results primarily in carbon fibers with some small minority species of large-diameter CNTs. When the Ni wire is thermally oxidized to produce a rough oxide layer coating that exceeds the thickness of the native oxide, the carbon product in an identical process is steered toward the formation of hollow-center CNTs with large diameters (~100+ nm) and wavy surfaces that are indicative of a high $sp^3$ (defect) content. Finally, when ALD is utilized to produce a moderately thick (50 nm) and dense barrier layer on the Ni anode surface, straight CNTs with smaller diameters are observed. To understand these differences, we carried out post-mortem STEM EDS imaging of the CNT materials to correlate

the synthesis product and the chemical identity of the catalyst particles that remain embedded in the product. Despite trace metals present in galvanized steel, post-mortem SEM EDS imaging reveals the catalytic behavior of metals, as only those metals that participate catalytically will be embedded in the CNTs. In both cases of the Ni wire and thermally oxidized Ni wire anodes, we consistently observed the presence of Ni-rich bimetallic Ni-Fe catalyst particles at the exterior edges of grown carbon nanostructures.

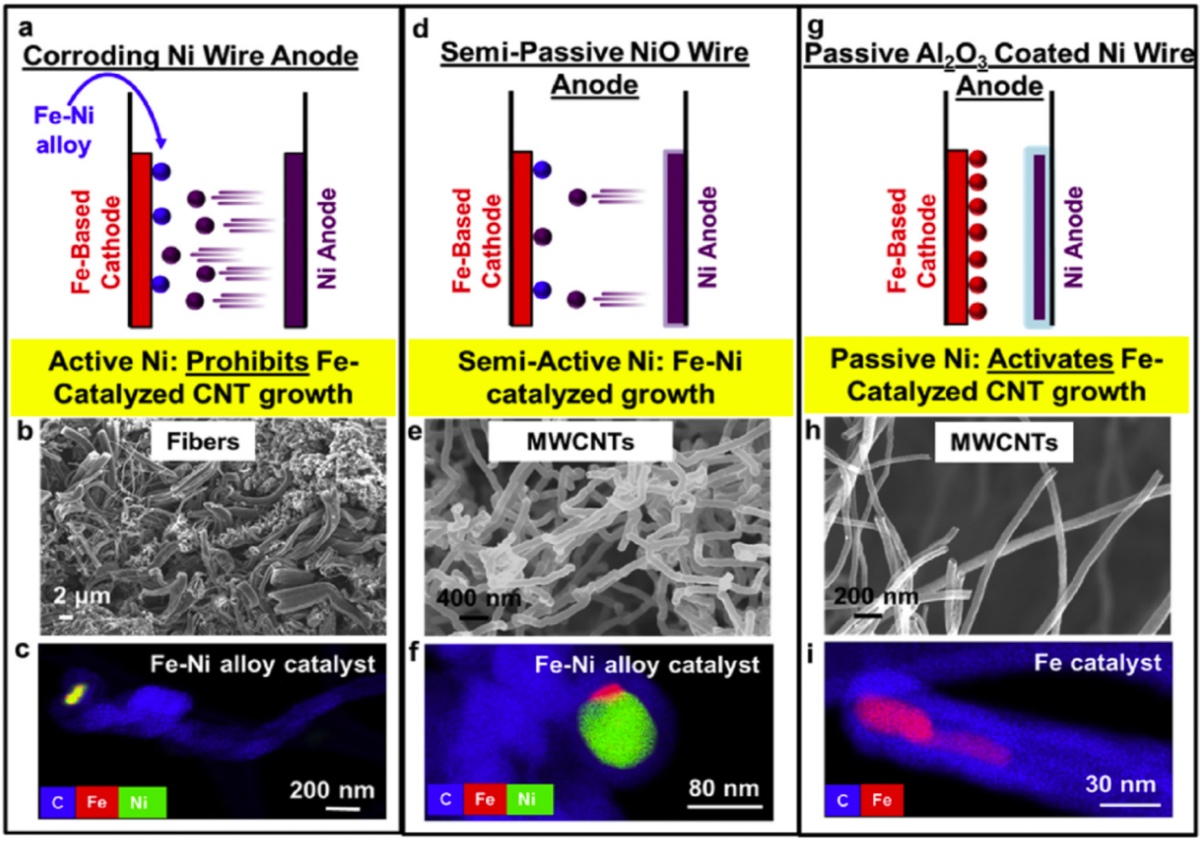


**Figure 19.** Schematic illustrations of the three anodes and their corrosive nature in electrolyte, SEM images of the carbons grown from each anode, and STEM EDS analysis of the catalysts left inside CNTs for (a-c) bare Ni anodes, (d-f) thermally passivated Ni anodes

However, in the case of the ALD coated Ni anode, we observe no signature of Ni in the catalyst particles (which reveals that Ni is sourced from the anode in the previous experiments), and observe only Fe-based catalyst materials positioned at the ends of the MWCNTs. We note that

while previous reports have observed fibers grown with dissolved iron oxide salts in carbonate electrolyte, this is the first report to utilize inherent catalytic properties of the steel substrate and elucidate Fe as the only catalyst, through SEM EDS imaging. As herein we show the anode can be deactivated from taking part in the catalytic process, this allows the CNT growth process to be directly controlled by the composition and properties of the cathode material. In this spirit, we therefore performed a series of experiments using galvanized steel (ZnO coating,>95% Fe), stainless steel ($Cr_2O_3$coating, 72% Fe), and 1010 steel (99% Fe) cathodes. We subjected these electrodes to either high current density (100 mA/cm$^2$) or low current density (25 mA/cm$^2$) and compared the carbon structures produced. As the carbon flux is a parameter commonly associated with gas-phase catalytic CNT growth, the analogous parameter of our system to changing carbon flux is the current density since this controls the rate at which $CO_2$ is split between electrodes. In these three different cathodes, the source of catalytic metal (bulk Fe) will have different accessibility based on the surface coating of the steel that dictates whether it is galvanized, stainless, or 1010. Shown in Fig. 20 are representative SEM images of the carbon products grown on each steel cathode. In all cases, if CNTs are observed, SEM images of these are shown with relative yields overlaid. In all cases carbon is deposited, but here we define relative yield as the concentration of CNTs relative to non-CNT carbon products. These yields were estimated based on SEM analysis of multiple images.

In the case of galvanized steel, we observe under low current densities (Fig. 20a) the formation of 30% CNTs among amorphous carbon, whereas high current densities (Fig. 20b) drive the growth of 99%yield MWCNTs. We attribute this high yield growth to the combined ability to activate the catalyst from beneath the ZnO layer with high current densities, but also sustain catalytic CNT growth in conditions of higher carbon flux.

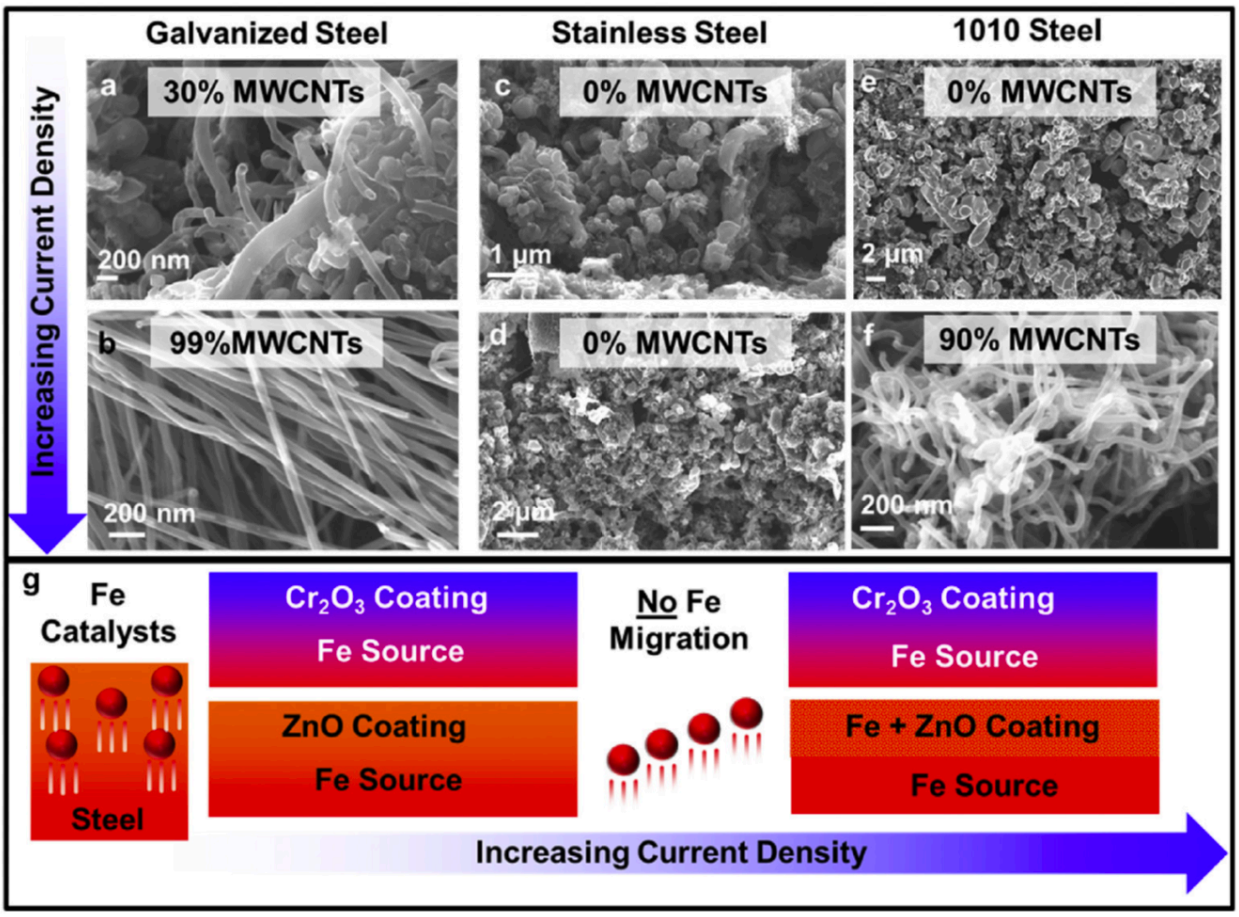


**Figure 20. (**a-f) SEM images of the carbons grown on the three different untreated steel cathodes, at (a, c, e) 25 mA/cm2 and (b, d, f) 100 mA/cm2, and (g) schematic illustration of the mechanism of sourcing Fe from within the steel.

At low current densities, we speculate that a combination of amorphous carbon overcoating of catalytic Fe metal combined with low accessibility of the Fe from the interior of the steel inhibit high yield CNT growth. At higher current densities, faster carbon deposition kinetics and greater Fe migration through the ZnO coating, driven by the increased electric field, to the electrode surface lead to high yield MWCNT growth. This effect was experimentally observed with SEM EDS imaging of the substrate surface before growth, after ten minutes of heating in the carbonate electrolyte, after five minutes of applied current, and after a full hour-long electrolysis. This relationship between current density and metal migration to the surface of the catalyst is

schematically represented in Fig. 20g. On the other hand in the case of the stainless steel cathode (Fig. 20c,d) we observe the formation of amorphous carbon at all current densities, with no CNTs observed. In this case, we conclude the $Cr_2O_3$ layer actively prevents the migration of Fe to the surface of the electrode and drives the formation of amorphous carbon, schematically represented in Fig. 20g. This result also implies that amorphous carbon deposition using galvanized steel electrodes is a result of decreased accessibility of catalytic metal as opposed to the adverse effect of slow carbon deposition on the surface. Finally, we studied carbon products grown on 1010 steel (Fig. 20e,f). We observe no CNTs grown at low current densities on 1010 steel, whereas high current densities drives the formation of MWCNTs as the majority product (90% yield). This trend, consistent with the case of galvanized steel, is attributed to the current-induced Fe diffusion through a native oxide layer to the electrode-electrolyte interface. Whereas previous reports have correlated positive catalytic activity to the zinc coating at the surface of the cathode, in our studies we believe this coating to be inert due to the observance of CNTs grown on 1010 steel, which has no zinc coating. Rather, we attribute the porous oxide coatings on both the galvanized and 1010 steel to aid in the diffusion of Fe to the surface for catalytic activity. We note that in the cases of galvanized steel and 1010 steel where CNTs are observed, some CNTs appear to be partially filled with catalyst metal. Here, as the CNTs are grown *via* tip-growth as supported by TEM imaging, metal filling will be a result of favorable energetics on the CNT interior in agreement with the capillary effect. We also note that during electrolysis experiments, the conductive nature of CNTs enables electrical connectivity between catalyst situated on growing CNTs and the cathode where the Fe metal catalyst is sourced from.

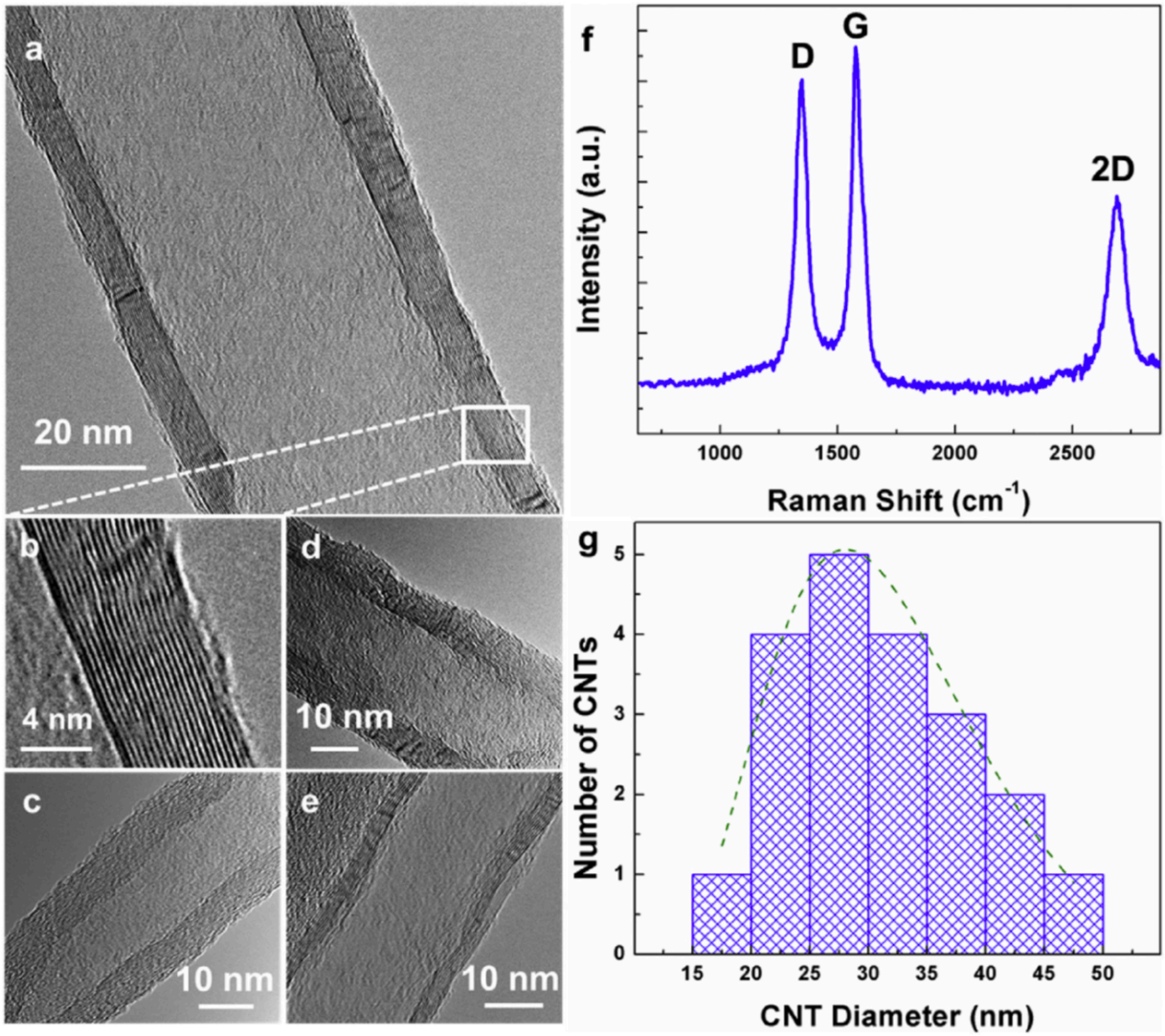


**Figure 21**. (a-e) TEM images of highly crystalline MWCNT grown on untreated galvanized steel cathode with inert Al2O3 coated Ni anode at 100 mA/cm2 including both (b) high resolution image of wall crystallinity, and (cee) a representative selection of CNT products (f) representative Raman spectra, and (g) size distribution assessed through ImageJ using multiple images acquired through TEM

Our results indicate that crystalline MWCNTs are best achieved through growth on the galvanized steel cathodes at high current densities, utilizing Fe catalyst particles accessible from the interior reservoir of iron within the steel. From TEM analysis of MWCNTs grown under these conditions (Fig. 21a-e), we observe highly crystalline, straight graphitic walls. This crystalline nature is further confirmed through Raman Spectroscopy (Fig. 21f), where we observe a sharp G

mode ~1580 $cm^{-1}$, indicative of in plane $sp^2$ hybridized carbons, and a D mode ~1350 $cm^{-1}$, which corresponds to out of plane defective $sp^3$ hybridized carbons. The average ratio of D to G peak intensities across a map of 50 scans is 0.89, consistent with that of graphitic MWCNT spectra. ImageJ image analysis software was used to assess the size distribution of MWCNTs evident in the multiple TEM images to obtain a log-normal distribution of MWCNTs with outer diameter sizes between 15 and 50 nm and an average diameter centered near ~27.5 nm (Fig. 20g). While CVD commonly grows single-walled and double-walled CNTs with smaller diameters than observed in this study, this is likely due to dewetting energetics of catalyst nanoparticles at a gas-solid interface. In our study, the catalyst particle dewetting occurs at a solid-liquid interface which controls particle size prior to CNT nucleation. Notably, we observe a log-normal diameter distribution of CNT diameters grown in our process that is a similar to the CNT diameter distribution shape in gas phase CVD growth where it is well accepted that CNT diameter is correlated to the catalyst nanoparticle size.[170] This range of CNT diameters is consistent with those produced in many gas phase processes, but represents a significant decrease from existing prior work on $CO_2$-derived CNTs, where the products exist as large diameter materials with diameters 150+ nm, and generally mixed with other non-CNT products.

## 4.4 Conclusions

In this study we demonstrate the synergy between traditional gas phase CNT growth mechanisms and electrolytic growth of CNTs by leveraging an electrode design strategy to understand and direct the catalytic process toward iron-catalyzed growth. We show the ability to capture $CO_2$ and electrochemically convert this into highly crystalline MWCNTs with an average diameter of 27.5 nm and a high degree of crystallinity by leveraging iron based CNT catalysts for

the first time. This builds on using ALD to produce a passive alumina coating on the Ni anode surface to inhibit mass transfer and isolate Fe as a primary catalyst species at the cathode where CNTs are grown, and engineer the surface properties of the Fe-containing cathode to optimize the accessibility of internally-contained catalyst material. Whereas previous works have studied the interplay between cathode surface properties and *in-situ* deposited catalytic particles,[60] herein we present the first study of catalysts inherent to the cathode materials, which can either be activated or deactivated, based on the engineered surface properties of the anode. SEM, TEM, and Raman spectroscopic imaging reveals the ability to produce highly crystalline CNT materials with high yield of 99% relative to other carbon products, and touting a CNT diameter distribution that intersects products formed in state-of-the-art traditional gas phase CNT processes. As decades of gas-phase CNT research has lead to the understanding that catalyst size and support layer dictate CNT growth, future works to modulate catalyst size to achieve smaller diameter CNTs and study the influence of catalyst support are of interest. More significantly, this work provides the first intersection between concepts present among the vast community of researchers studying gas phase CNT growth and the concepts and mechanisms behind the electrolytic growth of CNTs from ambient carbon dioxide.

# Chapter 5

## Sustainable Capture and Conversion of Carbon Dioxide into Valuable Multiwalled Carbon Nanotubes Using Metal Scrap Materials

Adopted from: **A. Douglas**, N. Muralidharan, R. Carter, C. L. Pint, "Sustainable Capture and Conversion of Carbon Dioxide into Valuable Multiwalled Carbon Nanotubes Using Metal Scrap Materials," ACS Sustainable Chemistry & Engineering, 5, 7104-7110 (2017) *with permission from the American Chemical Society*

### 5.1 Introduction

Two of the main global challenges faced by modern society include increasing amounts of atmospheric carbon pollution and the growing footprint of low-value non-degradable materials which are not recycled and are dumped into landfills. The first case, which is implicated as a main contributor to global climate change,[171] is addressed by the conversion of atmospheric $CO_2$ into stable products to form a carbon-neutral economy.[137, 172, 173] The United States alone emits over 5 million kilotons of $CO_2$ each year, which could potentially be a chemical feedstock for the production of functional materials, if appropriate conversion processes are realized.[172] In the second case, scrap metals represent > 130 million tons of waste each year and among the top contributors to this number is both steel and brass.[174, 175] Despite modern recycling efforts,[176, 177] a significant portion of these are not recycled (~ 17.5 million tons of steel[178] and ~ 1.1 million tons of brass[175]) and end up in landfills as non-degradable waste.

To overcome atmospheric carbon pollution, $CO_2$ conversion processes close the carbon loop to recycle and repurpose this greenhouse gas into useful chemicals and materials. The electrochemical conversion of $CO_2$ into alcohols and hydrocarbon fuels has been a highly active

area for research under the promise of a viable secondary market for otherwise pollutant greenhouse gases.[160, 162-164, 179] However high operating costs, the need for expensive catalyst materials that can't be developed from abundant sources, and low conversion efficiencies stand in the way of practical commercial viability for these techniques.[180, 181] On the other hand, the deposition of carbon from $CO_2$ using molten salt electrolysis to produce stable carbon products is an alternative to the production of fuels. This approach dates back to the 1960's where carbon was first deposited onto a gold electrode using molten salt electrolysis.[182] Compared to low-efficiency conversion to fuels, which is both carbon positive and generates a product whose value is correlated with further $CO_2$ generation, this approach gives promise to stable carbon-based products which can be processed into components used for high value consumer technologies. However, only recently has this approach been applied to the synthesis of nanostructured carbons, and limitations reflect lack of understanding of the chemistry and electrochemistry of the combined electrolyte and electrodes. While some groups have observed the effects of electrolyte composition or temperature on the resulting carbon structures,[30, 183-186] the strongest influence of carbon-structure control appears to be the cathode structure and composition,[54, 60, 187, 188] a concept consistent with gas-phase chemical synthesis routes.[189] Early efforts in the growth of carbon based nanostructures from molten carbonates observed growth activity linked to *in-situ* deposition[54, 190] and/or corrosion of the metal anode. Recently, our prior efforts have demonstrated routes to passivate the corrosive anode and selectively exploit Fe catalytic metal in the cathode for the first time. This leverages understanding from the traditional gas-phase CNT growth community, which has demonstrated Fe catalysts to be the most efficient for high quality CNT synthesis.[43-46, 49, 191-195] However, unlike gas-phase growth processes, electrochemical growth requires conductive electrode surfaces and chemical stability in the carbonate electrolyte.

In this regard, low-cost metal alloys are an ideal electrode to study the electrochemical conversion of $CO_2$ due to stability in molten carbonates and excellent conductivity. These materials offer a low carbon footprint compared to highly precise catalyst layers prepared using energy-intensive methods, and in the case where purity is not critical, can be sourced at virtually no additional cost. Conductive metal substrates, such as stainless steels, have also actively been utilized in gas phase carbon nanotube growth techniques due to the presence of a majority of Fe catalyst that can be tapped for CNT synthesis.[196-201] However, lack of understanding of the interplay between the cathode and anode and their role in the catalytic products has hampered an understanding of what electrode materials can or should be used for the catalytic conversion of $CO_2$ into functional carbon nanostructures.

In this study, we present findings generalizable to a wide range of low-cost multicomponent metal alloys that demonstrate for the first time that low-cost multicomponent scrap metals can be used to electrochemically synthesize MWCNT materials from ambient carbon dioxide as catalytically active cathodes. Electron microscopy maps indicate that in the case of both (1) Fe-rich metals, and (2) Fe-free metals where Fe exists as an impurity at or below 1 wt.%, that molten salt electrolysis leads to the segregation of Fe or Fe-Ni nanoparticles to the surface of the alloy that facilitate MWCNT growth. We further demonstrate the direct growth of MWCNTs from ambient carbon dioxide on the surface of scrap metal pieces with arbitrary shape and size, including pipes and shavings. This work indicates that under appropriate process conditions and when combined with a non-corrosive anode, virtually *any* metal alloy stable in molten carbonates can be viable candidates as cathodes in the conversion of ambient $CO_2$ into CNTs either from primary or impurity components.

## 5.2 Experimental Details

### *5.2.1 Electrode Preparation*

An $Al_2O_3$ coated Ni wire (Fisher Scientific, 99%, 1 mm diameter) anode was used in all electrolysis experiments. Ni wire was coated with 500 cycles (~ 50 nm) of $Al_2O_3$ by a Gemstar Arradiance atomic layer deposition (ALD) tool. The thickness of this coating was determined through ellipsometry analysis of $Al_2O_3$ coatings on silicon wafers with a J.A. Woollam spectrometer. To accomplish this, we utilized sequential 28 ms pulses of $C_6H_{18}Al_2$ (TMA) and $H_2O$ with a residence time of 1 second. This electrode can be used for multiple experiments. The cathodes used in these experiments were scrap metals including steel and brass that were retrieved from a scrap yard (PSC Metals). The structures utilized in this study included shavings taken from yellow brass and 316 Stainless Steel, screws, and pipes.

### *5.2.2 Electrolysis*

Experiments were carried out in an alumina crucible (AdValue Tech, 50 ml) containing 40 g lithium carbonate (Fisher Scientific, 99%) electrolyte, which was held at 750 °C (M.P. 723 °C) in a cylindrical ceramic heater (Thermcraft) using a bench top temperature controller (OEM Heaters). Electrodes were immersed into the electrolyte and a constant current was applied across the electrodes. The current density is normalized to the approximate exposed surface area of the cathode. All electrolysis experiments in this study were carried out for 1 hr. We observe no degradation of the lithium carbonate electrolyte and reused the same batch for five consecutive experiments before discarding. During the electrolysis, carbon accumulates at the cathode, which is removed from electrolyte and cooled after electrolysis. Carbon product was removed from the

electrodes by bath sonication in water (1 hr), and purified from carbonates *via* washing in 2 M HCl (which is strong enough to dissolve carbonates without removing all catalyst materials embedded within CNTs), and solvent exchanged to water through centrifugation. As Fe and Ni dissolve in strong acids, treatment in more concentrated acidic solutions can be used to separate the catalyst materials from the CNTs. The carbon was dried at 60 °C overnight.

### *5.2.3 Material Characterization*

The carbon nanostructures were analyzed with a Zeiss Merlin scanning electron microscope (SEM) and an FEI Osiris transmission electron microscope (TEM) at a beam voltage of 200 kV with corresponding elemental mapping by energy dispersive x-ray (EDS) technique to determine catalyst composition. Cathode surfaces were characterized through SEM EDS. The crystallinity of the carbon nanostructures was determined by Raman spectroscopy on a Renishaw inVia microscope with a 532 $nm^{-1}$ laser excitation, 10 seconds exposure time, and 10% laser power. Thermogravimetric analysis was carried out using a TGA Instrument Specialists TGA 1000 to characterize the relative wt.% of CNTs to residual catalysts.

## 5.3 Results and Discussion

The general process of electrochemical reduction of $CO_2$ to CNTs *via* molten salt electrolysis relies on the splitting of the molten $Li_2CO_3$ (M.P. 723 °C) electrolyte into C, which collects at the cathode, $O_2$ collected at the anode, and resulting $Li_2O$ in the electrolyte. $Li_2O$ then reacts with ambient $CO_2$ to regenerate the $Li_2CO_3$ electrolyte. This occurs under the application of a constant current of 100 $mA/cm^2$ between a scrap metal cathode and a reusable inert $Al_2O_3$ coated Ni wire anode, which we have previously demonstrated as an ideal anode allowing the

activation of catalysts which are contained on-site at the cathode material.[189] Here, we exploit this idea to explore how a class of conductive and extremely low-valued materials often discarded from scrap yards into landfills, and hence exhibiting negligible carbon footprint, can be repurposed as consumable cathodes for the catalytic synthesis of carbon nanotubes from atmospheric carbon dioxide.

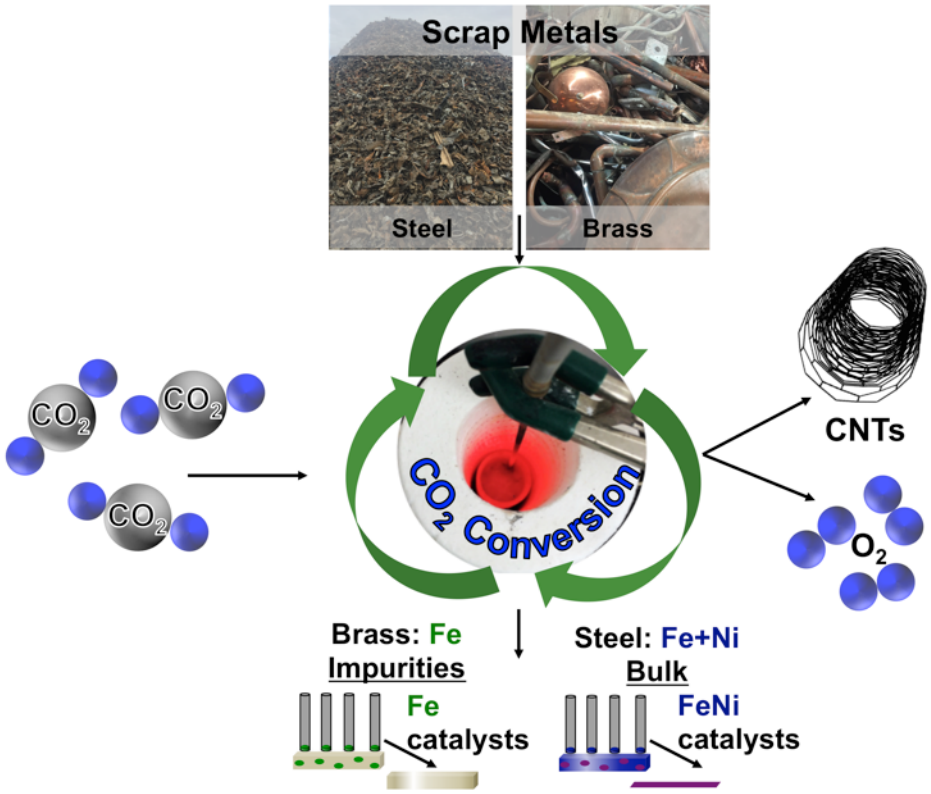


**Figure 22**. Schematic representation of the general process of CO2 conversion using scrap metals as electrodes, and CO2 as chemical feedstock for the production of CNTs, and recycling of scrap brass and steel by purification or consumption

In this regard, we chose two representative scrap metal materials – neither of which have been studied for CNT growth from molten salt electrolysis, but that give a general representation of (1) a metal cathode containing a significant amount of Fe metal on the interior (stainless steel) or (2) a metal cathode that contains catalytic Fe metal only as impurities of processing (brass). In each case, the output of electrolysis is either a mostly consumed cathode (stainless steel), or a

cathode that is purified of impurities (brass) to yield elemental copper and zinc that are inactive in this process. This idea is schematically represented in Figure 22. In turn, this work is therefore relevant to a broad class of multi-element metals that either contain Fe as a primary element, or do not contain Fe except as impurities in the metal alloy matrix.

Whereas decades of research on gas-phase CNT growth has elucidated the critical step of catalyst formation that is necessary to precede CNT growth,[167, 168] we performed experiments to study the evolution of the scrap brass and scrap stainless steel surfaces in the environment where CNT growth takes place using scanning electron microscopy (SEM) elemental mapping. Three cases were compared, (1) untreated metals, (2) after heat treatment to 750 °C in $Li_2CO_3$ for 15 minutes, and (3) after 5 minutes of initial applied current (Figure 2). For stainless steel (Figure 2a), we observe a surface mostly comprised of well-distributed Cr, Fe, and Ni initially with little change for the electrodes heat treated in molten carbonates. However, we observe the formation of prominent Fe-Ni islands, which are both catalytically active materials, on the surface after initial applied current. Similarly for brass, the untreated surface is comprised of only Cu and Zn, with no evidence of Fe. After heat treatment to 750 °C, the Cu and Zn begin to dealloy since the melting point of Zn is below 750 °C. During dealloying, Fe impurities from within the bulk of the brass become present at the surface of the scrap steel, as shown in Figure 23b. These Fe islands become more prominent after 5 minutes of initial applied current, and the presence of Fe particles at the surface of scrap brass is the basis for catalytic activity, even in a case where Fe is only an impurity component.

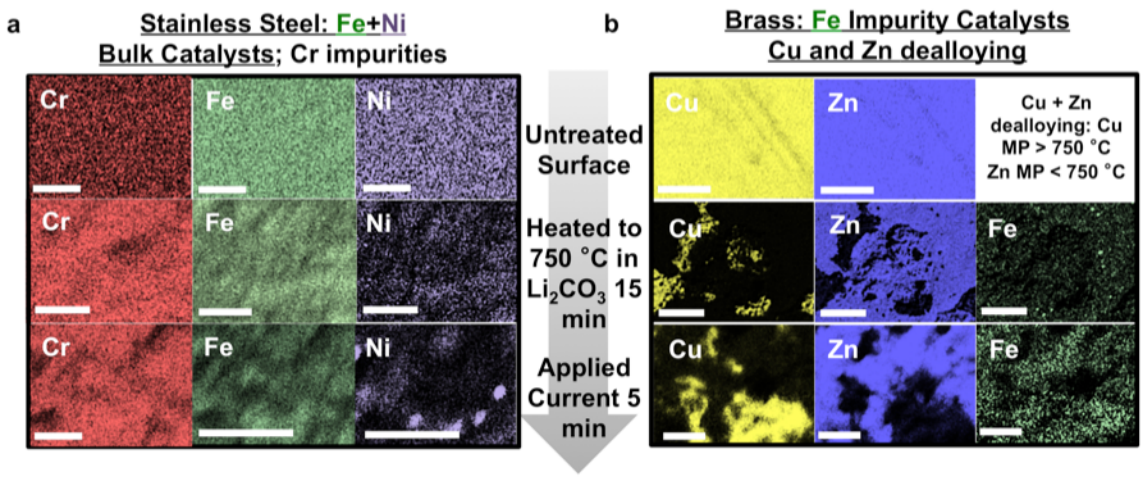


**Figure 23**. SEM EDX maps of electrode surfaces for (a) stainless steel and (b) brass throughout the electrolysis process. Shown from top to bottom are the untreated surfaces, the electrodes after heat treatment, and then after applied current. All scalebars are 2.5 μm.

Further, unlike the planar two-dimensional electrodes that have been used for previous efforts of carbon nanostructure growth through $CO_2$ electrolysis, the use of scrap metals requires electrodes that can be purposed from irregular materials. In this regard, we used recovered scraps and objects based from both stainless steel (316) and brass (yellow brass) that represent a diverse set of irregular shapes and sizes, including pipes, screws, and shavings (Figure 24). Shown in Figure 24 is the untreated scrap, the MWCNT-coated scrap after undergoing $CO_2$ capture and conversion process, and the resulting carbon products after removing excess carbonate in a dilute HCl wash. From all three stainless steel electrodes, we observe the formation of MWCNTs (Fig. 24a-c), attributed to the catalytic activity of the Fe and Ni particles from within the bulk of the metals. In the case of scrap brass, we observe the formation of CNTs with the brass shaving, but other objects including the screw and pipes led to the catalytic formation of other nanostructured carbons, such as nano-rotini and carbon nanofibers. This could be attributed to the possibility that impurities in a shaving are likely to be more concentrated near the surface of the shaving due to

the material processing required to form the shaving. However, SEM EDS characterization of these materials in an untreated state was inconclusive due to the lack of a prominent Fe signature prior to the heat treatment of these materials. In any case, this indicates that a material that natively does not contain Fe can still be catalytically active in the growth of CNTs from Fe that segregates to the surface during thermal and electrochemical processing.

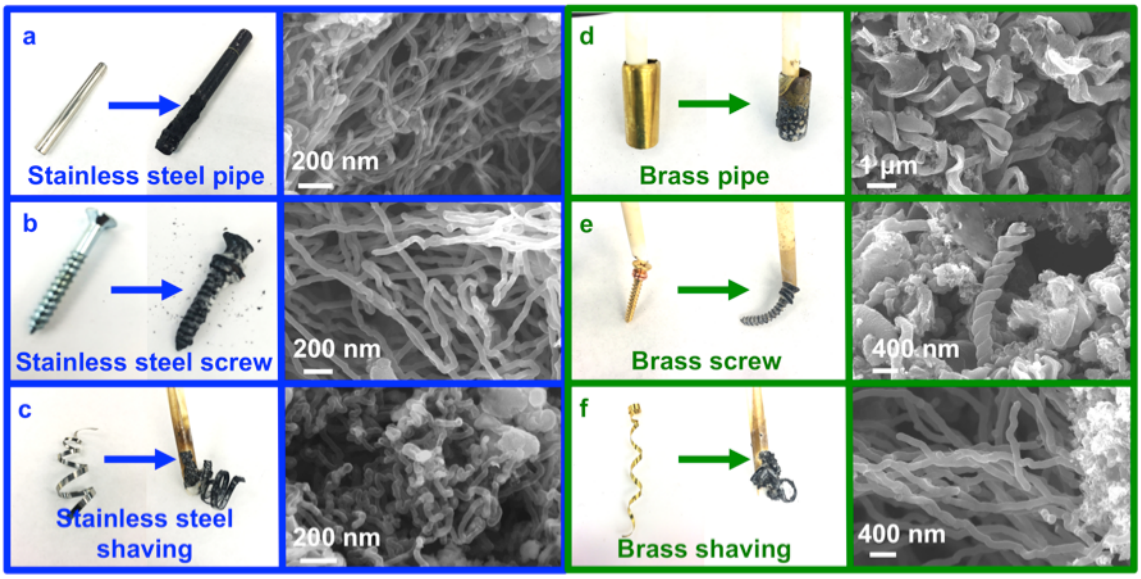


**Figure 24.** Steel scraps before and after electrolysis carbon coating and SEM images of the carbon products including (a) pipes, (b) screws, and (c) shavings. Also shown are the brass samples including (d) pipes, (e) screws, and (f) shavings.

Raman spectroscopy was used to characterize the carbon products, which all exhibit the characteristic graphitized carbon G peak ~ 1580 $cm^{-1}$, indicative of in-plane $sp^2$ hybridized carbons, and a D mode ~ 1350 $cm^{-1}$, which corresponds to out of plane defective $sp^3$ hybridized carbons. A higher D/G peak intensity ratio is observed for CNTs and carbon nanomaterials grown from brass compared to stainless steels, which indicates a greater concentration of $sp^3$ carbon materials (Figure 25a). Diameter distributions of CNTs were taken from image analysis using

multiple SEM images from multiple spots on the sample (Figure 25b) and indicate the brass-grown CNTs have a wider and larger size distribution compared to the stainless steel-grown CNTs. Based on the outer diameter, CNTs grown from a stainless steel shaving exhibit a tight size distribution from ~ 18-47 nm, centered at ~ 29 nm. In the case of the CNTs grown on the brass shaving electrode, we observe a wider size distribution from ~ 65-174 nm, with a peak centered around ~ 125 nm. We attribute the larger CNTs from brass to the high Fe mobility in the molten Zn that lowers the surface free energy of nanoparticles through coarsening, which in turn leads to larger diameter CNTs. As many previous studies on catalytic mechanisms that influence gas-phase CNT growth have elucidated the catalyst size, structure, and coarsening rate to the resulting CNT properties, we speculate that the most effective means to modulate CNT properties using this electrochemical growth technique is also through catalyst design.

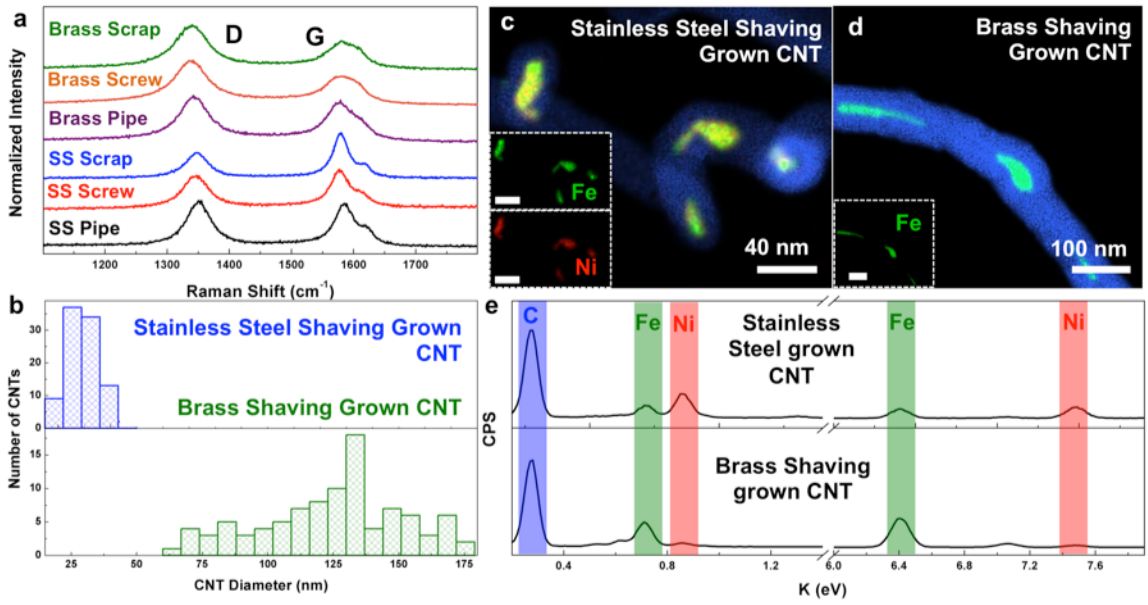


**Figure 25**. (a) Raman spectra of all samples, (b) size distribution plots of CNTs produced from stainless steel and brass shavings, STEM EDX maps of CNTs with embedded catalysts from (c) stainless steel shavings and (d) brass shavings, with insets of the catalyst metals and (e) energy spectra of the embedded catalyst.

Whereas previous imaging isolated the catalyst formation prior to CNT nucleation and growth, we further performed post-mortem STEM EDS imaging of the CNT materials to correlate the synthesis product and the chemical identity of the catalyst particles that remain embedded in the CNTs to validate prior observations. This is due to the idea that only those elements that participate catalytically (despite many elemental impurities present in the metal alloys) in CNT growth will be embedded in the CNTs following growth. The resulting compiled STEM EDS maps are shown in Figures 25 c-d, with individual elemental maps of the catalysts shown as insets. In the case of the stainless steel shaving-grown CNTs, we observe the presence of a Fe-Ni alloy nanoparticle catalyst that is responsible for the catalytic growth of CNTs, further confirmed with EDS spectra shown in Figure 25e showing C, Fe, and Ni presence. We note that as 316 stainless steel is alloyed with 2-3 wt.% Mo to enhance corrosion resistance and resist thermal degradation, and previous gas-phase CNT growth studies have seen enhanced catalytic activity with the addition of Mo present in the catalyst,[48] the Mo present in this system could lead to enhanced catalytic behavior. However, in the case of the brass shaving-grown CNT, we only observe the presence of Fe on the interior of the CNT, and in the EDS spectra. In both cases, we observe the catalysts embedded within the CNTs and residing at the tips. This result confirms our hypothesis that catalysts can be consumed from primary elements (Fe and Ni) within scrap stainless steel and consumed from impurity species (Fe) in brass as catalysts for CNT growth from $CO_2$.

Building from Raman spectroscopy and SEM imaging that give statistical assessments of the CNTs produced, we performed HR-TEM imaging of representative CNTs synthesized from both stainless steel and brass scraps (Figure 26) to give insight into the representative crystallinity and wall quality of the synthesized CNT materials. Consistent with the results from Raman

spectroscopy, we observe a better degree of crystallinity for CNTs synthesized using stainless steel scraps (Figs. 26a-b) compared to those using brass scraps (Figs. 26c-d).

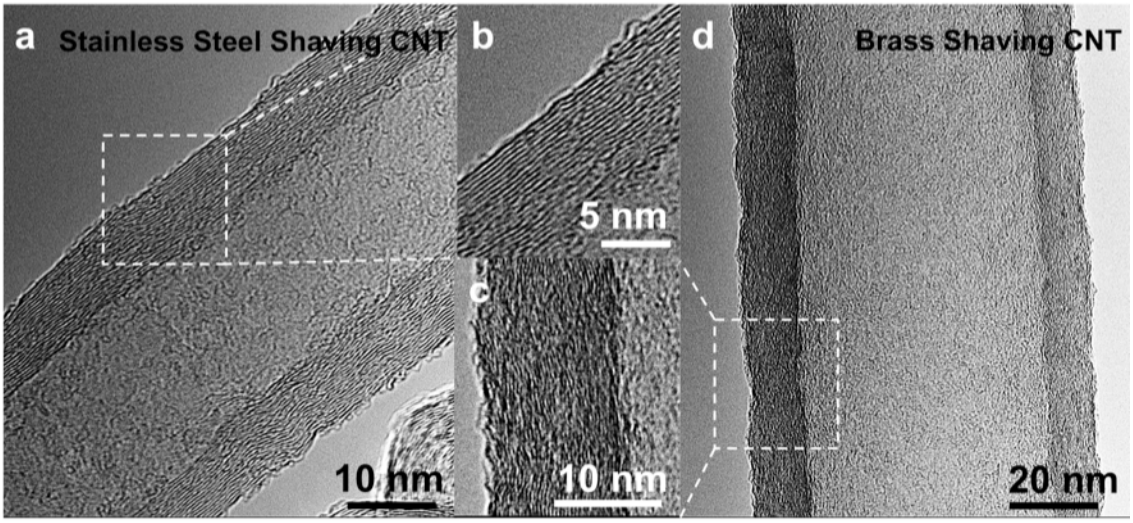


**Figure 26.** Representative TEM images of CNTs grown from (a, b) stainless steel shavings, and (c, d) brass shavings, with (b) and (c) demonstrating wall crystallinity of respective CNTs.

To further characterize and understand the scrap metal consumption from electrolysis, thermogravimetric analysis (TGA) was carried out on the scrap metal-grown CNTs. We previously reported the calculated $CO_2$ conversion at 84 g carbon per kilowatt-hour of applied electricity between the electrodes based on 100% efficiency and a standard reduction potential of 1.33 V.[189] In the case of the scrap steel, we observe ~ 27 wt.% residual catalyst metal following the burning of carbon materials near 600 °C. This correlates to an approximate 31 g scrap metal (Fe + Ni bulk) consumed for every 84 g carbon produced per kilowatt-hour of electricity, whereas the brass-grown CNTs present a case where 8 wt.% residual catalyst corresponds to approximately 7.3 g scrap metal (Fe impurities) consumed. We can also utilize TGA analysis to calculate how many consecutive electrolysis experiments are required to fully consume catalyst materials

embedded with the bulk of the scrap metal alloys. In the case of the stainless steel, where Fe and Ni can make up anywhere from 68-88 wt.% of the alloy, consecutive hour-long experiments can be ran 10-13 times to fully consume the Fe and Ni elements from the bulk of the steel. However, one hour-long electrolysis removes all 1 wt.% of Fe impurities from within the brass-based electrodes. This is consistent with the notion that steel presents a case of the bulk of the material *consumed*, whereas the brass is *purified* from impurities in this process. We also noted surface changes of the electrodes post-electrolysis, characterized by SEM EDX. We observe that in the case of the steel, the relative concentrations of Fe and Ni to other elements present including O and Cr slightly diminish compared to the concentrations prior to electrolysis, consistent with our findings of Fe and Ni consumed as catalysts within the CNTs. However, the brass scrap demonstrates a large change in elemental concentrations, where the untreated brass has ~ 2X the concentration of Cu relative to Zn, which increases drastically to over 8X in the post-electrolysis brass. This finding is also consistent with our observations of dealloying due to an operating temperature that is between the melting temperatures of the two elements. This implies the possibility to purify the brass by consuming the Fe impurities in addition to dealloying the brass alloy to form a higher value raw material (Cu).

On a final note, compared to conventional routes for CNT synthesis which are not only energy intensive in materials preparation but result in significant atmospheric emissions due to the thermal formation of stable carbon reaction byproducts, such as methane, our approach yields the production of CNTs from $CO_2$ with only $O_2$ emission byproducts. Through the use of scrap metal catalyst layers and low-emission energy sources, the route we describe has the potential to produce an overall carbon negative scheme for carbon sequestration and conversion. Whereas cheap solar cells are reaching levels of carbon neutrality, further improvement in low-energy silicon

processing can be a viable approach for a carbon-negative process. Further, combining this approach with geothermal or other carbon negative energy production techniques has the potential to not only enable carbon negative sequestration and conversion of carbon dioxide, but also the production of a high value commodity (with market values > $100/kg for MWCNT and $2,000/kg for SWCNT)[202] of significant technological interest arising from the nanoscale features of CNTs which are unique compared to other micrometer-scale feature carbon-based markets (with the market value of carbon fiber at $22/kg). Compared to alternative carbon conversion techniques, electrochemical conversion of $CO_2$ mediated by molten carbonate salts results in Coulombic efficiencies approaching 100%, resulting in a CNT yield directly comparable to the energy input for electrolysis. Furthermore, the energy requirement for this technique is significantly lower than gas-phase processes,[16, 203] with the only energy inputs arising from energy required to bias the electrodes (as low as 43 MJ/kg) and heat the electrolyte (as low as 30 MJ/kg). For comparison, previous reports have estimated a total energy requirement of ~ 5,816 MJ/kg for high-pressure carbon monoxide based growth, 482 MJ/kg for floating catalyst chemical vapor deposition growth, and 954 MJ/kg for fluidized bed gas-phase reactions.[203] Our findings, which are broadly applicable to a range of low-valued multicomponent metal scraps, support the promise of carbon-negative sequestration and conversion of carbon dioxide into high value CNT materials.

## 5.4 Conclusions

In summary, we demonstrate the general principle that conductive scrap metals can be used as catalytic growth cathodes for CNTs through the interaction of $CO_2$ in air with molten salts that provides the carbon source. Our results demonstrate this in the context of cathodes primarily composed of catalytic Fe metal (stainless steel) as well as cathodes that do not natively contain

catalytic Fe metal except through impurities (brass). SEM EDS measurements confirm the formation of catalytic metal islands on the surface of the metal during thermal and electrochemical treatment in both cases that provide the basis for nucleation of MWCNTs. We measure an average diameter of ~ 29 nm in the case of the steel scrap-grown CNTs, and ~ 126 nm for the brass scrap-grown CNTs. Raman spectroscopy and TEM characterization reveals a higher crystallinity of CNTs grown from stainless steel scraps compared to brass scraps, and TGA measurements verify the wt.% of residual catalyst metals within the CNTs, and the ability to consume scrap metals (as either bulk or impurities) through this process. Overall, our work demonstrates how low-value scrap metals can be valuable consumable templates for the production of stable and functional MWCNTs by the conversion of carbon dioxide scavenged from the atmosphere.

# Chapter 6

## Toward Small-Diameter Carbon Nanotubes Synthesized from Captured Carbon Dioxide: Critical Role of Catalyst Coarsening

Adopted from: **A. Douglas**, R. Carter, M. Li, C. L. Pint, "Toward Small-Diameter Carbon Nanotubes Synthesized from Captured Carbon Dioxide: Critical Role of Catalyst Coarsening," ACS Applied Materials & Interfaces, 10, 19010-19018 (2018) *with permission from the American Chemical Society*

### 6.1 Introduction

Due to their impressive mechanical, electronic, and thermal properties, carbon nanotubes (CNTs) have been at the forefront of research and technological development for nearly two decades.[31, 32, 34, 43, 45, 46, 48, 66, 204] These extraordinary physical properties are attributed to their atomic structure and size, motivating a significant body of work focused on understanding the mechanisms of CNT growth that govern their resulting structure.[50, 66, 167, 168, 191, 204-211] The structure and diameter of a nanotube significantly influences its mechanical and electronic properties,[206] and thus can impact its performance in a variety of applications.[32, 212, 213] Furthermore, small diameter CNTs including few-walled (*ca.* 3-10 walls), double-walled, and single-walled CNTs have higher economic value due to their enhanced physical properties, broader appeal toward applications, and greater difficulty in synthesis compared to their larger diameter counterparts possessing greater wall numbers.[214-216]

Decades of gas-phase CNT growth research, most recently leveraging state-of-the-art *in-situ* TEM techniques, have determined a strong correlation between the size of the catalyst particles and the diameter of the resulting CNTs.[68-70] This understanding has enabled diameter distribution

control, which can be most easily realized by tuning the thickness of the deposited catalyst layer to control dewetted particle sizes.[55] Furthermore, catalyst size[43, 206, 217, 218] and dynamic evolution of size due to catalyst coarsening,[50] catalyst diffusion,[204] and mechanically driven collective growth termination,[51-53] enable a collective understanding of growth and termination during gas phase processes. This challenge of maintaining small diameter catalysts during growth duration has motivated growth processes such as water-assisted and short-duration "supergrowth" which has been shown to overcome these deactivation mechanisms.[44, 46]

From a general perspective, gas-phase CNT growth occurs as a carbon-containing precursor gas passes over the surface of a catalytic nanoparticle, decomposes on the particle surface, and precipitates from the particle as graphitic carbon.[59] In contrast, the electrochemical reduction of $CO_2$ to produce CNTs has only recently been reported and discussed, and utilizes electrochemistry between two biased electrodes to dissociate a carbonate species and deposit elemental carbon onto a surface. In this process, catalyst evolution and carbon deposition from $CO_2$ feedstock are decoupled due to the addition of electrochemical controls that determine global synthesis parameters such as carbon flux independently from the activity on the catalyst surface. Whereas the origin of this technique to sequester $CO_2$ and produce amorphous carbon deposits dates back to the early 1960's,[182] the growth of CNTs requires the additional control of the deposited carbon to sites where CNTs can by synthesized – a concept that has only recently been demonstrated.[54, 60, 72, 173, 189, 219] Early observations of hollow carbon fiber materials with diameters > 100 nm relied on the *in-situ* deposition of primarily nickel catalysts from corroded metal anodes onto the cathode,[54, 60, 72] which favored this architecture over spherical carbon particles,[24, 182, 184, 220] flakes,[25, 26] or other carbon structures[221] previously reported. However, the stochastic nature by which such *in-situ* catalyst is formed, among other limitations, results in CNT materials possessing

larger diameters (> 100 nm) and lower quality than CNTs produced by other scalable methods, such as fluidized bed CVD. Recently, our work has demonstrated that by passivating the anode from corrosion, thereby eliminating the detrimental *in-situ* catalyst formation, we can isolate control of catalysts sourced from the cathode, yielding CNTs with diameters near ~ 30 nm (versus > 100 nm otherwise) and of moderate quality comparable to gas-phase processes.[189] This also enables isolation of the catalyst formation and synthesis steps to a single electrode, as opposed to two electrodes during *in-situ* catalyst formation. This gives promise toward routes intersecting state-of-the-art methods for diameter and chirality control, such as with high melting point metal catalysts, while retaining the cost-effective and scalable versatility and sustainability that builds from this electrochemical technique.

In this spirit, the aim of this study is to elucidate mechanisms that control electrochemical CNT growth in the context of the catalyst-support layer architecture that has been effective for the high yield growth of CNTs using gas phase approaches. To accomplish this, we study Fe metal catalyst deposited at different thicknesses (0.5 nm to 5 nm) onto a passive stainless steel cathode which is paired with a passive oxygen evolving Ni anode to achieve electrochemical CNT growth originating from the cathode. Upon heating, we demonstrate dewetting of the Fe catalyst and electrochemical reduction that leads to CNT growth correlated with catalyst particle diameter. However, time dependent studies of CNT diameters elucidate rapid Ostwald ripening that limits diameter control over long growth durations that give promise to higher yield. Nonetheless, our results at short growth durations indicate some double-walled CNTs among a population of small diameter CNTs. This work provides a blueprint toward achieving high valued single-walled CNTs using this electrochemical approach, and syncs the challenges that remain pertinent for diameter control in gas-phase CNT growth with those in this electrochemical technique.

## 6.2 Experimental Details

### *6.2.1 Electrode Preparation*

An $Al_2O_3$ coated Ni wire (Fisher Scientific, 99%, 1 mm diameter) anode was used in all electrolysis experiments. Ni wire was coated with 500 cycles (~ 50 nm) of $Al_2O_3$ by a Gemstar Arradiance atomic layer deposition (ALD) tool. The thickness of this coating was determined through ellipsometry analysis of $Al_2O_3$ coatings on silicon wafers with a J.A. Woollam spectrometer. To accomplish this, we utilized sequential 28 ms pulses of $C_6H_{18}Al_2$ (TMA) and $H_2O$ with a residence time of 1 second. The inert nature of this electrode is demonstrated by its ability to be reused for multiple experiments. The cathodes used in these experiments were 316 stainless steel (Trinity Brand Industries) sheets with thin layers of Fe deposited *via* e-beam evaporation using an Angstrom eBeam and Sputter Tool.

### *6.2.2 Electrolysis*

Experiments were carried out in an alumina crucible (AdValue Tech, 50 ml) containing 40 g lithium carbonate (Fisher Scientific, 99%) electrolyte, which was held at 750 °C (M.P. 723 °C) in a cylindrical ceramic heater (Thermcraft) using a bench top temperature controller (OEM Heaters). Electrodes were immersed into the electrolyte and a constant current was applied across the electrodes. The current density is normalized to the approximate exposed surface area of the cathode. All electrolysis experiments in this study were carried out for 1 hr unless otherwise noted in the text. We observe no degradation of the lithium carbonate electrolyte and reused the same batch for five consecutive experiments before discarding. During the electrolysis, carbon

accumulates at the cathode, which is removed from electrolyte and cooled after electrolysis. Carbon product was removed from the electrodes by bath sonication in water (1 hr), and purified from carbonates *via* washing in 2 M HCl, and solvent exchanged to water through centrifugation. The carbon was dried at 60 °C overnight.

### *6.2.3 Material Characterization*

The carbon nanostructures were analyzed with a Zeiss Merlin scanning electron microscope (SEM) and an FEI Osiris transmission electron microscope (TEM) at a beam voltage of 200 kV with corresponding elemental mapping by energy dispersive x-ray (EDS) technique to determine catalyst composition. Diameter distributions were assessed by taking measurements of > 100 CNTs from multiple SEM images at multiple different spots. In the case of the 3 min growth samples, diameter distributions were assessed by a combination of SEM and TEM imaging, to account for the population of CNTs that are too small to measure from SEM techniques. Cathode surfaces were characterized through SEM EDS. Raman spectroscopy was used to determine CNT crystallinity on a Renishaw inVia microscope with a 532 $nm^{-1}$ laser excitation, 10 seconds exposure time, and 10% laser power. All samples were purified through suspension in sodium dodecylbenzene sulfonate (SDBS, Fisher Scientific) and centrifugation for 15 minutes at 2000 rpm for Raman characterization.

## 6.3 Results and Discussion

The electrochemical reduction of $CO_2$ to CNTs *via* molten salt electrolysis has been previously described[189] and relies on the splitting of the molten $Li_2CO_3$ (M.P. 723 °C) electrolyte into C, which collects at the cathode, $O_2$ collected at the anode, and $Li_2O$ in the electrolyte. $Li_2O$

regenerates the $Li_2CO_3$ electrolyte through a chemical reaction with ambient $CO_2$. This takes place under constant current of 100 mA/cm$^2$ applied between a conductive stainless steel-based cathode and inert $Al_2O_3$ coated Ni wire anode, which we have demonstrated as an ideal reusable oxygen-evolution anode that enables metal at the cathode-electrolyte interface to moderate the catalyst activity.[189] However, despite the expectation that some of the conventional ideas guiding CNT growth carry over to this two-electrode growth system,[173] no studies have been conducted that can enable the comparison or contrast between gas phase and electrochemical growth processes. Therefore, in this study, we leverage the capability to isolate the catalytic activity to a single electrode, and study electrochemical CNT growth from Fe catalyst layers deposited *via* e-beam evaporation with thickness ranging from 0.5 nm to 5 nm onto stainless steel surfaces. We chose stainless steel as the support for catalysts because of its high conductivity, the low-surface energy surface oxide that allows Fe dewetting, and inert chemical nature in molten carbonates. This approach enables the tuning of catalyst size with the thickness of the deposited Fe, as schematically illustrated in Figure 27a-b.

Figure 27c shows a catalyst-coated stainless steel cathode before electrochemical carbon deposition, with Figure 1d showing a CNT-coated cathode after 60 minutes of electrochemical growth. This duration of growth yields ~ 50 mg of carbon deposited across an electrode with total area 2.5 cm$^2$, achieved under constant current of 100 mA/cm$^2$ (~ 90% Coulombic efficiency). Notably, this yield is higher than conventional CVD growth processes where unlike electrochemical growth, the reaction rate is limited by the decomposition of hydrocarbons at the surface of the catalyst. Importantly, the precise nature of the ultrathin Fe coatings used for catalysts enables our study to focus on understanding of parameters that control and limit growth in this system in accordance with conventional CNT synthesis. Control experiments conducted with no

Fe catalyst demonstrate no CNT growth, making the observed CNT growth observed correlated to the Fe catalyst deposited.

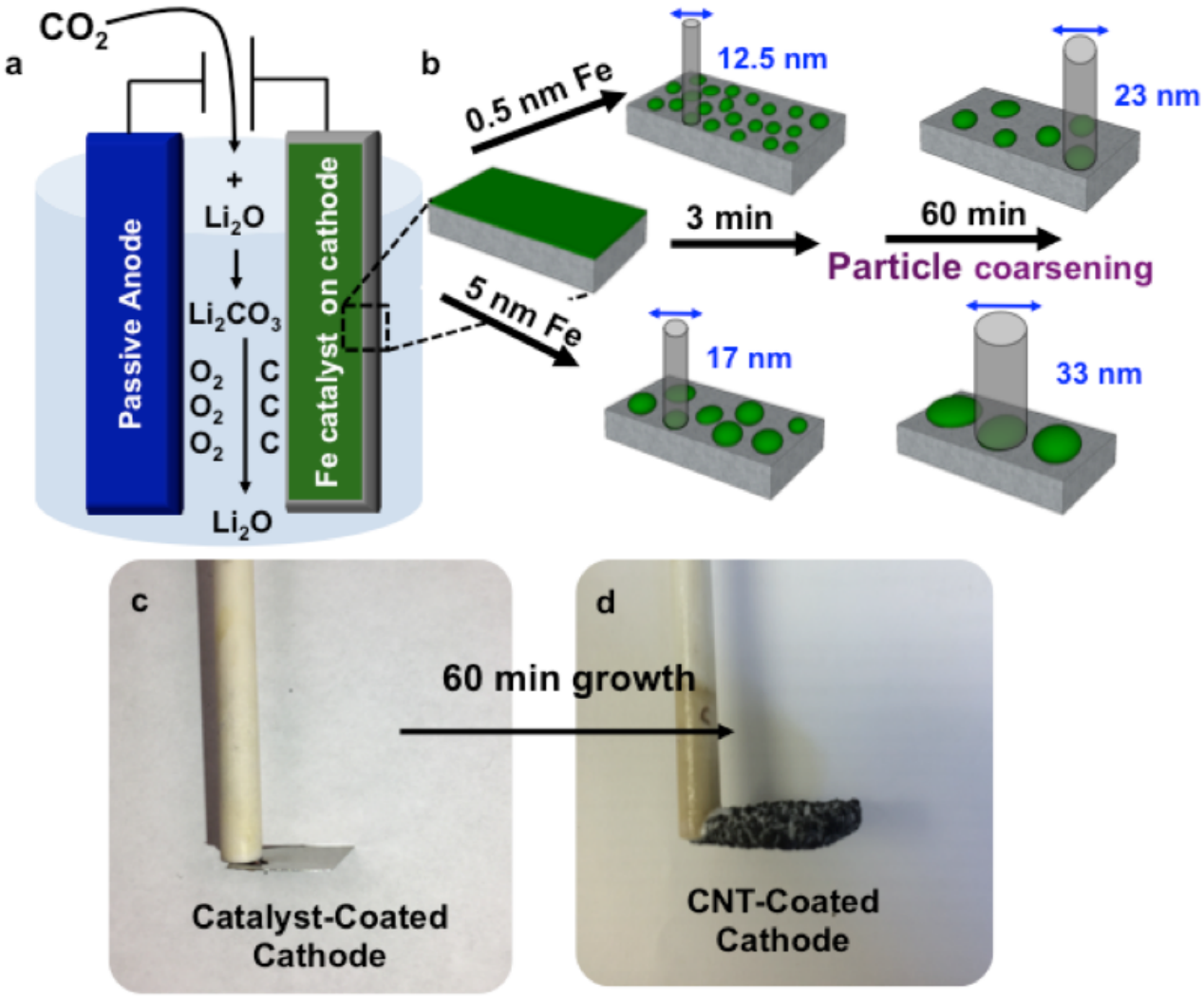


**Figure 27**. Schematic illustration of (a) electrolysis setup and (b) catalyst of varying thickness and growth time controls CNT diameter, (c) catalyst coated stainless steel cathode before electrochemical CNT growth, and (d) with CNT coating after 60 minutes of growth

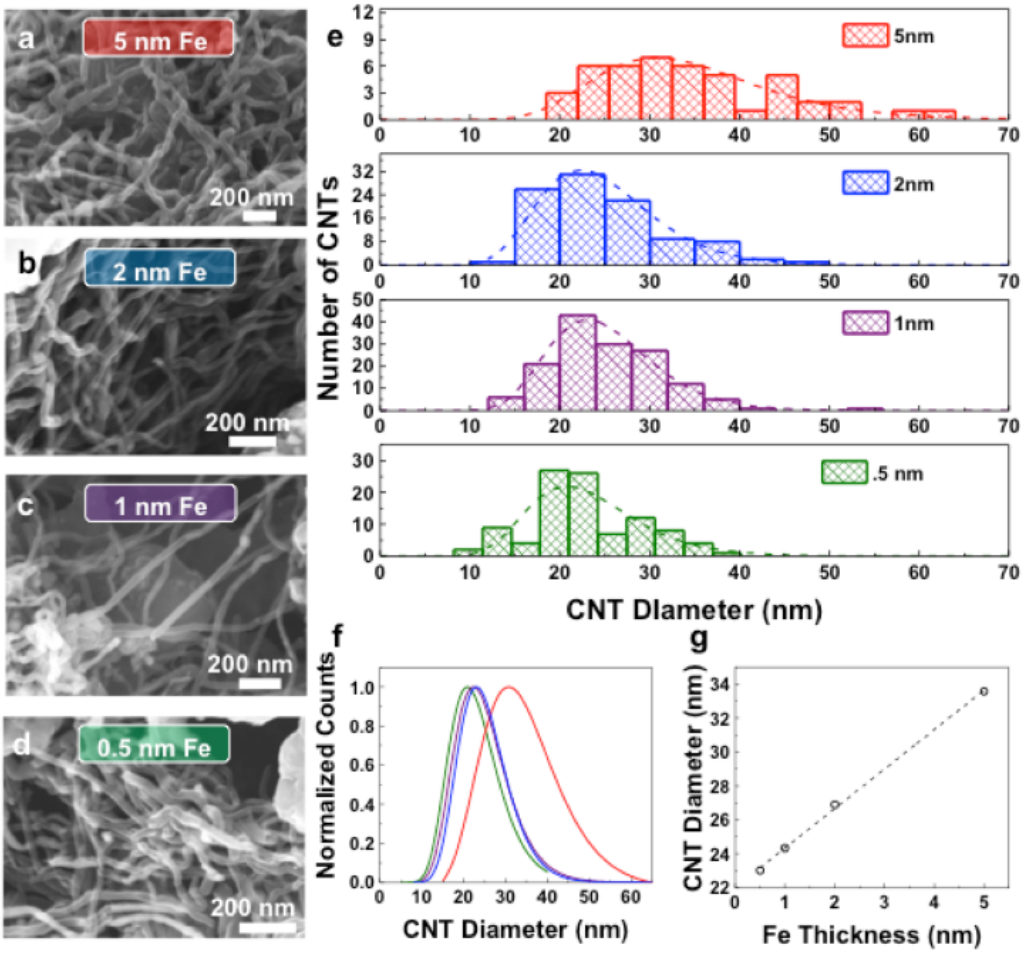


**Figure 28**. (a-d) SEM images showing representative CNTs growth from different catalyst thicknesses, (e) size distributions for each growth condition, (f) normalized lognormal fits of the distributions, and (g) median diameters as a function of Fe catalyst thickness

Electrochemical CNT growth was studied for the different catalyst thicknesses ranging from 0.5 nm to 5 nm Fe, with representative SEM images shown in Figure 28 a-d and corresponding diameter distributions measured from image analysis using multiple SEM images from multiple spots on the sample. The diameter distributions follow lognormal distributions (fits overlaid) with a diameter distribution shifting with the total thickness of Fe catalyst. We observe a general trend of thinner catalyst layers yielding CNTs with smaller and tighter diameter distributions, with 0.5 nm Fe leading to CNTs ranging from ~ 10-38 nm with a median diameter

centered around ~ 23 nm. 5 nm catalyst layers result in the widest and largest diameter distribution ranging from ~ 19-62 nm with a median diameter centered around ~ 33 nm. Normalized lognormal fits of the raw distribution data are overlaid and shown in Figure 29f, demonstrating the trend of increasing CNT diameter from increased Fe thickness, which is further shown in Figure 29g, with median CNT diameter as a function of Fe thickness plotted with a linear fit. Notably, all of the CNTs studied formed mat-like morphologies rather than the dense self-assembled morphology that forms in CVD growth with this catalyst composition. As we expect the percentage of active catalyst is high based on our measured yield, we speculate that hydrodynamic forces at the liquid-solid interface may play a role to modulate the resulting CNT morphology and prevent self-alignment.

Raman spectroscopy was used to characterize the MWCNT products, which all exhibit the characteristic graphitized carbon G peak ~ 1580 $cm^{-1}$, indicative of in-plane $sp^2$ hybridized carbons, and a D mode ~ 1350 $cm^{-1}$, which corresponds to out-of-plane defective $sp^3$ hybridized carbons. Figure 29a shows representative spectra for CNTs grown from all catalyst thickness conditions, and a higher D/G peak intensity ratio is observed for CNTs grown from thicker Fe catalyst layers. This observation indicates a greater concentration of $sp^3$ carbon materials in the samples produced from thicker Fe catalyst layers. Figure 29b demonstrates the trend between the D/G intensity ratios ($I_D/I_G$) as a function of Fe thickness, and we observe a trend where thicker Fe layers yield CNTs with a larger defect concentration, which is generally consistent with the presence of larger diameter CNTs.

As Raman spectroscopy and SEM image analysis give statistical assessments of the CNTs grown, we performed HR-TEM imaging of representative CNTs synthesized from both extreme cases of 0.5 nm (Figure 29c) and 5 nm (Figure 29d) Fe thicknesses to give insight into the

crystallinity and wall quality of the synthesized CNT materials.

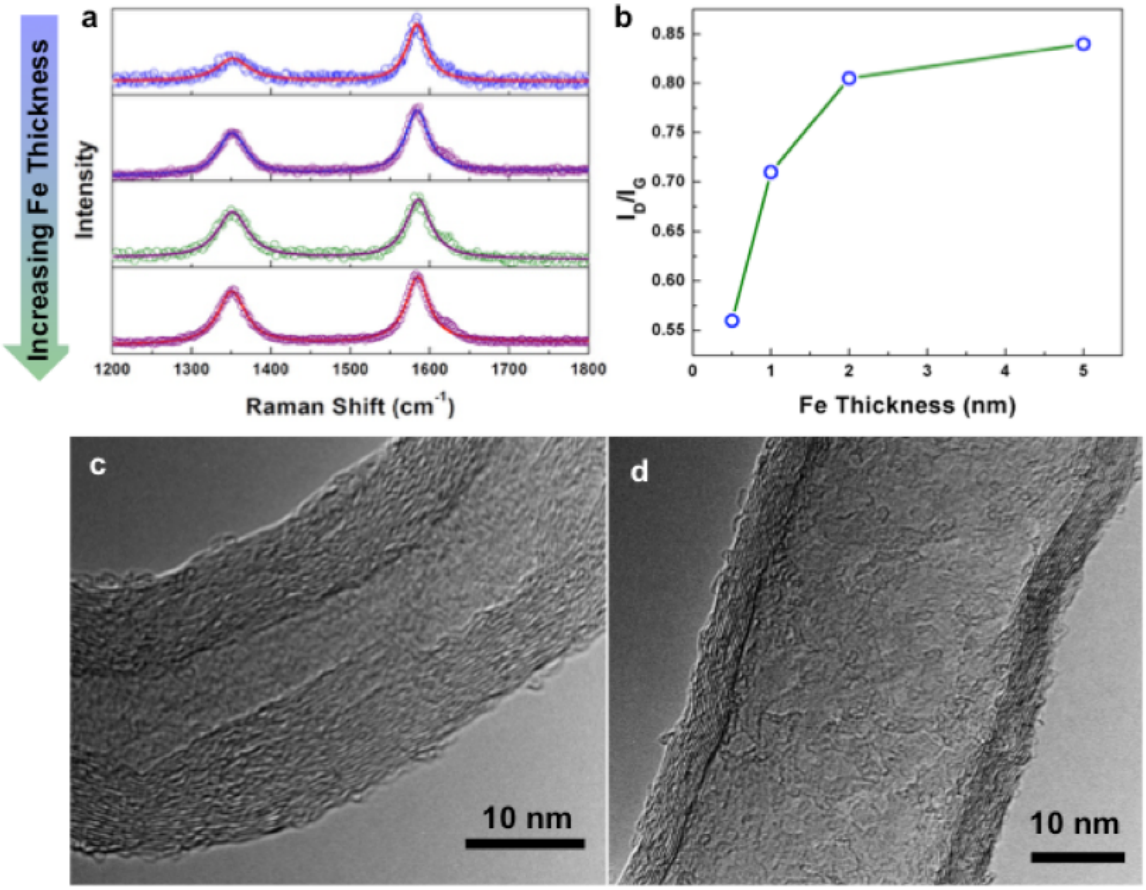


**Figure 29.** (a) Representative Raman spectra with fits shown in solid lines and raw data shown in open circles; (b) ID/IG ratios as a function of Fe catalyst thickness; representative TEM images of CNTs grown from (c) 0.5 nm Fe catalyst and (d) 5 nm Fe catalysts

Consistent with our observations from Raman spectroscopy, we observe a high degree of crystalline carbon compared to other reports on electrochemically synthesized carbon. However, compared to other CNTs produced via CVD using similar catalyst layers, our CNTs exhibit localized crystallinity with a higher defect content than these materials that is common for larger diameter CNT materials. We also observe sizes consistent with diameter distributions taken from SEM images, where smaller diameter CNTs are observed in the case of 0.5 nm Fe films compared to larger diameter CNTs grown from the 5 nm Fe films. However, we notably observe that there

are on average slightly more walls in the smaller diameter CNTs, which is opposite to that expected for CNTs where a constant carbon flux and growth rate is achieved. Since our electrochemical process produces a constant carbon flux per electrode area, we speculate this to be related to the following two points (1) smaller diameter catalyst, owing to their depressed melting point,[222] will support increased carbon diffusion through the catalyst nanoparticle leading to different rates of carbon precipitation,[52] and (2) a CNT growing into a liquid medium will be required to displace the surrounding liquid, causing a drag force during growth that will be independent of the rate at which carbon diffuses to the growing CNT. Collectively, these two points can imply that smaller CNTs may exhibit a greater number of walls, even though the average number of walls between the CNTs grown from 0.5 nm and 5 nm is only different by ~ 2 walls. Our imaging also confirms the absence of amorphous carbon on the CNT wall, which we expect is due to the liquid-solid interface formed by the carbonate with the CNT during growth. This is different from CVD growth where hydrocarbons diffuse through the grown CNT materials before reaching the catalyst, often leading to amorphous carbon build-up on the walls.

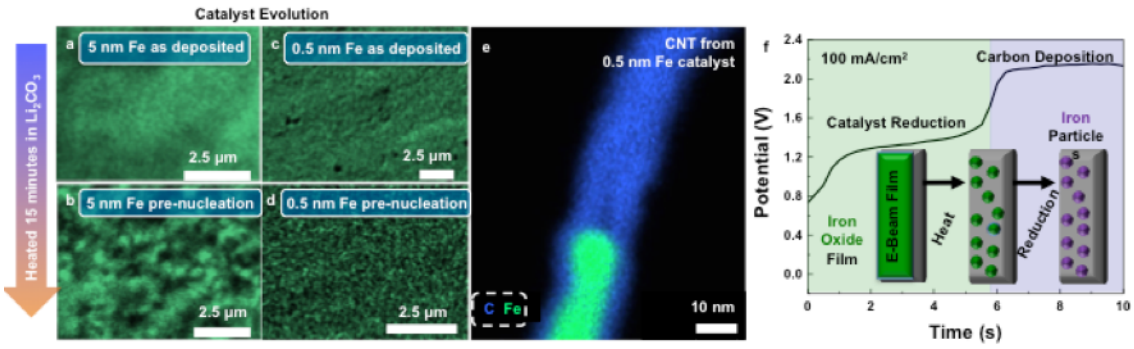


**Figure 30.** SEM elemental maps showing evolution of catalysts (a,c) as deposited and (b,d) after 15 minutes of heating in molten electrolyte; (a,b) show 0.5 nm Fe catalysts and (c,d) show 5 nm Fe catalysts; (e) STEM elemental map of 0.5 nm Fe catalyst grown CNT showing Fe catalyst; (f) galvanostatic electrolysis plot of potential versus time with inlay of schematic illustration of proposed mechanism of catalyst formation and reduction

So far we have demonstrated a strong correlation between the pre-deposited catalyst film thickness and CNT diameter, emphasizing that particle size and CNT diameter are correlated in this electrochemical process. However, with only 0.5 nm thickness of Fe catalyst, the CNTs produced in our system have median diameters of ~ 23 nm, which is much larger than that observed in gas phase growth processes that produce single or two-three walled CNTs from catalysts prepared with this thickness. Since emerging concepts for gas-phase CNT growth have demonstrated the importance of understanding the dynamic nature of the catalyst size, through catalyst reduction to growth and termination,[167, 168] we performed experiments to study the evolution of the cathode surfaces in the environment where CNT growth takes place using SEM elemental mapping. We compared as-deposited Fe thin films on stainless steel surfaces before and after pre-nucleation heat treatment to 750 °C in $Li_2CO_3$ for 15 minutes (Figure 30a-d). As shown in Figure 4a, the 5 nm Fe film appears uniformly distributed on the stainless steel surface until heated in the electrolyte, where the film forms larger particles, shown in Figure 30b. However, the 0.5 nm Fe film shows the formation of smaller well-distributed particles (Figure 30c-d). Whereas this imaging isolates the catalyst formation prior to CNT nucleation and growth, we further performed post-mortem STEM EDS imaging on the CNTs to correlate the final products and the chemical identity of the catalyst particles that remain embedded inside the CNT tips to confirm our prior observations. We know that only those elements that participate catalytically in CNT growth will be embedded in the CNTs following growth, and this serves to confirm the inert nature of our passivated anode. The compiled STEM EDS map is shown in Figure 30e, where we observe Fe as the only element that remains embedded inside a CNT tip grown from 0.5 nm Fe catalyst layer. Figure 30f reports the first 10 seconds of a typical potential response from the galvanostatic electrolysis conditions applied to these Fe-based catalyst layers. We observe two

distinct plateaus, including the first at around 1.2 V for 6 seconds, then a higher potential plateau at around 2.0 V, which extends for the duration of the hour-long electrolysis. We attribute the low-voltage initial plateau to the reduction of the Fe catalyst, which oxidizes during air exposure following deposition. As it is known that metallic Fe is necessary to precipitate CNTs,[223] we emphasize this as a key step to achieve CNT growth prior to the carbon deposition from $Li_2CO_3$, which occurs near 2 V. This proposed mechanism is schematically represented as an inset in Figure 4f.

To better understand the effect of dynamic processes occurring between the first few seconds where catalyst reduction occurs, and the conclusion of a 60 minute duration synthesis experiment, we performed time-stop experiments for the cases of 0.5 and 5 nm Fe thicknesses for 3, 10, and 30 min growth times and compared the CNTs produced under these conditions to those grown for 1 hour. The CNT diameter distributions and overlaid lognormal fits as well as representative SEM images of each time growth and thickness are shown in Figure 31. We observe at both thicknesses that smaller diameter CNTs with a tighter size distribution are correlated to shorter growth times, with sizes ranging from ~ 8-22 nm for 0.5 nm Fe (Figure 31a) and ~3-37 nm for 5 nm Fe (Figure 31f) for 3 min growth conditions. These diameter distributions become wider with median sizes increasing under conditions of longer growth times. Representative Raman spectra for each growth condition demonstrates the characteristic peaks for graphitized carbon.

The median sizes for each condition are plotted in Figure 31i as a function of growth time for both thicknesses studied with linear fits overlaid. In each case we see a positive correlation between growth time and median CNT diameter, with larger diameters observed at each growth time for the 5 nm Fe grown CNTs compared to those grown from 0.5 nm Fe.

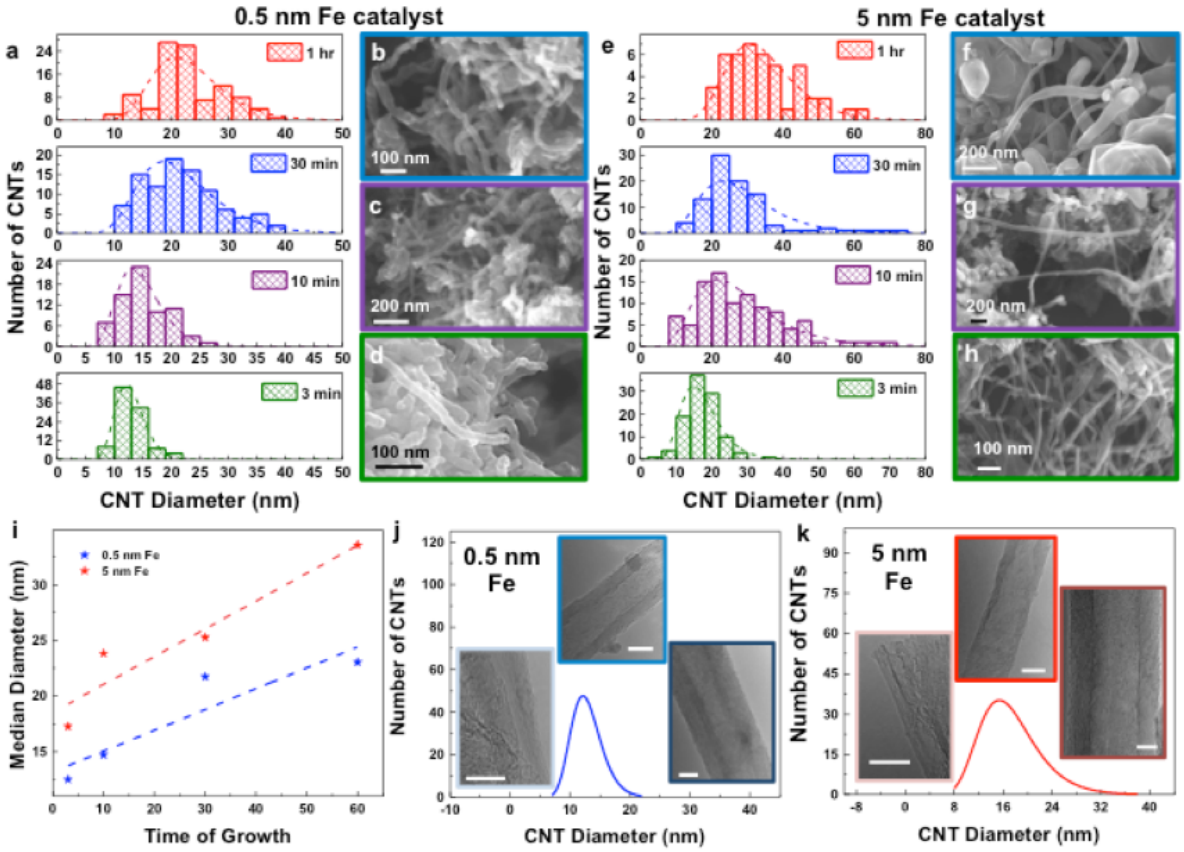


**Figure 31.** (a) size distributions of CNTs grown from 0.5 nm Fe for varying growth times, (b-d) representative SEM images for 0.5 nm Fe grown CNTs at each growth time, (e) size distributions for CNTs of the same growth times from a 5 nm Fe film, (f-h) representative SEM images for 5 nm Fe grown CNTs at each growth time, (i) median CNT diameter as a function of growth time for 0.5 nm and 5 nm Fe grown CNTs, and lognormal fits with representative TEM images for (j) 0.5 nm Fe grown CNTs and (k) 5 nm Fe grown CNTs (SB = 10 nm).

In order to study the crystallinity and number of walls for the CNTs, we performed HR-TEM imaging for CNTs grown for 3 min and show representative TEM images across the spectrum of measured diameters as insets alongside the lognormal fits for 0.5 nm Fe (Figure 31j) and 5 nm Fe (Figure 31k) thicknesses. Notably, while the TEM imaging is generally consistent with the trends observed with SEM imaging, this technique is ideally suited to carry out assessment of the averages and the extremes. For example, TEM imaging reveals some small CNTs such as the double-walled CNT grown from 5 nm Fe catalyst for 3 min which is shown as an inset in Figure 31k - representing

the smallest diameter CNT ever grown from $CO_2$. Whereas these small diameter CNTs are a minority component of the CNTs grown, their presence indicates that the nucleation of such small diameter CNTs can exist in this electrochemical approach, and we speculate that such species are rapidly overshadowed by the CNTs that nucleate and grow as the Fe catalyst undergoes catalyst coarsening.

Reflecting on the results of our studies in comparison to CVD techniques using similar catalyst materials, we attribute the larger diameter of CNTs we observe during electrochemical growth to Ostwald ripening-induced catalyst morphology evolution prior to CNT nucleation. This observation provides us with exceptional insight into how SWCNT growth can be achieved based on lessons learned over the past few decades in CVD growth. Whereas high yield SWCNT growth is now readily achieved in CVD techniques, the enabling factor to achieve this was the incorporation of oxygen-containing additives into the gas mixture, including water vapor, ethanol, or oxygen.[44, 46] However, research studies later demonstrated the role of these additives to slow Ostwald ripening of catalyst particles, which was the mechanistic advance to achieving high density growth of SWCNTs.[224, 225] For electrochemical growth, this generates an intriguing question about the type of additives which can be introduced in a molten carbonate that could draw parallels to this important step in CVD. Additionally, another key feature to achieving controlled SWCNT growth has been linked to the fast reduction of the catalyst layer to produce the smallest possible catalyst particles. Whereas this is difficult to carry out in CVD without using highly reactive and toxic gas additives, such as hydrazine,[226] the electrochemical growth of CNTs offers new *electrochemical parameters* that can be controlled to achieve this, noting that the catalyst reduction itself is an electrochemical process. Therefore, by understanding this Ostwald ripening mechanism by which the CNTs produced in our electrochemical method have larger diameters

than CNTs grown through CVD, we can envision a path drawing on parallels and lessons learned from three decades of advances in gas phase CNT growth to achieve SWCNT growth using electrochemistry in the future.

Finally, it is noteworthy to discuss overall process energy and byproduct considerations for the electrochemical growth of CNTs from atmospheric carbon dioxide as compared to conventional synthesis routes. Conventional routes have been studied widely, but are limited to the thermal, instead of electrochemical, decomposition of carbon-containing precursors (hydrocarbons).[227, 228] This requires a large energy footprint, and is inefficient since energy is distributed into a cracking pattern from the hydrocarbon precursor to produce numerous carbon-containing byproducts, including methane, volatile organic compounds, and polycyclic aromatic hydrocarbons – most of which are not consumed in the reaction.[229-232] Since catalytic activity in the conventional approach is associated with only a few active (minority) hydrocarbon species, the majority of these secondary products are process emissions, raising significant environmental and public health concerns when scaling-up CNT manufacturing technologies.[229] In contrast, the electrochemical synthesis of CNTs from $CO_2$ involves solid carbon deposits onto an electrode and only $O_2$ emission byproducts, which are beneficial to the environment. Whereas most arguments over carbon neutrality commonly hinge on the emissions footprint of the *electricity source* instead of the technique itself, we instead emphasize that a feasible process which converts $CO_2$ to some material must produce a material value higher than the electricity cost input. In this regard, an all-carbon product produced with energy and $CO_2$ will have a net value per $CO_2$ greater than that of the net $CO_2$ consumed, making it carbon neutral or negative regardless of the source of energy input. Here, calculations for our laboratory-scale process involves energy input cost of ~ $\$50/kg_{CNT}$ which is 2X lower than the minimum cost of CNTs on the market that are generally

tens of nm in diameter (20 – 50 nm for example) and with low wall crystallinity. By simple system level designs, such as the use of $ZrO_2$ instead of $Al_2O_3$ thermal insulation materials, these costs can be lowered to below $\$5/kg_{CNT}$. In parallel, better control of underlying mechanisms in this system can enable the extremely valuable forms of CNTs such as single and double-walled CNTs. With a wave of research today centered on multi-step $CO_2$ conversion processes bottlenecked by low efficiencies due to energy coupled into a spread of chemical products, none of which are more valuable than the nominal cost of energy to produce them, our work demonstrates an alternate path to the quality and diameter of CNT materials that can overcome this limitation. Given the extraordinary properties, we anticipate this route to be the basis to produce all carbon nanostructures that can enable the batteries, composites, transparent films, fabrics, and coatings of tomorrow based on tapping into this abundant source of this $CO_2$ feedstock in our air today.

## 6.4 Conclusions

In summary, we demonstrate that the electrochemical growth of CNTs from $CO_2$ can be achieved from Fe catalyst, with diameters controlled by the catalyst particle distribution and coarsening during the duration of growth. Our results demonstrate the ability to tune median CNT diameters from ~ 33 nm to ~ 23 nm by varying the catalyst thickness from 5 nm to 0.5 nm Fe. Raman spectroscopy and TEM characterization reveal a high level of crystallinity and lower concentration of defects for CNTs grown from thinner catalyst layers. SEM EDS measurements confirm the formation of catalyst particles on the surface of the stainless steel cathodes during pre-growth thermal treatment that are responsible for MWCNT nucleation and growth, confirmed through post-mortem STEM EDS imaging. Galvanostatic electrolysis indicates the electrochemical reduction of Fe catalyst particles, followed by carbon deposition to produce CNTs.

Experiments studying the time evolution of CNT diameters highlight the rapid increase of the CNT diameters over growth duration, indicating strong coarsening or Ostwald ripening effects during growth. HR-TEM imaging reveals a high degree of crystallinity for the CNTs grown under short time conditions, and a minority population of extremely small diameter CNTs. Energy calculations for our process further paints a picture that distinguishes our efforts from other $CO_2$ conversion processes where the economic value of the CNT output is much greater than the energy consumption of the process. This is a picture unique to CNTs with small diameters ranging from multi-walled CNTs to single-walled CNTs with diameters less than 20-30 nm and cannot be matched by routes to convert $CO_2$ into methanol, cements, carbon fibers, or large diameter CNTs (> 100 nm) due to the low value of these materials in current markets. This work presents fundamental insight into the challenge of coarsening-induced diameter control to transition to single-walled CNT growth, giving promise to a powerful technique to convert a gas-phase environmental hazard into some of the most technologically valuable materials in the world.

# Chapter 7

## Toward Sustainable Manufacturing of Lithium-Ion Batteries: Utilization of Carbon-Negative Carbon Nanotubes and Earth-Abundant Lithium Iron Phosphate for Low-Carbon Batteries

Adapted from: **A. Douglas**, K. Moyer, J. Eaves, M. Pannell, C. L. Pint, "Toward Sustainable Manufacturing of Lithium-Ion Batteries: Utilization of Carbon-Negative Carbon Nanotubes and Earth-Abundant Lithium Iron Phosphate for Low-Carbon Batteries," *in preparation*

### 7.1 Introduction

Reducing greenhouse gas (GHG) emissions from the transportation sector is a major thrust in many climate change policies to reduce overall anthropogenic carbon emissions, as the transportation sector generates the largest share of GHG emissions at ~ 28% of all emissions in the United States.[1, 233-235] Increased population and mobility have outweighed modest fuel efficiency improvements made to vehicles, causing most efforts to focus on the transition to a transportation industry powered by electricity.[236, 237] Due to their high energy and power density, lithium ion batteries (LIB) are an ideal choice to aid in this transition and are being increasingly deployed in electric vehicles (EVs) primarily due to steadily decreasing battery cost and increasing affordability of EVs (including all-electric, plug-in hybrid, and hybrid-electric vehicles).[238] Replacing conventional gasoline-powered combustion engine motor vehicles with EVs has the promise to significantly reduce GHG emissions in the use-phase of a vehicle's life, and shift GHG emissions and other pollutants from distributed vehicle tailpipes to largely centralized power plants.

However, the rise in LIB deployment has garnered critical assessment of the energetics and GHG emissions associated with LIB production and use in EVs.[12, 15, 239, 240] Most studies to date have focused their efforts on assessing various energy blends to minimize the use-phase carbon footprint of EVs, even though the production-phase of LIBs is energy-intensive with a high level of GHG emissions from chemical processes. According to cradle-to-gate life cycle analysis studies,[12, 241-243] more than 400 kWh are required to make a 1 kWh LIB, resulting in the emission of about 75 kg of $CO_2$ – and a single EV typically uses ~ 28 kWh of storage.[12] The vast majority (~ 74%) of this energy required for LIB production comes from materials production, with the remaining energy in the manufacturing and assembly stage.[15] This realization begs the question – can we change the selection criteria for materials used in LIBs to minimize GHG emissions and thus create a truly "green" technology to power transportation with environmental benefits realized prior to hundreds of cycles?

Classical figures of merit used to select materials for LIBs include specific energy and power, lifetime, cost, and safety. These criteria have informed our current technology, which relies on intercalation-based electrodes consisting of layered metal oxide cathodes and graphite anodes.[131, 244] However, beyond the energetically-intensive production process for these materials, recent attention has been drawn to the questionable labor practices used in Cobalt mining,[245] airborne particulate matter from graphite mining causing public health concerns and thwarting crop growth in areas nearby mines,[11, 246] and possible geo-political issues and price instability arising from foreseen shortages of low-abundance materials used such as Cobalt, Lithium, and Nickel (increased battery demand has resulted in a nearly 4X increase in prices for whole-sale Cobalt in the past two years, from \$22 to \$81/kg).[11, 12, 130] Thus, any new assessment of material choices used for LIBs should include careful consideration of production energy and GHG

emissions; abundance in earth's crust; geo-political, human rights, and public health concerns; *and* performance metrics such as energy, power, lifetime, safety, and cost. Until now, materials selection for LIBs have been made solely based on cost and performance at the expensive of sustainability, but given the rising demand of batteries for EVs, the scarcity of materials currently employed in LIBs, and the urgency of climate change requiring a drastic reduction in GHG emissions,[2] selection criteria must change.

In this spirit, the aim of this study is to develop a platform for LIB materials selection which accounts for sustainability and performance. Using well agreed-upon data from Argonne National Laboratory's GREET model,[15] we create a sustainability index for currently-employed and next-generation LIB materials that includes abundance, energy and GHG emissions from production, geo-political, human rights, and public health concerns, and performance metrics including capacity and voltage. Based on the findings from this platform, we utilize earth-abundant iron-based cathode materials[247] and carbon nanotubes (CNTs) derived from carbon dioxide[189, 219, 248] as anode materials in batteries, firstly studying their individual performance in half-cells and finally combining them into full-cells with stable cycling performance. Overall, our work provides a blueprint towards the sustainable selection of materials for LIBs to power our society towards a net-zero GHG emissions transportation model, and highlights the ability to significantly reduce the overall $CO_2$ footprint of LIBs without compromising performance by employing earth-abundant cathode materials produced with minimal emissions, with CNTs synthesized using atmospheric carbon.

## 7.2 Experimental Details

### *7.2.1 CNT Synthesis*

CNTs were synthesized using previously described methods[189, 219, 248] employing electrochemical growth mediated by molten carbonate electrolysis of $CO_2$. Briefly, Ni wires were coated with 500 cycles (~50 nm) of $Al_2O_3$ by a Gemstar Arradiance atomic layer deposition (ALD) and used as anodes. The thickness of this coating was determined through ellipsometry analysis of $Al_2O_3$ coatings on silicon wafers with a J.A. Woollam spectrometer. To accomplish this, we utilized sequential 28 ms pulses of $C_6H_{18}Al_2$ and $H_2O$ with a residence time of 1 s. Untreated galvanized steel (Home Depot) wire was used as the cathode. Experiments were carried out in an alumina crucible (AdValue Tech, 50 ml) containing 40 g lithium carbonate (Fisher Scientific, 99%) electrolyte, which was held at 750 °C (mp 723 °C) in a cylindrical ceramic heater (Thermcraft) using a bench top temperature controller (OEM Heaters). 5 $cm^2$ electrodes (coiled wires) were immersed into the electrolyte and a constant current was applied across the electrodes. All electrolysis experiments in this study were carried out for 1 h under a current density of 100 $mAh/cm^2$. We observe no degradation of the lithium carbonate electrolyte and reused the same batch for five consecutive experiments before discarding. During the electrolysis, carbon accumulates at the cathode, which is removed from electrolyte and cooled after electrolysis. Carbon product was removed from the electrodes by bath sonication in water (1 h), and purified from carbonates *via* washing in 2 M HCl, and solvent exchanged to water through centrifugation. The carbon was dried at 60 °C overnight.

*7.2.2 Battery Fabrication*

Coin cell devices were assembled in an Ar glovebox using 2032 stainless steel coin cells (MTI). For cathodes, Lithium Iron Phosphate (XX) was dispersed in a slurry of electrochemically-grown CNTs and PVDF binder at a ratio of 18:1:1, respectively. The slurry was cast onto carbon-coated aluminum foil using a doctor blade and dried in a vacuum oven overnight. Individual electrodes were punched out from the foil and assembled into coin cells with a 2500 Celgard separator saturated with 1 M LiPF6 (dried at 100 C overnight in an Ar glovebox) in diethylene glycol dimethyl ether (Sigma-Aldrich) separating the cathode material from pure lithium foil (Sigma-Aldrich). The same procedure is followed for half-cell anodes, except the slurry is a mixture of electrochemically-grown CNTs and PVDF binder with conductive carbon black at a ratio of 8:1:1, and was cast onto copper foil. Galvanostatic charge-discharge measurements were carried out for constant currents ranging from C/10 to 2C (1 $C_{LFP}$ = 170 mA/g, 1 $C_{CNT}$ = 374 mA/g). Full cells were assembled by first cycling CNT anodes for 2 full cycles and charged to 1 V at C/10 in half-cells against lithium foil prior to disassembly. These were then assembled into full cells with LFP cathodes, with a negative to positive ratio of 1.2 in terms of capacity.

## 7.3 Results and Discussion

With the onset of EVs becoming more affordable and accessible since the early 2000's, battery production for EV applications has grown exponentially to meet the rising demand for more total vehicles, and farther range per EV (Figure 32a). Battery capacity (in GWh) has more than quadrupled from 2015-2017[249] and is only expected to continue rising as the cost of batteries continues to decrease towards the 2020 DOE target of $125/kWh,[10] the figure of merit to make

EVs price-competitive with conventional gasoline vehicles. However, the core chemistry of our LIBs hasn't changed since its inception, and improvements to cost, energy, and power density have been realized solely through packaged-cell-level engineering.

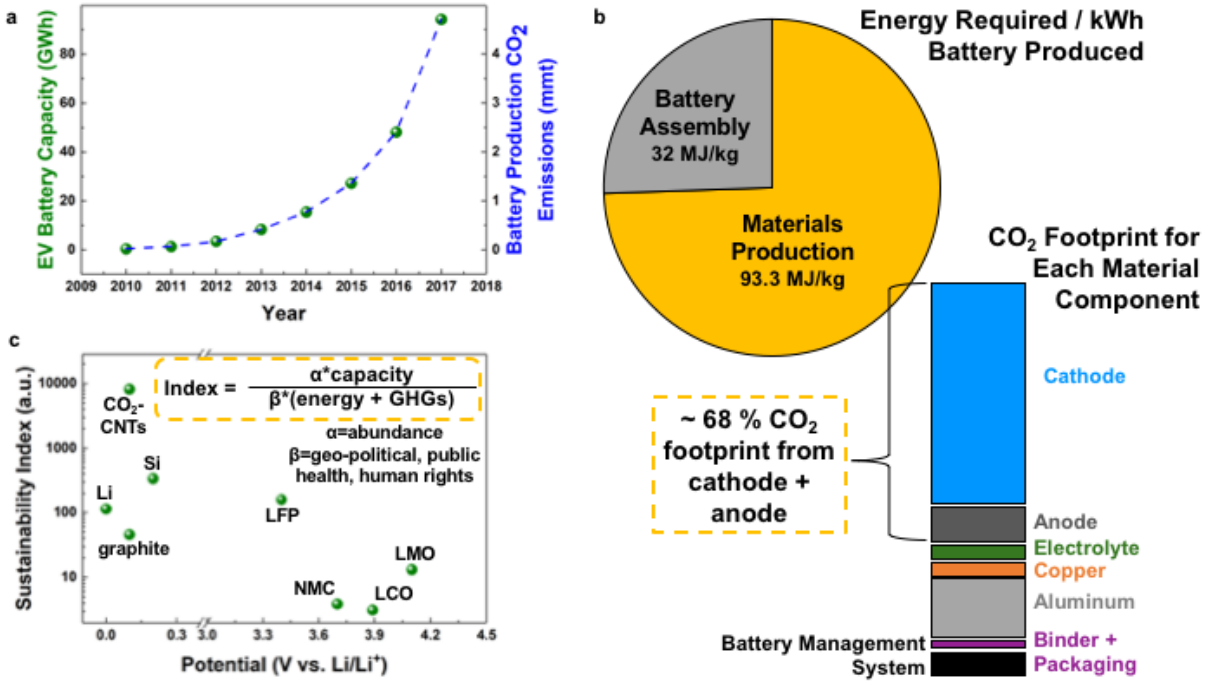


**Figure 32.** (a) increasing EV battery capacity with subsequent increasing CO2 emissions from EV battery production, (b) energy and CO2 assessment of LIB cell components, and (c) sustainability of many current and future LIB anode and cathode materials, plotted as a sustainability index versus potential

Given that largest contributor to the energy required for battery production comes from the materials production (Figure 32b), and the materials utilized have not changed over the last 10 years,[11] the $CO_2$ footprint / kWh has remained largely unchanged, causing the same exponentially rising trend in overall $CO_2$ emissions from EV battery production (Figure 32a). Today, the total $CO_2$ emissions from EV battery production accounts for < 1% of total transportation-related $CO_2$

emissions in the United States. However, if growth continues as projected, by 2030 there will be ~ 220 million EVs on the road globally,[249] with the equivalent battery production-related emissions at ~ 15% of today's transportation-related $CO_2$ emissions. Considering these emissions happen prior to the use-phase of a vehicle, and the penetration of renewables onto the grid is only projected to grow from 18% to 26% in the same timeframe,[250] the GHG emissions avoided by switching to EVs are minimal at best when considering both the battery manufacturing and use-phase in a life cycle analysis without significant changes to the GHG footprint during battery production.

A careful assessment of the $CO_2$ footprint for each material component that makes up an LIB reveals that ~ 68% of total $CO_2$ emissions associated with LIBs are derived from the cathode and anode materials, with the majority of this figure coming from the cathode (Figure 32b).[15] In this spirit, we assessed a variety of anode and cathode materials based on the energy and GHG emissions associated with the raw materials production, earth abundance, theoretical capacity and voltage, and any geo-political, public health, and human rights concerns. These factors were all used to determine a sustainability index, where:

$$\text{Sustainability Index} = [\alpha * \text{theoretical capacity}] / [\beta * (\text{energy} + \text{GHG emissions})] \quad (1)$$

In this equation, $\alpha$ is the earth abundance of the element (in multi-elemental compounds, the lowest abundance is considered), and $\beta$ is a variable 1-5 to account for geo-political, public health, and human rights concerns. Additionally, the energy required for production and GHG emissions associated with the chemical production and processing of the materials are derived from well-agreed upon data from Argonne National Laboratory's GREET model.[15] The sustainability index for a variety of commercially utilized and next-generation anode and cathode materials is plotted versus theoretical potential (V vs. $Li/Li^+$) in Figure 32c. Notably, currently-utilized lithium cobalt oxide cathodes (LCO) and graphite anodes are among the least sustainable materials studied due

to questionable labor practices used in the mining of cobalt, airborne particulate matter from graphite mining that results in damaged crops and polluted villages and drinking water, and the low earth-abundance of cobalt at only 0.0003% in the earth's crust. In contrast, despite its 0.5 V handicap compared to LCO, lithium iron phosphate (LFP) stands out as the most sustainable cathode material due to iron's extremely high earth abundance at 6.3% in the earth's crust and > 5X lower energy required to produce LFP compared to LCO, both under hydrothermal synthesis techniques.[15] Additionally, when considering anode materials, $CO_2$-derived CNTs have the highest sustainability index due to the relatively low energy required to produce them (2X lower than graphite production), but primarily because of their negative GHG emissions footprint when coupled with manufacturing using renewable electricity sources.[219]

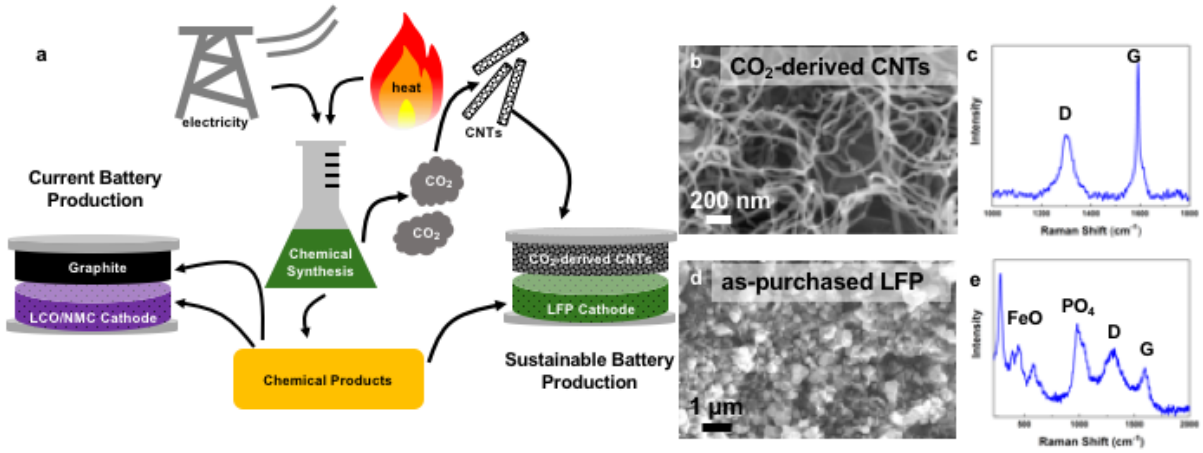


**Figure 33.** a) schematic illustration of CO2 emitting chemical processes used to make battery materials today, which can be coupled into CO2-derived materials for LIBs, (b) SEM images and (c) Raman spectra of CO2-derived CNTs, (d) SEM and (e) Raman spectra of as-purchased LFP

In this spirit, we envision a pathway towards net-zero GHG emissions battery production with the use of low-energy and earth abundant cathode materials coupled with $CO_2$-derived carbon anode materials. This is schematically represented in Figure 33a. Under current manufacturing, emissions are associated with both the anode and cathode materials, but we present a platform

towards negative-emissions anodes derived from $CO_2$ which offsets GHG emissions from cathode processing. To achieve the highest $CO_2$ emissions reduction over current LIB technology, we employ LFP cathode materials with $CO_2$-derived CNTs, and characterization of materials are shown in Figure 33. The synthesis of $CO_2$-derived CNTs using electrochemical routes has been previously described[189, 219, 248] and relies on the electrochemical splitting of carbonate melts and chemical capture of ambient $CO_2$ via metal oxides that remain in the electrolyte after deposition of C and $O_2$. This process results in an *in-situ* capture and conversion technique for atmospheric $CO_2$ that has no toxic by-products, demonstrates high energy efficiencies (Coulombic efficiencies > 90%), and produces a highly valuable material that can be implemented into a variety of devices to increase performance. The synthesis technique was chosen using galvanized steel cathodes and $Al_2O_3$ coated Ni anodes to produce CNTs that exhibit a balance of small diameter, highly graphitic multi-walled CNTs with a low catalyst content ( < 10 wt.%). SEM images of electrochemically produced CNTs from $CO_2$ are shown in Figure 33a, which show multi-walled CNTs with diameters ~ 15-50 nm with a median diameter ~ 27 nm. Raman spectroscopy was used to characterize the CNT products, which exhibit the characteristic graphitized carbon G peak ~ 1580 $cm^{-1}$, indicative of in-plane $sp^2$ hybridized carbons, and a D mode ~ 1350 $cm^{-1}$, which corresponds to out of plane defective $sp^3$ hybridized carbons. SEM characterization of as-purchased LFP particles is shown in Figure 33d, with Raman spectra consistent with LFP signature in Figure 33e.

The materials selected were assembled into half-cells and tested against lithium foil for electrochemical performance. Typical charge-discharge curves and cycling data at C/3 for LFP cathodes employing CNT conductive additives and PVDF binders is given in Figure 34, and demonstrates a capacity retention of 61% after 100 cycles, with stable Coulombic efficiencies reaching ~ 99.5% after 10 cycles. Rate studies at moderate C rates up to 1C were performed and

demonstrate a linear capacity retention with minimal active material degradation as shown by the high capacity retention when cycled at C/3 after more moderate rates of cycling (Figure 34). Additionally, minimal overpotential is observed at rates up to 1C. Half-cell cycling of CNT anodes against lithium foil show a sloping curve with lithium intercalation ranging from ~ 1V - 0.1V as revealed by charge-discharge curves (Figure 34) and demonstrate cycling performance with Coulombic efficiencies reaching 98.8% after 8 cycles. Notably, first cycle SEI formation for high surface area nanomaterials is often quite significant, with CNT anodes in literature demonstrating a wide range of performances resulting from their varying morphologies and structures. However, the CNTs used here demonstrate minimal first-cycle losses, with first-cycle capacities ~ 550 mAh/g, corresponding to a first cycle Coulombic efficiency of 73%. Rate studies at moderate rates up to 1C also demonstrate high capacity retention with minimal overpotential, with retention of 71% at 1C.

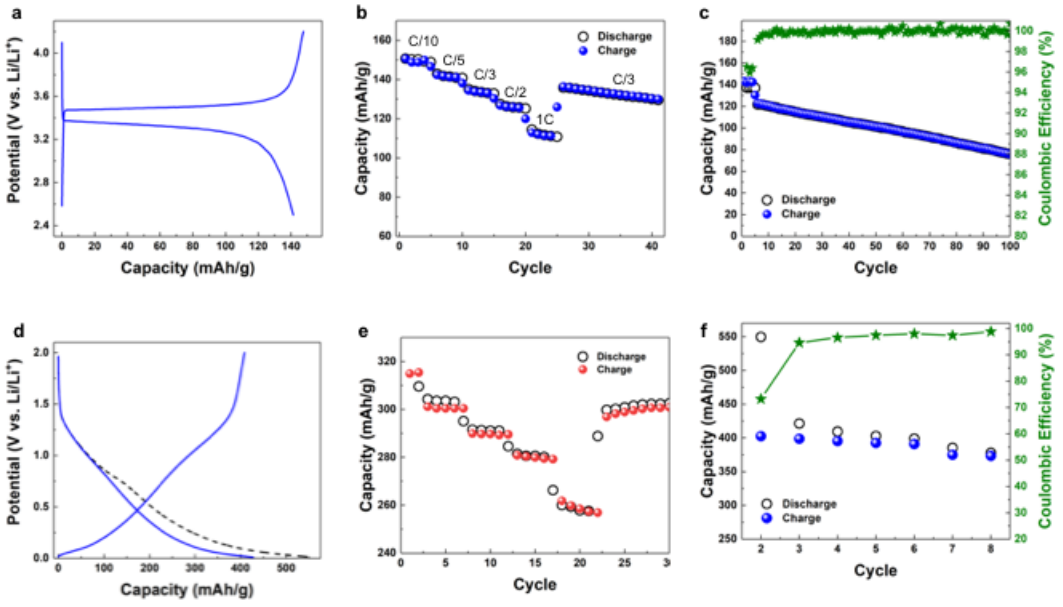


**Figure 34.** (a-c) half-cell data for LFP cathodes against lithium foil, and (d-f) half cell data for CNT anodes against lithium foil

To assemble full-cells employing LFP cathodes and CNT anodes, CNT anode half-cells were cycled twice at C/10 and charged up to 1V prior to disassembly and combination with uncycled LFP cathodes with 1M $LiPF_6$ in EC/DEC electrolyte. The cells had a 20% excess of anode material in terms of capacity, to account for first-cycle irreversible losses and to avoid lithium plating at the anode. Further, the pre-cycling of the anodes allowed for SEI formation over the anode surface without irreversible losses of lithium at the cathode side. Full-cell performance is shown in Figure 35, with charge-discharge curves at C/10 shown in Figure 35b and cycling at C/3 in Figure 35c. The lower voltage plateau and sloped plateau compared to half-cell cathodes reflect the combination of electrochemical processes at both the positive and negative sides of the cell. The LFP/CNT cells demonstrate a reversible capacity of ~ 110 mAh/g. Cycling data demonstrates capacity retention of 84% over 35 cycles, and a Coulombic efficiency reaching 98.5% after ~ 15 cycles.

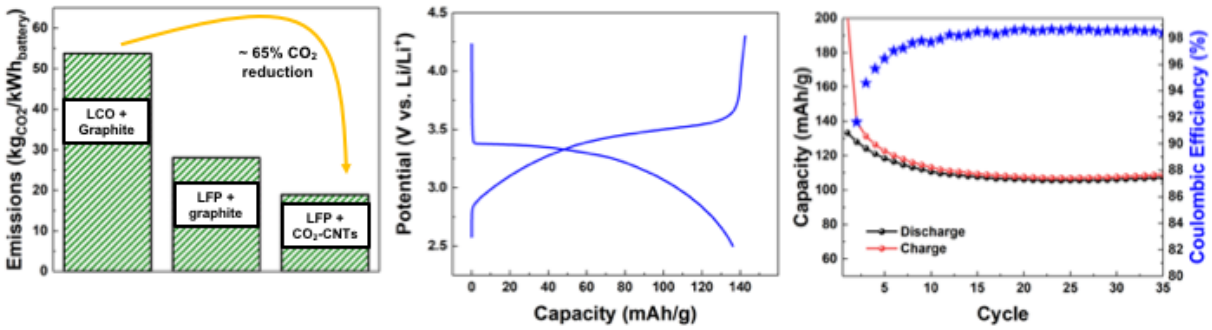


**Figure 35.** (a) emissions per kWh of various battery architectures, (b) charge discharge and (c) cycling data for full cells employing CNT anodes and LFP cathodes

Importantly, the $CO_2$ emissions associated with the production of this cell architecture demonstrates a 65% reduction compared to LCO/graphite cells, when accounting for the lower

emissions from LFP processing and the negative emissions of the $CO_2$-derived CNTs (Figure 35a). Notably, the switch from LCO to LFP cathode material accounts for ~ 48% of this reduction, with the remaining $CO_2$ emissions avoided derived from carbon-negative materials used at the anode. Considering this demonstrates a 17% $CO_2$ emissions reduction for replacing a component that typically constitutes < 10 % of overall $CO_2$ emissions, this platform demonstrates the impact of utilizing carbon-negative materials throughout a battery architecture, and presents a pathway forward towards low-carbon electrochemical energy storage.

Considering all LIB materials components that contribute towards GHG emissions, other components of interest for replacement with low-carbon alternatives include the aluminum current collector used at the cathode (which accounts for nearly 18% of total GHG emissions for LIB materials), the battery management system, and the copper current collector used at the anode (each responsible for ~ 3.5% of emissions). Alternative current collectors made of carbon-based materials would achieve light-weighting of these components and if coupled with carbon-negative production from electrochemical capture of ambient $CO_2$ could be combined to realize a LIB with near net-zero emissions from materials processing (97% GHG emissions reduction from materials components).

## 7.4 Conclusions

In summary, we present here a platform for assessing the sustainability of materials selected for LIB applications and discuss routes towards LIB manufacturing with net-zero GHG emissions. This is especially pertinent now as we are at the cusp of a global widespread transition towards an electrified transportation technologies, but cradle-to-gate life cycle analyses thus far have shown the manufacturing of materials for LIBs to be problematic when considering the

overall benefit EVs bring to total transportation-related GHG emissions. In this work, we demonstrate the use of electrochemically synthesized $CO_2$-derived CNTs as anode materials coupled with earth-abundant LFP cathodes for a low-carbon footprint battery architecture. CNT materials were characterized by SEM and found to have a balance of small diameter ~ 27 nm and highly graphitic structure, demonstrated with Raman spectroscopy. Electrochemical characterization of CNT anode and LFP cathode half-cells demonstrate cycling performance, with CNT anodes demonstrating a capacity ~ 315 mAh/g at C/10 and LFP cathodes demonstrating a capacity ~ 137 mAh/g at C/10 with a 62% retention after 100 cycles at a moderate cycling rate of C/3. Full-cells assembled using CNT anodes coupled with LFP cathodes tested at C/10 delivered a reversible capacity ~ 110 mAh/$g_{LFP}$, and Coulombic efficiency reaching 98.5% by cycle 15. The use of earth-abundant LFP materials that require low energies to produce using conventional techniques coupled with CNT anode materials derived from atmospheric $CO_2$ demonstrate a $CO_2$ emissions reduction from materials components of 65% compared to LCO/graphite cells, which constitutes an overall LIB production emissions reduction of ~ 50% when combined with traditionally-employed cell manufacturing. Strategies towards net-zero GHG emissions for materials production are discussed, and can be realized through further deployment of carbon-based components produced from atmospheric $CO_2$ as current collectors. A significant effort has been concentrated towards reducing overall carbon emissions through deployment of EVs, but to date, LIB materials choices have been made based solely on cost and performance and at the expense of questionable labor practices, public health, geo-political concerns, and large amounts of GHG emissions. Our work here demonstrates a platform that can be used to roadmap sustainable materials choices to be implemented into LIBs for EV applications, which result in the

realization of high performance and low-cost LIBs without compromising on factors that contribute towards sustainability.

# Chapter 8

Conclusions and Future Outlook

## 8.1 Conclusions

Herein I have demonstrated a novel technique for the manufacturing of carbon nanomaterials through electrochemical capture and conversion of atmospheric carbon dioxide and the use of these carbon nanomaterials in a variety of energy storage applications including large-diameter defective CNTs as anodes in $Li^+$ and $Na^+$ ion batteries and smaller-diameter graphitic CNTs as conductive additives in LFP cathodes coupled with CNT anodes. The full-cell architecture demonstrated using LFP cathodes and CNT anodes provides a platform towards the production of LIBs with net-zero $CO_2$ emissions, a goal we will need to work towards to improve the sustainability of energy storage technologies. Beyond applications in energy storage devices, I demonstrate here work towards controlling the electrochemical growth of carbon materials from ambient carbon dioxide, and mechanistic understanding of catalytic processes that in some cases mimic and other cases diverge from phenomena observed in gas-phase CNT growth using CVD techniques.

Early experimental work in this dissertation (Chapter 2) demonstrate the synthesis of ultrafine $FeS_2$ nanoparticles and use of the nanoparticles as cathode materials in both $Li^+$ and $Na^+$ ion cell configurations. The reaction mechanism between $FeS_2$ and $Li^+$ (or $Na^+$) relies on a conversion reaction that results in $M_2S$ (M = Li or Na) and metallic Fe. Electrochemical analysis reveals much higher performance for the ultrafine nanoparticles compared to their bulk powder counterparts, and specific mechanistic understanding is gained through *ex-situ* TEM and Raman analysis. *Ex-situ* TEM analysis reveals that due to the slow diffusion of Fe, only surface-level

conversion takes place in the bulk flakes, while complete conversion was made possible in the ultrafine particles due to their nanostructure with diameters ~ 2X the diffusion length of Fe.

Nanostructured anode materials have also been an exciting area of energy storage research, and nanostructured carbons with a high defect content have been studied for their ability to intercalate $Na^+$ ions, while bulk graphite cannot. In chapter 3, I studied the effects of defect content in CNTs grown through electrochemical reduction of atmospheric $CO_2$ when assembled into anodes for $Li^+$ and $Na^+$ batteries. This work demonstrated the first studies of tuning CNT properties through this electrochemical growth technique (such as defect content) for energy storage applications. However, many limitations existed in the synthesis method utilized in this study. Most importantly, the CNTs were catalyzed via *in-situ* deposited metallic particles that were either derived from a corrosive anode or from metal salts added into the electrolyte and deposited onto the cathode surface prior to carbon deposition. As elucidated in decades of gas-phase CNT growth studies, the catalyst particle dictates the structure of the resulting CNT grown from it, and being able to control catalyst properties such as size, morphology, and chemical species is critical towards controlling the growth of CNTs using this technique. The shortcomings of this approach motivated the development of a completely inert anode consisting of $Al_2O_3$ coatings applied to Ni wire via atomic layer deposition, which is developed in Chapter 4. This development allows for decoupling of dynamic processes taking place at both the anode and cathode that would influence the catalyst structure that dictates CNT growth, and activates catalyst materials that are solely present at the cathode to be utilized for CNT growth. This development enabled studies of catalyst materials inherent to steel wires and foils (Chapter 4), bulk scrap brass and steel structures (Chapter 5), and pre-deposited catalytic films onto a catalytically-inert surface of stainless steel (Chapter 6).

We demonstrated the ability to isolate iron-based catalyst materials present in bulk steels by using the inert $Al_2O_3$-coated Ni anode and study the migration effect of catalyst materials through bulk to various surfaces in different steels. We observe a high concentration of CNTs in the carbon products produced from galvanized steel cathodes at moderate current densities due to the migration of Fe particles through the Zinc surface, which is molten at the working temperature of the electrolysis. Further, we observe no mobility of Fe in the case of stainless steel which maintains a chromium oxide coating that prevents Fe migration. This phenomenon is then used in chapter 6, where we intentionally choose stainless steel cathode substrates to deposit Fe films via e-beam to control the amount of catalyst materials present for CNT growth.

The ability to harness catalytic materials from the bulk of metal structures is exploited in chapter 5, where we demonstrate the use of this technique to catalyze CNTs from catalyst particles that exist within scrap brass and steel. In the case of brass, Fe particles are present as impurities and the electrochemical process is employed to purify the impurities and by consuming the Fe particles as catalysts for CNT growth. In the case of the steel, however, the bulk of the material is Fe, and would be fully consumed if the CNT growth were left to run for many cycles. This work presents a route towards recycling scrap materials *and* atmospheric carbon in one electrochemical process.

Relying on the catalytically inert nature of stainless steel foils, demonstrated in chapter 4, we demonstrate the deposition of Fe films in various thicknesses and subsequent growth of CNTs from those films. We demonstrate the influence of catalyst size on resulting CNT diameter, as thicker Fe films will form larger particles through dewetting of the metallic film on the oxide surface of the cathode. Observations of larger diameter CNTs catalyzed from thicker Fe films lead to the understanding that catalyst size determines CNT diameter, analogous to phenomena

observed in CVD growth. Interestingly, time-stop experiments conducted on cathodes with the same film thickness revealed that the median CNT diameter grows as the electrolysis time is increased. This gives rise to the mechanistic understanding that catalytic processes are governed by Ostwald ripening of metallic particles which are free to move in 3 dimensions through a liquid-phase media in this growth technique. Our observations lead to the conclusion that Ostwald ripening effects are indeed exacerbated by the liquid-phase environment compared to those commonly observed in gas-phase CNT growth.

In the culmination of this work, chapter 7 demonstrates the use of $CO_2$-derived CNTs as both an active anode material and a conductive binder with LFP cathodes. These materials choices present a platform towards the sustainable production of LIBs, with conscious decision-making considerate of cost and performance in addition to sustainability factors such as earth abundance, energy required to produce the materials, $CO_2$ and other GHG emissions associated with the production and processing of materials, and geo-political, public health, and human rights concerns that have plagued many materials currently utilized in LIBs today. Overall, this approach demonstrates the ability to select materials that exhibit high performance and lower materials-related $CO_2$ emissions by ~ 65% and overall battery emissions by ~ 50%. Routes towards lowering emissions by 97% are discussed and can also rely on materials produced by electrochemical reduction of $CO_2$.

## 8.2 Future Outlook

Significant work is motivated by the experimental work presented here. With the core technique of $CO_2$ conversion into carbon nanomaterials, much work can be done to further the field in terms of both understanding mechanisms that govern the growth process and controlling

the growth of structures obtained through this technique. Furthermore, the materials synthesized using this technique demonstrate a carbon-negative footprint when coupled with carbon-free electricity sources to power the electrolysis. This presents an exciting new frontier of carbon-negative materials that can be implemented into a variety of devices suitable for applications in energy, defense, medical, electronics, and consumer goods.

As the works presented throughout this dissertation summarize some of the first studies on utilizing the electrochemical reduction of $CO_2$ to produce controllable nanostructures, there are many exciting new directions to further understand dynamic growth mechanisms that dictate carbon growth. Basic scientific understanding of mechanisms that govern the nucleation process of carbon onto the surface of the cathode will lead to a stronger understanding of how to control initial carbon nucleation to drive the formation of various carbon structures and can lead towards the control of growth of highly desirable structures of carbon including a high yield of single-walled CNTs, vertically-aligned CNT arrays, and single- and few-layer graphene sheets. We demonstrate in chapter 6 here the phenomena of Ostwald ripening controlling the mass transfer of catalytic materials and the coarsening of catalyst particles over time to yield larger diameter CNTs. Strategies to control Ostwald ripening and pin catalyst particles in small islands have been demonstrated in gas-phase CNT growth through the use of oxidating species that provide a thin surface oxide to discourage the catalyst particles from coarsening. Chemical strategies towards the oxidation of catalyst particles at the cathode surface may lead to a similar effect, through electrolyte additives or surface species at the cathode-electrolyte interface. Another strategy towards control of Ostwald ripening is through electrochemical parameters, where high-pulsed currents may facilitate rapid reduction of catalyst oxide species and the "pinning" of small individual particles to the cathode surface prior to carbon nucleation. We have performed initial

studies to this effect and see a significant CNT diameter reduction and a tightening of the diameter range when catalyst films are subjected to a high pulsed current (500 mA/cm2) for a brief time (~ 30 seconds) prior to the sustaining carbon deposition current (100 mA/cm2) for CNT growth.

Additionally, the only catalyst systems studied to date in this electrochemical growth system are Fe, Ni, or bimetallic combinations of both. A variety of catalyst species have been demonstrated in CVD growth of CNTs, with the most prevalent being the CoMo catalyst system that is responsible for HiPCO growth of single-walled CNTs. Studies on alternative catalyst species such as bimetallic particles or high melting-point materials that may be more resistive to Ostwald ripening in the liquid growth environment are an exciting direction that warrants further investigation. Beyond a new horizon of catalyst species also exists alternative methods for catalyst deposition, as many have been studied in CVD growth but have not been applied to the electrochemical growth of CNTs from $CO_2$.

Finally, the work demonstrated here using $CO_2$-derived CNTs in LIB architectures demonstrates a 65% reduction in materials-related $CO_2$ emissions by replacing conventionally-utilized graphite anodes with $CO_2$-derived CNTs, and using earth-abundant LFP materials that require low energy for production as cathodes coupled with CNT binders. While these approaches address materials that today account for 68% of the $CO_2$ footprint of LIB materials, future studies should address the remaining significant $CO_2$ contributors such as the current collectors. Recent reports in literature have studied the use of CNT "webs" as current collectors for LIBs, so development of CNT sheets that can be coated with active materials and replace metal foils can lead to overall an $CO_2$ footprint reduction for materials towards 97%, and also significant light-weighting of the overall battery, as metallic current collectors today account for a significant portion of the mass.

REFERENCES


1. N. S. Lewis, Aspects of Science and Technology in Support of Legal and Policy Frameworks Associated with a Global Carbon Emissions-Control Regime, *Energy Environ. Sci.*, 2016, **9**, 2172-2176.

2. M. McNutt, Climate Warning, 50 Years Later, *Science*, 2015, **350**, 721-721.

3. P. Jin, T. F. Wang, N. N. Liu, S. Dupont, J. Beardall, P. W. Boyd, U. Riebesell, and K. S. Gao, Ocean Acidification Increases the Accumulation of Toxic Phenolic Compounds across Trophic Levels, *Nature Communications*, 2015, **6**.

4. P. Martens, and S. C. Moser, Health Impacts of Climate Change, *Science*, 2001, **292**, 1065-1066.

5. P. N. Pearson, and M. R. Palmer, Atmospheric Carbon Dioxide Concentrations over the Past 60 Million Years, *Nature*, 2000, **406**, 695-699.

6. M. Pagani, Z. H. Liu, J. LaRiviere, and A. C. Ravelo, High Earth-System Climate Sensitivity Determined from Pliocene Carbon Dioxide Concentrations, *Nat. Geosci.*, 2010, **3**, 27-30.

7. P. Friedlingstein, P. Cox, R. Betts, L. Bopp, W. Von Bloh, V. Brovkin, P. Cadule, S. Doney, M. Eby, I. Fung, G. Bala, J. John, C. Jones, F. Joos, T. Kato, M. Kawamiya, W. Knorr, K. Lindsay, H. D. Matthews, T. Raddatz, P. Rayner, C. Reick, E. Roeckner, K. G. Schnitzler, R. Schnur, K. Strassmann, A. J. Weaver, C. Yoshikawa, and N. Zeng, Climate-Carbon Cycle Feedback Analysis: Results from the (Cmip)-M-4 Model Intercomparison, *J. Clim.*, 2006, **19**, 3337-3353.

8. H. Arakawa, M. Aresta, J. N. Armor, M. A. Barteau, E. J. Beckman, A. T. Bell, J. E. Bercaw, C. Creutz, E. Dinjus, D. A. Dixon, K. Domen, D. L. DuBois, J. Eckert, E. Fujita, D. H. Gibson, W. A. Goddard, D. W. Goodman, J. Keller, G. J. Kubas, H. H. Kung, J. E. Lyons, L. E. Manzer, T. J. Marks, K. Morokuma, K. M. Nicholas, R. Periana, L. Que, J. Rostrup-Nielson, W. M. H. Sachtler, L. D. Schmidt, A. Sen, G. A. Somorjai, P. C. Stair, B. R. Stults, and W. Tumas, Catalysis Research of Relevance to Carbon Management: Progress, Challenges, and Opportunities, *Chem. Rev.*, 2001, **101**, 953-996.

9. *National Academies of Sciences, Engineering, and Medicine: Negative Emissions Technologies and Reliable Sequestration*, 2018.

10. *Vehicle Technologies Office Fy 2015 Budget at-a-Glance; U.S. Department of Energy*, Washington, DC, 2014.

11. K. Turcheniuk, D. Bondarev, V. Singhal, and G. Yushin, Ten Years Left to Redesign Lithium-Ion Batteries Reserves of Rare Metals Used in Electric-Vehicle Cells Are Dwindling, So Boost Research on Iron and Silicon Alternatives, Urge Kostiantyn Turcheniuk and Colleagues., *Nature*, 2018, **559**, 467-470.

12. D. Larcher, and J. M. Tarascon, Towards Greener and More Sustainable Batteries for Electrical Energy Storage, *Nat. Chem.*, 2015, **7**, 19-29.

13. C. Bommier, T. W. Surta, M. Dolgos, and X. L. Ji, New Mechanistic Insights on Na-Ion Storage in Nongraphitizable Carbon, *Nano Lett.*, 2015, **15**, 5888-5892.

14. V. Palomares, M. Casas-Cabanas, E. Castillo-Martinez, M. H. Han, and T. Rojo, Update on Na-Based Battery Materials. A Growing Research Path, *Energy Environ. Sci.*, 2013, **6**, 2312-2337.

15. J. L. Sullivan, and L. A. Gaines, *A Review of Battery Life-Cycle Analysis: State of Knowledge and Critical Needs*, 2010.

16. D. L. Plata, A. J. Hart, C. M. Reddy, and P. M. Gschwend, Early Evaluation of Potential Environmental Impacts of Carbon Nanotube Synthesis by Chemical Vapor Deposition, *Environ. Sci. Technol.*, 2009, **43**, 8367-8373.

17. H. R. Jhong, S. C. Ma, and P. J. A. Kenis, Electrochemical Conversion of Co2 to Useful Chemicals: Current Status, Remaining Challenges, and Future Opportunities, *Current Opinion in Chemical Engineering*, 2013, **2**, 191-199.

18. J. E. Bara, D. E. Camper, D. L. Gin, and R. D. Noble, Room-Temperature Ionic Liquids and Composite Materials: Platform Technologies for Co2 Capture, *Acc. Chem. Res.*, 2010, **43**, 152-159.

19. M. D. Ingram, B. Baron, and G. J. Janz, The Electrolytic Deposition of Carobn from Fused Carbonates, *Electrochem. Acta.*, 1966, **11**, 1629-1639.

20. H. Kawamura, and Y. Ito, Electrodeposition of Cohesive Carbon Films on Aluminum in a Licl-Kcl-K2co3 Melt, *J. Appl. Electrochem.*, 2000, **30**, 571-574.

21. B. Kaplan, H. Groult, A. Barhoun, F. Lantelme, T. Nakajima, V. Gupta, S. Komaba, and N. Kumagai, Synthesis and Structural Characterization of Carbon Powder by Electrolytic Reduction of Molten Li2co3-Na2co3-K2co3, *J. Electrochem.Soc.*, 2002, **149**, D72-D78.

22. V. Kaplan, E. Wachtel, K. Gartsman, Y. Feldman, and I. Lubomirsky, Conversion of Co2 to Co by Electrolysis of Molten Lithium Carbonate, *J. Electrochem. Soc.*, 2010, **157**, B552-B556.

23. K. Le Van, H. Groult, F. Lantelme, M. Dubois, D. Avignant, A. Tressaud, S. Komaba, N. Kumagai, and S. Sigrist, Electrochemical Formation of Carbon Nano-Powders with Various Porosities in Molten Alkali Carbonates, *Electrochem. Acta.*, 2009, **54**, 4566-4573.

24. H. V. Ijije, R. C. Lawrence, N. J. Siambun, S. M. Jeong, D. A. Jewell, D. Hu, and G. Z. Chen, Electro-Deposition and Re-Oxidation of Carbon in Carbonate-Containing Molten Salts, *Farad. Discuss.*, 2014, **172**, 105-116.

25. L. W. Hu, Y. Song, J. B. Ge, J. Zhu, and S. Q. Jiao, Capture and Electrochemical Conversion of Co2 to Ultrathin Graphite Sheets in Cacl2-Based Melts, *J. Mater. Chem. A*, 2015, **3**, 21211-21218.

26. L. W. Hu, Y. Song, S. Q. Jiao, Y. J. Liu, J. B. Ge, H. D. Jiao, J. Zhu, J. X. Wang, H. M. Zhu, and D. J. Fray, Direct Conversion of Greenhouse Gas Co2 into Graphene Via Molten Salts Electrolysis, *Chemsuschem*, 2016, **9**, 588-594.

27. I. Crassous, H. Groult, F. Lantelme, D. Devilliers, A. Tressaud, C. Labrugere, M. Dubois, C. Belhomme, A. Colisson, and B. Morel, Study of the Fluorination of Carbon Anode in Molten Kf-2hf by Xps and Nmr Investigations, *Journal of Fluorine Chemistry*, 2009, **130**, 1080-1085.

28. A. Demirbas, T. Ozturk, and M. F. Demirbas, Recovery of Energy and Chemicals from Carbonaceous Materials, *Energy Sources Part a-Recovery Utilization and Environmental Effects*, 2006, **28**, 1473-1482.

29. S. J. An, J. L. Li, C. Daniel, D. Mohanty, S. Nagpure, and D. L. Wood, The State of Understanding of the Lithium-Ion-Battery Graphite Solid Electrolyte Interphase (Sei) and Its Relationship to Formation Cycling, *Carbon*, 2016, **105**, 52-76.

30. H. Yin, Mao, X., Tang, D., Xiao, W., Xing, L., Zhu, H., Wang, D., Sadoway, D. R., Capture and Electrochemical Conversion of Co2 to Value-Added Carbon and Oxygen by Molten Salt Electrolysis, *Energ. Environ. Sci.*, 2013, **6**, 1538-1545.

31. S. Iijima, Helical Microtubules of Graphitic Carbon, *Nature*, 1991, **354**, 56-58.

32. M. F. L. De Volder, S. H. Tawfick, R. H. Baughman, and A. J. Hart, Carbon Nanotubes: Present and Future Commercial Applications, *Science*, 2013, **339**, 535-539.

33. M. Baibarac, and P. Gomez-Romero, Nanocomposites Based on Conducting Polymers and Carbon Nanotubes: From Fancy Materials to Functional Applications, *Journal of Nanoscience and Nanotechnology*, 2006, **6**, 289-302.

34. A. M. Thayer, Carbon Nanotubes by the Metric Ton, *Chem. Eng. News*, 2007, **85**, 29-35.

35. Y. T. Yeh, Y. Tang, A. Sebastian, A. Dasgupta, N. Perea-Lopez, I. Albert, H. G. Lu, M. Terrones, and S. Y. Zheng, Tunable and Label-Free Virus Enrichment for Ultrasensitive Virus Detection Using Carbon Nanotube Arrays, *Science Advances*, 2016, **2**.

36. G. Centi, and S. Perathoner, The Role of Nanostructure in Improving the Performance of Electrodes for Energy Storage and Conversion, *European Journal of Inorganic Chemistry*, 2009, DOI: 10.1002/ejic.200900275, 3851-3878.

37. R. Carter, L. Oakes, A. P. Cohn, J. Holzgrafe, H. F. Zarick, S. Chatterjee, R. Bardhan, and C. L. Pint, Solution Assembled Single-Walled Carbon Nanotube Foams: Superior Performance in Supercapacitors, Lithium-Ion, and Lithium-Air Batteries, *J. Phys. Chem. C*, 2014, **118**, 20137-20151.

38. R. Das, M. E. Ali, S. B. Abd Hamid, S. Ramakrishna, and Z. Z. Chowdhury, Carbon Nanotube Membranes for Water Purification: A Bright Future in Water Desalination, *Desalination*, 2014, **336**, 97-109.

39. P. Bondavalli, Carbon Nanotubes Based Transistors Composed of Single-Walled Carbon Nanotubes Mats as Gas Sensors: A Review, *Comptes Rendus Physique*, 2010, **11**, 389-396.

40. N. Li, Y. Huang, F. Du, X. B. He, X. Lin, H. J. Gao, Y. F. Ma, F. F. Li, Y. S. Chen, and P. C. Eklund, Electromagnetic Interference (Emi) Shielding of Single-Walled Carbon Nanotube Epoxy Composites, *Nano Letters*, 2006, **6**, 1141-1145.

41. G. D. Nessim, M. Seita, D. L. Plata, K. P. O'Brien, A. J. Hart, E. R. Meshot, C. M. Reddy, P. M. Gschwend, and C. V. Thompson, Precursor Gas Chemistry Determines the Crystallinity of Carbon Nanotubes Synthesized at Low Temperature, *Carbon*, 2011, **49**, 804-810.

42. X. Z. Liao, A. Serquis, Q. X. Jia, D. E. Peterson, Y. T. Zhu, and H. F. Xu, Effect of Catalyst Composition on Carbon Nanotube Growth, *Appl. Phys. Lett.*, 2003, **82**, 2694-2696.

43. A. W. Orbaek, A. C. Owens, C. C. Crouse, C. L. Pint, R. H. Hauge, and A. R. Barron, Single Walled Carbon Nanotube Growth and Chirality Dependence on Catalyst Composition, *Nanoscale*, 2013, **5**, 9848-9859.

44. P. B. Amama, C. L. Pint, S. M. Kim, L. McJilton, K. G. Eyink, E. A. Stach, R. H. Hauge, and B. Maruyama, Influence of Alumina Type on the Evolution and Activity of Alumina-Supported Fe Catalysts in Single-Walled Carbon Nanotube Carpet Growth, *ACS Nano*, 2010, **4**, 895-904.

45. P. B. Amama, C. L. Pint, F. Mirri, M. Pasquali, R. H. Hauge, and B. Maruyama, Catalyst-Support Interactions and Their Influence in Water-Assisted Carbon Nanotube Carpet Growth, *Carbon*, 2012, **50**, 2396-2406.

46. S. M. Kim, C. L. Pint, P. B. Amama, R. H. Hauge, B. Maruyama, and E. A. Stach, Catalyst and Catalyst Support Morphology Evolution in Single-Walled Carbon Nanotube Supergrowth: Growth Deceleration and Termination, *J. Mater. Res.*, 2010, **25**, 1875-1885.

47. C. J. Lee, J. Park, Y. Huh, and J. Y. Lee, Temperature Effect on the Growth of Carbon Nanotubes Using Thermal Chemical Vapor Deposition, *Chem. Phys. Lett.*, 2001, **343**, 33-38.

48. C. L. Pint, N. Nicholas, S. T. Pheasant, J. G. Duque, A. Nicholas, G. Parra-Vasquez, G. Eres, M. Pasquali, and R. H. Hauge, Temperature and Gas Pressure Effects in Vertically Aligned Carbon Nanotube Growth from Fe-Mo Catalyst, *J. Phys. Chem. C*, 2008, **112**, 14041-14051.

49. A. A. Puretzky, Geohegan, D. B., Jesse, S., Ivanov, I. N. and Eres, G., In Situ Measurements and Modeling of Carbon Nanotube Array Growth Kinetics During Chemical Vapor Deposition., *Appl. Phys. A*, 2005, **81**, 223-240.

50. P. B. Amama, C. L. Pint, L. McJilton, S. M. Kim, E. A. Stach, P. T. Murray, R. H. Hauge, and B. Maruyama, Role of Water in Super Growth of Single-Walled Carbon Nanotube Carpets, *Nano Lett.*, 2009, **9**, 44-49.

51. M. Bedewy, and A. J. Hart, Mechanical Coupling Limits the Density and Quality of Self-Organized Carbon Nanotube Growth, *Nanoscale*, 2013, **5**, 2928-2937.

52. M. Bedewy, E. R. Meshot, and A. J. Hart, Diameter-Dependent Kinetics of Activation and Deactivation in Carbon Nanotube Population Growth, *Carbon*, 2012, **50**, 5106-5116.

53. M. R. Maschmann, Integrated Simulation of Active Carbon Nanotube Forest Growth and Mechanical Compression, *Carbon*, 2015, **86**, 26-37.

54. S. Licht, A. Douglas, J. W. Ren, R. Carter, M. Lefler, and C. L. Pint, Carbon Nanotubes Produced from Ambient Carbon Dioxide for Environmentally Sustainable Lithium-Ion and Sodium-Ion Battery Anodes, *ACS Cent. Sci.*, 2016, **2**, 162-168.

55. V. Jourdain, and C. Bichara, Current Understanding of the Growth of Carbon Nanotubes in Catalytic Chemical Vapour Deposition, *Carbon*, 2013, **58**, 2-39.

56. M. Kumar, and Y. Ando, Chemical Vapor Deposition of Carbon Nanotubes: A Review on Growth Mechanism and Mass Production, *Journal of Nanoscience and Nanotechnology*, 2010, **10**, 3739-3758.

57. J. P. Tessonnier, and D. S. Su, Recent Progress on the Growth Mechanism of Carbon Nanotubes: A Review, *Chemsuschem*, 2011, **4**, 824-847.

58. H. U. Rashid, K. C. Yu, M. N. Umar, M. N. Anjum, K. Khan, N. Ahmad, and M. T. Jans, Catalyst Role in Chemical Vapor Deposition (Cvd) Process: A Review, *Reviews on Advanced Materials Science*, 2015, **40**, 235-248.

59. J. Prasek, J. Drbohlavova, J. Chomoucka, J. Hubalek, O. Jasek, V. Adam, and R. Kizek, Methods for Carbon Nanotubes Synthesis-Review, *J. Mater. Chem.*, 2011, **21**, 15872-15884.

60. J. W. Ren, F. F. Li, J. Lau, L. Gonzalez-Urbina, and S. Licht, One-Pot Synthesis of Carbon Nanofibers from Co2, *Nano Lett.*, 2015, **15**, 6142-6148.

61. D. C. Meier, and D. W. Goodman, The Influence of Metal Cluster Size on Adsorption Energies: Co Adsorbed on Au Clusters Supported on Tio2, *Journal of the American Chemical Society*, 2004, **126**, 1892-1899.

62. H. Tsunoyama, H. Sakurai, and T. Tsukuda, Size Effect on the Catalysis of Gold Clusters Dispersed in Water for Aerobic Oxidation of Alcohol, *Chemical Physics Letters*, 2006, **429**, 528-532.

63. M. Hoch, Phase-Stability of Carbon in Fcc and Bcc Metals, *Calphad-Computer Coupling of Phase Diagrams and Thermochemistry*, 1988, **12**, 83-88.

64. O. V. Yazyev, and A. Pasquarello, Effect of Metal Elements in Catalytic Growth of Carbon Nanotubes, *Physical Review Letters*, 2008, **100**.

65. R. T. Yang, P. J. Goethel, J. M. Schwartz, and C. R. F. Lund, Solubility and Diffusivity of Carbon in Metals, *Journal of Catalysis*, 1990, **122**, 206-210.

66. S. M. Kim, C. L. Pint, P. B. Amama, D. N. Zakharov, R. H. Hauge, B. Maruyama, and E. A. Stach, Evolution in Catalyst Morphology Leads to Carbon Nanotube Growth Termination, *J. Phys. Chem. Lett.*, 2010, **1**, 918-922.

67. E. Teblum, Y. Gofer, C. L. Pint, and G. D. Nessim, Role of Catalyst Oxidation State in the Growth of Vertically Aligned Carbon Nanotubes, *J. Phys. Chem. C*, 2012, **116**, 24522-24528.

68. S. Helveg, C. Lopez-Cartes, J. Sehested, P. L. Hansen, B. S. Clausen, J. R. Rostrup-Nielsen, F. Abild-Pedersen, and J. K. Norskov, Atomic-Scale Imaging of Carbon Nanofibre Growth, *Nature*, 2004, **427**, 426-429.

69. S. Hofmann, R. Sharma, C. Ducati, G. Du, C. Mattevi, C. Cepek, M. Cantoro, S. Pisana, A. Parvez, F. Cervantes-Sodi, A. C. Ferrari, R. Dunin-Borkowski, S. Lizzit, L. Petaccia, A. Goldoni, and J. Robertson, In Situ Observations of Catalyst Dynamics During Surface-Bound Carbon Nanotube Nucleation, *Nano Lett.*, 2007, **7**, 602-608.

70. H. Yoshida, S. Takeda, T. Uchiyama, H. Kohno, and Y. Homma, Atomic-Scale in-Situ Observation of Carbon Nanotube Growth from Solid State Iron Carbide Nanoparticles, *Nano Lett.*, 2008, **8**, 2082-2086.

71. J. W. Ren, J. Lau, M. Lefler, and S. Licht, The Minimum Electrolytic Energy Needed to Convert Carbon Dioxide to Carbon by Electrolysis in Carbonate Melts, *J. Phys. Chem. C*, 2015, **119**, 23342-23349.

72. H. J. Wu, Z. D. Li, D. Q. Ji, Y. Liu, L. L. Li, D. D. Yuan, Z. H. Zhang, J. W. Ren, M. Lefler, B. H. Wang, and S. Licht, One-Pot Synthesis of Nanostructured Carbon Materials from Carbon Dioxide Via Electrolysis in Molten Carbonate Salts, *Carbon*, 2016, **106**, 208-217.

73. B. Kaplan, H. Groult, S. Komaba, N. Kumagai, and F. Lantelme, Synthesis of Nanostructured Carbon Material by Electroreduction in Fused Alkali Carbonates, *Chem. Lett.*, 2001, 714-715.

74. *Smithers Apex the Future of Carbon Fibre to 2021*, 2016.

75. Global Market Insights: Carbon Nanotubes Market Size by Product, 2016.

76. Grand View Research: Carbon Black Market Analysis by Application (Tires, High Performance Coatings, Plastics) and Segment Forecasts to 2022, 2016.

77. Bcc Research: Graphene: Technologies, Applications and Markets, 2016.

78. Grand View Research: Activated Carbon Market Analysis by Product, 2016.

79. A. S. Arico, P. Bruce, B. Scrosati, J. M. Tarascon, and W. Van Schalkwijk, Nanostructured Materials for Advanced Energy Conversion and Storage Devices, *Nat. Mater.*, 2005, **4**, 366-377.

80. R. Bardhan, L. O. Hedges, C. L. Pint, A. Javey, S. Whitelam, and J. J. Urban, Uncovering the Intrinsic Size Dependence of Hydriding Phase Transformations in Nanocrystals, *Nat. Mater.*, 2013, **12**, 905-912.

81. Y. G. Guo, J. S. Hu, and L. J. Wan, Nanostructured Materials for Electrochemical Energy Conversion and Storage Devices (Vol 20, Pg 2878, 2008), *Adv. Mater.*, 2008, **20**, 4384-4384.

82. P. G. Bruce, B. Scrosati, and J. M. Tarascon, Nanomaterials for Rechargeable Lithium Batteries, *Angew. Chem.*, 2008, **47**, 2930-2946.

83. W. L. Liu, X. H. Rui, H. T. Tan, C. Xu, Q. Y. Yan, and H. H. Hng, Solvothermal Synthesis of Pyrite Fes2 Nanocubes and Their Superior High Rate Lithium Storage Properties, *RSC Adv.*, 2014, **4**, 48770-48776.

84. M. Caban-Acevedo, N. S. Kaiser, C. R. English, D. Liang, B. J. Thompson, H. E. Chen, K. J. Czech, J. C. Wright, R. J. Hamers, and S. Jin, Ionization of High-Density Deep Donor Defect States Explains the Low Photovoltage of Iron Pyrite Single Crystals, *J. Am. Chem. Soc.*, 2014, **136**, 17163-17179.

85. P. P. Prosini, M. Carewska, S. Scaccia, P. Wisniewski, and M. Pasquali, Long-Term Cyclability of Nanostructured Lifepo4, *Electrochem. Acta.*, 2003, **48**, 4205-4211.

86. N. C. Li, C. R. Martin, and B. Scrosati, Nanomaterial-Based Li-Ion Battery Electrodes, *J. Power Sources*, 2001, **97-8**, 240-243.

87. L. W. Ji, Z. Lin, M. Alcoutlabi, and X. W. Zhang, Recent Developments in Nanostructured Anode Materials for Rechargeable Lithium-Ion Batteries, *Energy Environ. Sci.*, 2011, **4**, 2682-2699.

88. C. K. Chan, H. L. Peng, G. Liu, K. McIlwrath, X. F. Zhang, R. A. Huggins, and Y. Cui, High-Performance Lithium Battery Anodes Using Silicon Nanowires, *Nat. Nanotechnol.*, 2008, **3**, 31-35.

89. A. S. Westover, D. Freudiger, Z. S. Gani, K. Share, L. Oakes, R. E. Carter, and C. L. Pint, On-Chip High Power Porous Silicon Lithium Ion Batteries with Stable Capacity over 10 000 Cycles, *Nanoscale*, 2015, **7**, 98-103.

90. H. Li, X. J. Huang, L. Q. Chen, Z. G. Wu, and Y. Liang, A High Capacity Nano-Si Composite Anode Material for Lithium Rechargeable Batteries, *Electrochem. Solid State Lett.*, 1999, **2**, 547-549.

91. U. Kasavajjula, C. S. Wang, and A. J. Appleby, Nano- and Bulk-Silicon-Based Insertion Anodes for Lithium-Ion Secondary Cells, *J. Power Sources*, 2007, **163**, 1003-1039.

92. H. Kim, M. Seo, M. H. Park, and J. Cho, A Critical Size of Silicon Nano-Anodes for Lithium Rechargeable Batteries, *Angew. Chem.*, 2010, **49**, 2146-2149.

93. C. Kim, M. Noh, M. Choi, J. Cho, and B. Park, Critical Size of a Nano Sno2 Electrode for Li-Secondary Battery, *Chem. Mater.*, 2005, **17**, 3297-3301.

94. M. He, K. Kraychyk, M. Walter, and M. V. Kovalenko, Monodisperse Antimony Nanocrystals for High-Rate Li-Ion and Na-Ion Battery Anodes: Nano Versus Bulk, *Nano Lett.*, 2014, **14**, 1255-1262.

95. K. Kravchyk, L. Protesescu, M. I. Bodnarchuk, F. Krumeich, M. Yarema, M. Walter, C. Guntlin, and M. V. Kovalenko, Monodisperse and Inorganically Capped Sn and Sn/Sno2 Nanocrystals for High-Performance Li-Ion Battery Anodes, *J. Am. Chem. Soc.*, 2013, **135**, 4199-4202.

96. R. Malini, U. Uma, T. Sheela, M. Ganesan, and N. G. Renganathan, Conversion Reactions: A New Pathway to Realise Energy in Lithium-Ion Battery-Review, *Ionics*, 2009, **15**, 301-307.

97. M. T. McDowell, Z. D. Lu, K. J. Koski, J. H. Yu, G. Y. Zheng, and Y. Cui, In Situ Observation of Divergent Phase Transformations in Individual Sulfide Nanocrystals, *Nano Lett.*, 2015, **15**, 1264-1271.

98. X. Sun, C. G. Zhou, M. Xie, H. T. Sun, T. Hu, F. Y. Lu, S. M. Scott, S. M. George, and J. Lian, Synthesis of Zno Quantum Dot/Graphene Nanocomposites by Atomic Layer Deposition with High Lithium Storage Capacity, *J. Mater. Chem. A*, 2014, **2**, 7319-7326.

99. H. W. Song, N. Li, H. Cui, and C. X. Wang, Enhanced Capability and Cyclability of Sno2-Graphene Oxide Hybrid Anode by Firmly Anchored Sno2 Quantum Dots, *J. Mater. Chem. A*, 2013, **1**, 7558-7562.

100. C. X. Peng, B. D. Chen, Y. Qin, S. H. Yang, C. Z. Li, Y. H. Zuo, S. Y. Liu, and J. H. Yang, Facile Ultrasonic Synthesis of Coo Quantum Dot/Graphene Nanosheet Composites with High Lithium Storage Capacity, *ACS Nano*, 2012, **6**, 1074-1081.

101. X. Y. Zhou, J. J. Shi, Y. Liu, Q. M. Su, J. Zhang, and G. H. Du, Microwave Irradiation Synthesis of Co3o4 Quantum Dots/Graphene Composite as Anode Materials for Li-Ion Battery, *Electrochem. Acta.*, 2014, **143**, 175-179.

102. J. H. Chen, and W. W. Harvey, Cation Self-Diffusion in Chalcopyrite and Pyrite, *Metall. Mater. Trans. B*, 1975, **6**, 331.

103. E. Strauss, D. Golodnitsky, and E. Peled, Study of Phase Changes During 500 Full Cycles of Li/Composite Polymer Electrolyte/Fes2 Battery, *Electrochem. Acta.*, 2000, **45**, 1519-1525.

104. D. Zhang, Y. J. Mai, J. Y. Xiang, X. H. Xia, Y. Q. Qiao, and J. P. Tu, Fes2/C Composite as an Anode for Lithium Ion Batteries with Enhanced Reversible Capacity, *J. Power Sources*, 2012, **217**, 229-235.

105. S. Y. Huang, X. Y. Liu, Q. Y. Li, and J. Chen, Pyrite Film Synthesized for Lithium-Ion Batteries, *J. Alloy Compd.*, 2009, **472**, L9-L12.

106. Y. R. Wang, H. T. Liao, J. Wang, X. F. Qian, Y. C. Zhu, and S. Q. Cheng, Effects of Current Collectors on Electrochemical Performance of Fes2 for Li-Ion Battery, *J. Electrochem. Sci.*, 2013, **8**, 4002-4009.

107. R. Fong, J. R. Dahn, and C. H. W. Jones, Electrochemistry of Pyrite-Based Cathodes for Ambient-Temperature Lithium Batteries, *J. Electrochem. Soc.*, 1989, **136**, 3206-3210.

108. J. Cabana, L. Monconduit, D. Larcher, and M. R. Palacin, Beyond Intercalation-Based Li-Ion Batteries: The State of the Art and Challenges of Electrode Materials Reacting through Conversion Reactions, *Adv. Mater.*, 2010, **22**, E170-E192.

109. Z. Hu, Z. Q. Zhu, F. Y. Cheng, K. Zhang, J. B. Wang, C. C. Chen, and J. Chen, Pyrite Fes2 for High-Rate and Long-Life Rechargeable Sodium Batteries, *Energy Environ. Sci.*, 2015, **8**, 1309-1316.

110. T. B. Kim, J. W. Choi, H. S. Ryu, G. B. Cho, K. W. Kim, J. H. Ahn, K. K. Cho, and H. J. Ahn, Electrochemical Properties of Sodium/Pyrite Battery at Room Temperature, *J. Power Sources*, 2007, **174**, 1275-1278.

111. Z. Shadike, Y. N. Zhou, F. Ding, L. Sang, K. W. Nam, X. Q. Yang, and Z. W. Fu, The New Electrochemical Reaction Mechanism of Na/Fes2 Cell at Ambient Temperature, *J. Power Sources*, 2014, **260**, 72-76.

112. M. Walter, T. Zund, and M. V. Kovalenko, Pyrite (Fes2) Nanocrystals as Inexpensive High-Performance Lithium-Ion Cathode and Sodium-Ion Anode Materials, *Nanoscale*, 2015, **7**, 9158-9163.

113. D. Golodnitsky, and E. Peled, Pyrite as Cathode Insertion Material in Rechargeable Lithium/Composite Polymer Electrolyte Batteries, *Electrochem. Acta.*, 1999, **45**, 335-350.

114. T. A. Yersak, H. A. Macpherson, S. C. Kim, V. D. Le, C. S. Kang, S. B. Son, Y. H. Kim, J. E. Trevey, K. H. Oh, C. Stoldt, and S. H. Lee, Solid State Enabled Reversible Four Electron Storage, *Adv. Energy Mater.*, 2013, **3**, 120-127.

115. J. P. Wilcoxon, P. P. Newcomer, and G. A. Samara, Strong Quantum Confinement Effects in Semiconductors: Fes2 Nanoclusters, *Solid State Commun.*, 1996, **98**, 581-585.

116. Y. X. Bai, J. Yeom, M. Yang, S. H. Cha, K. Sun, and N. A. Kotov, Universal Synthesis of Single-Phase Pyrite Fes2 Nanoparticles, Nanowires, and Nanosheets, *J. Phys. Chem. C*, 2013, **117**, 2567-2573.

117. K. B. Hueso, M. Armand, and T. Rojo, High Temperature Sodium Batteries: Status, Challenges and Future Trends, *Energy Environ. Sci.*, 2013, **6**, 734-749.

118. T. J. Collins, Imagej for Microscopy, *Biotechniques*, 2007, **43**, 25.

119. Y. Shao-Horn, and Q. C. Horn, Chemical, Structural and Electrochemical Comparison of Natural and Synthetic Fes2 Pyrite in Lithium Cells, *Electrochem. Acta.*, 2001, **46**, 2613-2621.

120. Y. Shao-Horn, S. Osmialowski, and Q. C. Horn, Nano-Fes2 for Commercial Li/Fes2 Primary Batteries, *J. Electrochem. Soc.*, 2002, **149**, A1499-A1502.

121. J. W. Choi, G. Cheruvally, H. J. Ahn, K. W. Kim, and J. H. Ahn, Electrochemical Characteristics of Room Temperature Li/Fes2 Batteries with Natural Pyrite Cathode, *J. Power Sources*, 2006, **163**, 158-165.

122. Y. J. Choi, N. W. Kim, K. W. Kim, K. K. Cho, G. B. Cho, H. J. Ahn, J. H. Ahn, K. S. Ryu, and H. B. Gu, Electrochemical Properties of Nickel-Precipitated Pyrite as Cathode Active Material for Lithium/Pyrite Cell, *J. Alloy Comp.*, 2009, **485**, 462-466.

123. D. Zhang, X. L. Wang, Y. J. Mai, X. H. Xia, C. D. Gu, and J. P. Tu, Enhanced Electrochemical Performance of Fes2 Synthesized by Hydrothermal Method for Lithium Ion Batteries, *J. Appl. Electrochem.*, 2012, **42**, 263-269.

124. C. Rice, R. J. Young, R. Zan, U. Bangert, D. Wolverson, T. Georgiou, R. Jalil, and K. S. Novoselov, Raman-Scattering Measurements and First-Principles Calculations of Strain-Induced Phonon Shifts in Monolayer Mos2, *Phys. Rev. B*, 2013, **87**.

125. W. B. Pearson, *A Handbook of Lattice Spacings and Structures of Metals and Alloys*, Pergamon Press, New York, 1958.

126. D. H. Son, S. M. Hughes, Y. D. Yin, and A. P. Alivisatos, Cation Exchange Reactions-in Ionic Nanocrystals, *Science*, 2004, **306**, 1009-1012.

127. D. Y. C. Leung, G. Caramanna, and M. M. Maroto-Valer, An Overview of Current Status of Carbon Dioxide Capture and Storage Technologies, *Renew. Sust. Energ. Rev.*, 2014, **39**, 426-443.

128. X. Z. Lim, How to Make the Most of Carbon Dioxide, *Nature*, 2015, **526**, 628-630.

129. B. Dunn, H. Kamath, and J. M. Tarascon, Electrical Energy Storage for the Grid: A Battery of Choices, *Science*, 2011, **334**, 928-935.

130. J. M. Tarascon, Is Lithium the New Gold?, *Nat. Chem.*, 2010, **2**, 510.

131. N. Nitta, F. X. Wu, J. T. Lee, and G. Yushin, Li-Ion Battery Materials: Present and Future, *Mater. Today*, 2015, **18**, 252-264.

132. Z. Xiong, Y. S. Yun, and H. J. Jin, Applications of Carbon Nanotubes for Lithium Ion Battery Anodes, *Materials*, 2013, **6**, 1138-1158.

133. D. Kundu, E. Talaie, V. Duffort, and L. F. Nazar, The Emerging Chemistry of Sodium Ion Batteries for Electrochemical Energy Storage, *Angew. Chem.*, 2015, **54**, 3431-3448.

134. N. Yabuuchi, K. Kubota, M. Dahbi, and S. Komaba, Research Development on Sodium-Ion Batteries, *Chem. Rev.*, 2014, **114**, 11636-11682.

135. Z. Q. Zhu, F. Y. Cheng, Z. Hu, Z. Q. Niu, and J. Chen, Highly Stable and Ultrafast Electrode Reaction of Graphite for Sodium Ion Batteries, *J. Power Sources*, 2015, **293**, 626-634.

136. A. P. Cohn, K. Share, R. Carter, L. Oakes, and C. L. Pint, Ultrafast Solvent-Assisted Sodium Ion Intercalation into Highly Crystalline Few-Layered Graphene, *Nano Lett.*, 2016, **16**, 543-548.

137. K. P. Kuhl, T. Hatsukade, E. R. Cave, D. N. Abram, J. Kibsgaard, and T. F. Jaramillo, Electrocatalytic Conversion of Carbon Dioxide to Methane and Methanol on Transition Metal Surfaces, *J. Am. Chem. Soc.*, 2014, **136**, 14107-14113.

138. S. Menkin, D. Golodnitsky, and E. Peled, Artificial Solid-Electrolyte Interphase (Sei) for Improved Cycleability and Safety of Lithium-Ion Cells for Ev Applications, *Electrochem. Commun.*, 2009, **11**, 1789-1791.

139. J. Ding, H. L. Wang, Z. Li, A. Kohandehghan, K. Cui, Z. W. Xu, B. Zahiri, X. H. Tan, E. M. Lotfabad, B. C. Olsen, and D. Mitlin, Carbon Nanosheet Frameworks Derived from Peat Moss as High Performance Sodium Ion Battery Anodes, *ACS Nano*, 2013, **7**, 11004-11015.

140. E. M. Lotfabad, J. Ding, K. Cui, A. Kohandehghan, W. P. Kalisvaart, M. Hazelton, and D. Mitlin, High-Density Sodium and Lithium Ion Battery Anodes from Banana Peels, *ACS Nano*, 2014, **8**, 7115-7129.

141. S. Licht, Step (Solar Thermal Electrochemical Photo) Generation of Energetic Molecules: A Solar Chemical Process to End Anthropogenic Global Warming, *J. Phys. Chem. C*, 2009, **113**, 16283-16292.

142. S. Licht, B. H. Wang, S. Ghosh, H. Ayub, D. L. Jiang, and J. Ganley, A New Solar Carbon Capture Process: Solar Thermal Electrochemical Photo (Step) Carbon Capture, *J. Phys. Chem. C Lett.*, 2010, **1**, 2363-2368.

143. S. Licht, Efficient Solar-Driven Synthesis, Carbon Capture, and Desalinization, Step: Solar Thermal Electrochemical Production of Fuels, Metals, Bleach, *Adv. Mater.*, 2011, **23**, 5592-5612.

144. S. Licht, B. C. Cui, B. H. Wang, F. F. Li, J. Lau, and S. Z. Liu, Ammonia Synthesis Ammonia Synthesis by N-2 and Steam Electrolysis in Molten Hydroxide Suspensions of Nanoscale Fe2o3, *Science*, 2014, **345**, 637-640.

145. F. F. Li, and S. Licht, Advances in Understanding the Mechanism and Improved Stability of the Synthesis of Ammonia from Air and Water in Hydroxide Suspensions of Nanoscale Fe2o3, *Inorg. Chem.*, 2014, **53**, 10042-10044.

146. Y. J. Zhu, B. H. Wang, X. L. Liu, H. Y. Wang, H. J. Wu, and S. Licht, Step Organic Synthesis: An Efficient Solar, Electrochemical Process for the Synthesis of Benzoic Acid, *Green Chem.*, 2014, **16**, 4758-4766.

147. B. C. Cui, and S. Licht, Critical Step Advances for Sustainable Iron Production, *Green Chem.*, 2013, **15**, 881-884.

148. S. Licht, and H. J. Wu, Step Iron, a Chemistry of Iron Formation without Co2 Emission: Molten Carbonate Solubility and Electrochemistry of Iron Ore Impurities, *J. Phys. Chem. C*, 2011, **115**, 25138-25147.

149. S. Licht, H. J. Wu, C. Hettige, B. H. Wang, J. Asercion, J. Lau, and J. Stuart, Step Cement: Solar Thermal Electrochemical Production of Cao without Co2 Emission, *Chem. Comm.*, 2012, **48**, 6019-6021.

150. M. Saravanan, P. Sennu, M. Ganesan, and S. Ambalavanan, Multi-Walled Carbon Nanotubes Percolation Network Enhanced the Performance of Negative Electrode for Lead-Acid Battery, *J. Electrochem. Soc.*, 2013, **160**, A70-A76.

151. C. A. Schneider, W. S. Rasband, and K. W. Eliceiri, Nih Image to Imagej: 25 Years of Image Analysis, *Nat. Mater.*, 2012, **9**, 671-675.

152. I. Lahiri, S. W. Oh, J. Y. Hwang, S. Cho, Y. K. Sun, R. Banerjee, and W. Choi, High Capacity and Excellent Stability of Lithium Ion Battery Anode Using Interface-Controlled Binder-Free Multiwall Carbon Nanotubes Grown on Copper, *ACS Nano*, 2010, **4**, 3440-3446.

153. Z. J. Fan, J. Yan, G. Q. Ning, T. Wei, L. J. Zhi, and F. Wei, Porous Graphene Networks as High Performance Anode Materials for Lithium Ion Batteries, *Carbon*, 2013, **60**, 558-561.

154. M. Inaba, H. Yoshida, Z. Ogumi, T. Abe, Y. Mizutani, and M. Asano, In-Situ Raman-Study on Electrochemical Li-Intercalation into Graphite, *J. Electrochem. Soc.*, 1995, **142**, 20-26.

155. Y. L. Cao, L. F. Xiao, M. L. Sushko, W. Wang, B. Schwenzer, J. Xiao, Z. M. Nie, L. V. Saraf, Z. G. Yang, and J. Liu, Sodium Ion Insertion in Hollow Carbon Nanowires for Battery Applications, *Nano Lett.*, 2012, **12**, 3783-3787.

156. D. L. Wood, J. L. Li, and C. Daniel, Prospects for Reducing the Processing Cost of Lithium Ion Batteries, *J. Power Sources*, 2015, **275**, 234-242.

157. J. M. Matter, M. Stute, S. O. Snaebjornsdottir, E. H. Oelkers, S. R. Gislason, E. S. Aradottir, B. Sigfusson, I. Gunnarsson, H. Sigurdardottir, E. Gunnlaugsson, G. Axelsson, H. A. Alfredsson, D. Wolff-Boenisch, K. Mesfin, D. F. D. Taya, J. Hall, K. Dideriksen, and W. S. Broecker, Rapid Carbon Mineralization for Permanent Disposal of Anthropogenic Carbon Dioxide Emissions, *Science*, 2016, **352**, 1312-1314.

158. H. Y. Yin, X. H. Mao, D. Y. Tang, W. Xiao, L. R. Xing, H. Zhu, D. H. Wang, and D. R. Sadoway, Capture and Electrochemical Conversion of Co2 to Value-Added Carbon and Oxygen by Molten Salt Electrolysis, *Energy Environ. Sci.*, 2013, **6**, 1538-1545.

159. M. Mikkelsen, M. Jorgensen, and F. C. Krebs, The Teraton Challenge. A Review of Fixation and Transformation of Carbon Dioxide, *Energy Environ. Sci.*, 2010, **3**, 43-81.

160. J. Kothandaraman, A. Goeppert, M. Czaun, G. A. Olah, and G. K. S. Prakash, Conversion of Co2 from Air into Methanol Using a Polyamine and a Homogeneous Ruthenium Catalyst, *J. Am. Chem. Soc.*, 2016, **138**, 778-781.

161. A. Bansode, and A. Urakawa, Towards Full One-Pass Conversion of Carbon Dioxide to Methanol and Methanol-Derived Products, *J. Catal.*, 2014, **309**, 66-70.

162. S. Borman, Carbon Dioxide Hydrogenated to Methanol on Large Scale, *Chem. Eng. News*, 2016, **94**, 7-7.

163. F. Studt, I. Sharafutdinov, F. Abild-Pedersen, C. F. Elkjaer, J. S. Hummelshoj, S. Dahl, I. Chorkendorff, and J. K. Norskov, Discovery of a Ni-Ga Catalyst for Carbon Dioxide Reduction to Methanol, *Nat. Chem.*, 2014, **6**, 320-324.

164. M. Gattrell, N. Gupta, and A. Co, A Review of the Aqueous Electrochemical Reduction of Co2 to Hydrocarbons at Copper, *J. Electroanal. Chem.*, 2006, **594**, 1-19.

165. M. S. Dresselhaus, G. Dresselhaus, R. Saito, and A. Jorio, Raman Spectroscopy of Carbon Nanotubes, *Phys. Rep.*, 2005, **409**, 47-99.

166. E. T. Thostenson, Z. F. Ren, and T. W. Chou, Advances in the Science and Technology of Carbon Nanotubes and Their Composites: A Review, *Compos. Sci. Technol.*, 2001, **61**, 1899-1912.

167. A. A. Puretzky, D. B. Geohegan, S. Jesse, I. N. Ivanov, and G. Eres, In Situ Measurements and Modeling of Carbon Nanotube Array Growth Kinetics During Chemical Vapor Deposition, *Appl. Phys. A*, 2005, **81**, 223-240.

168. G. D. Nessim, Properties, Synthesis, and Growth Mechanisms of Carbon Nanotubes with Special Focus on Thermal Chemical Vapor Deposition, *Nanoscale*, 2010, **2**, 1306-1323.

169. J. W. Ren, and S. Licht, Tracking Airborne Co2 Mitigation and Low Cost Transformation into Valuable Carbon Nanotubes, *Sci. Rep.*, 2016, **6**.

170. C. L. Pint, Y. Q. Xu, S. Moghazy, T. Cherukuri, N. T. Alvarez, E. H. Haroz, S. Mahzooni, S. K. Doorn, J. Kono, M. Pasquali, and R. H. Hauge, Dry Contact Transfer Printing of Aligned Carbon Nanotube Patterns and Characterization of Their Optical Properties for Diameter Distribution and Alignment, *ACS Nano*, 2010, **4**, 1131-1145.

171. P. M. Cox, R. A. Betts, C. D. Jones, S. A. Spall, and I. J. Totterdell, Acceleration of Global Warming Due to Carbon-Cycle Feedbacks in a Coupled Climate Model, *Nature*, 2000, **408**, 184-187.

172. N. S. Lewis, Aspects of Science and Technology in Support of Legal and Policy Frameworks Associated with a Global Carbon Emissions-Control Regime, *Energ. Environ. Sci.*, 2016, **9**, 2172-2176.

173. A. Douglas, and C. L. Pint, Review—Electrochemical Growth of Carbon Nanotubes and Graphene from Ambient Carbon Dioxide: Synergy with Conventional Gas-Phase Growth Mechanisms, *ECS J. Solid State Sci. Technol.*, 2017, **6**, M3084-M3089.

174. *Us Department of the Interior, Us Geological Survey Mineral Commodities Summary 2015*, Reston, VA, 2015.

175. T. G. Goonan, *Copper Recycling in the United States in 2004*, Reston, VA, 2010.

176. R. U. Ayres, Metals Recycling: Economic and Environmental Implications, *Resour. Conserv. Recy.*, 1997, **21**, 145-173.

177. N. Muralidharan, A. S. Westover, H. T. Sun, N. Galioto, R. E. Carter, A. P. Cohn, L. Oakes, and C. L. Pint, From the Junkyard to the Power Grid: Ambient Processing of Scrap Metals into Nanostructured Electrodes for Ultrafast Rechargeable Batteries, *ACS Energy Lett.*, 2016, **1**, 1034-1041.

178. R. J. Damuth, *Iron and Steel Scrap: Accumulation and Availability as of December 31, 2009*, 2010.

179. K. P. Kuhl, E. R. Cave, D. N. Abram, and T. F. Jaramillo, New Insights into the Electrochemical Reduction of Carbon Dioxide on Metallic Copper Surfaces, *Energ. Environ. Sci.*, 2012, **5**, 7050-7059.

180. M. Le, M. Ren, Z. Zhang, P. T. Sprunger, R. L. Kurtz, and J. C. Flake, Electrochemical Reduction of Co2 to Ch3oh at Copper Oxide Surfaces, *J. Electrochem. Soc.*, 2011, **158**, E45-E49.

181. G. Arai, T. Harashina, and I. Yasumori, Selective Electrocatalytic Reduction of Carbon-Dioxide to Methanol on Ru-Modified Electrode, *Chem. Lett.*, 1989, **18**, 1215-1218.

182. M. D. Ingram, B. Baron, and G. J. Janz, The Electrolytic Deposition of Carbon from Fused Carbonates, *Electrochim. Acta*, 1966, **11**, 1629-1639.

183. H. V. Ijije, and G. Z. Chen, Electrochemical Manufacturing of Nanocarbons from Carbon Dioxide in Molten Alkali Metal Carbonate Salts: Roles of Alkali Metal Cations, *Adv. Manuf.*, 2016, **4**, 23-32.

184. K. Le Van, H. Groult, F. Lantelme, M. Dubois, D. Avignant, A. Tressaud, S. Komaba, N. Kumagai, and S. Sigrist, Electrochemical Formation of Carbon Nano-Powders with Various Porosities in Molten Alkali Carbonates, *Electrochim. Acta.*, 2009, **54**, 4566-4573.

185. H. Wu, Li, Z., Ji, D., Liu, Y., Yi, G., Yuan, D., Wang, B., Zhang, Z., Effect of Molten Carbonate Composition on the Generation of Carbon Material, *RSC Adv.*, 2017, **7**, 8467-8473.

186. L. Hu, Song, Y., Ge, J., Zhu, J., Jiao, S., Capture and Electrochemical Conversion of Co2 to Ultrathin Graphite Sheets in Cacl2-Based Melts, *J. Mater. Chem. A*, 2016, **3**, 21211-21218.

187. J. Ge, Hu, L., Song, Y., Jiao, S., An Investigation into the Carbon Nucleation and Growth on a Nickel Substrate in Licl–Li2co3 Melts, *Farad. Discuss.*, 2016, **190**, 259-268.

188. J. Ge, Han, Z., Zhu, J., Jiao, S., Electrochemical Deposition of Carbon Prepared on Cu and Ni Cathodes in Cacl2-Licl Melts, *J. Electrochem. Soc.*, 2017, **164**, D248-D252.

189. A. Douglas, R. Carter, N. Muralidharan, L. Oakes, and C. L. Pint, Iron Catalyzed Growth of Crystalline Multi-Walled Carbon Nanotubes from Ambient Carbon Dioxide Mediated by Molten Carbonates, *Carbon*, 2017, **116**, 572-578.

190. J. W. Ren, J. Lau, M. Lefler, and S. Licht, The Minimum Electrolytic Energy Needed to Convert Carbon Dioxide to Carbon by Electrolysis in Carbonate Melts, *J. Phys. Chem. C.*, 2015, **119**, 23342-23349.

191. H. Almkhelfe, X. Li, R. R., and P. B. Amama, Catalytic Cvd Growth of Millimeter-Tall Single-Wall Carbon Nanotube Carpets Using Industrial Gaseous Waste as a Feedstock, *Carbon*, 2017, **116**, 181-190.

192. M. R. Maschmann, Amama, P. D., Goyal, A., Iqbal, Z., Gat, R., Fisher, T. S., Parametric Study of Synthesis Conditions in Plasma-Enhanced Cvd of High-Quality Single-Walled Carbon Nanotubes, *Carbon*, 2006, **44**, 10-18.

193. M. R. Maschmann, Franklin, A. D., Amama, P. D., Zakharov, D. N., Stach, E. A., Sands, T. D., Fisher, T. S., Vertical Single-and Double-Walled Carbon Nanotubes Grown from Modified Porous Anodic Alumina Templates, *Nanotechnology*, 2006, **17**, 3925.

194. G. D. Nessim, Hart, A. J., Kim J. S., Acquaviva D., Oh, J., Morgan C. D., Seita, M., Leib, J. S., Thompson, C. V., Tuning of Vertically-Aligned Carbon Nanotube Diameter and Areal Density through Catalyst Pre-Treatment, *Nano Lett.*, 2008, **8**, 3587-3593.

195. L. Shi W., J., Polsen E. S., Oliver, C. R., Zhao Y., Meshot E. R., Barclay M., Fairbrother D. H., Hart, A. J., Plata, D. L., Oxygen-Promoted Catalyst Sintering Influences Number

Density, Alignment, and Wall Number of Vertically Aligned Carbon Nanotubes, *Nanoscale*, 2017.

196. D. Park, Y. H. Kim, and J. K. Lee, Synthesis of Carbon Nanotubes on Metallic Substrates by a Sequential Combination of Pecvd and Thermal Cvd, *Carbon*, 2003, **41**, 1025-1029.

197. Y. Soneda, and M. Makino, Formation and Texture of Carbon Nanofilaments by the Catalytic Decomposition of Co on Stainless-Steel Plate, *Carbon*, 2000, **38**, 478-480.

198. C. L. Lin, C. F. Chen, and S. C. Shi, Field Emission Properties of Aligned Carbon Nanotubes Grown on Stainless Steel Using Ch4/Co2 Reactant Gas, *Diamond Relat. Mater.*, 2004, **13**, 1026-1031.

199. R. L. Vander Wal, and L. J. Hall, Carbon Nanotube Synthesis Upon Stainless Steel Meshes, *Carbon*, 2003, **41**, 659-672.

200. M. Karwa, Z. Iqbal, and S. Mitra, Scaled-up Self-Assembly of Carbon Nanotubes inside Long Stainless Steel Tubing, *Carbon*, 2006, **44**, 1235-1242.

201. S. Talapatra, S. Kar, S. K. Pal, R. Vajtai, L. Ci, P. Victor, M. M. Shaijumon, S. Kaur, O. Nalamasu, and P. M. Ajayan, Direct Growth of Aligned Carbon Nanotubes on Bulk Metals, *Nat. Nanotechnol.*, 2006, **1**, 112-116.

202. J. Oliver, *Global Markets and Technologies for Carbon Nanotubes*, BCC Research, Wellesley, MA, 2015.

203. D. Kushnir, and B. A. Sanden, Energy Requirements of Carbon Nanoparticle Production, *J. Ind. Ecol.*, 2008, **12**, 360-375.

204. P. B. Amama, C. L. Pint, S. M. Kim, L. McJilton, K. G. Eyink, E. A. Stach, R. H. Hauge, and B. Maruyama, Influence of Alumina Type on the Tvolution and Activity of Alumina-Supported Fe Catalysts in Single-Walled Carbon Nanotube Carpet Growth, *ACS Nano*, 2010, **4**, 895-904.

205. N. T. Alvarez, F. Li, C. L. Pint, J. T. Mayo, E. Z. Fisher, J. M. Tour, V. L. Colvin, and R. H. Hauge, Uniform Large Diameter Carbon Nanotubes in Vertical Arrays from Premade near-Monodisperse Nanoparticles, *Chem. Mater.*, 2011, **23**, 3466-3475.

206. C. L. Cheung, A. Kurtz, H. Park, and C. M. Lieber, Diameter-Controlled Synthesis of Carbon Nanotubes, *J. Phys. Chem. B*, 2002, **106**, 2429-2433.

207. H. Navas, M. Picher, A. Andrieux-Ledier, F. Fossard, T. Michel, A. Kozawa, T. Maruyama, E. Anglaret, A. Loiseau, and V. Jourdain, Unveiling the Evolutions of Nanotube Diameter Distribution During the Growth of Single-Walled Carbon Nanotubes, *ACS Nano*, 2017, **11**, 3081-3088.

208. P. Li, X. Zhang, and J. Liu, Aligned Single-Walled Carbon Nanotube Arrays from Rhodium Catalysts with Unexpected Diameter Uniformity Independent of the Catalyst Size and Growth Temperature, *Chem. Mater.*, 2016, **28**, 870-875.

209. S. C. Zhang, L. M. Tong, Y. Hu, L. X. Kang, and J. Zhang, Diameter-Specific Growth of Semiconducting Swnt Arrays Using Uniform Mo2c Solid Catalyst, *J. Am. Chem. Soc.*, 2015, **137**, 8904-8907.

210. S. Sakurai, H. Nishino, D. N. Futaba, S. Yasuda, T. Yamada, A. Maigne, Y. Matsuo, E. Nakamura, M. Yumura, and K. Hata, Role of Subsurface Diffusion and Ostwald Ripening in Catalyst Formation for Single-Walled Carbon Nanotube Forest Growth, *J. Am. Chem. Soc.*, 2012, **134**, 2148-2153.

211. D. B. Geohegan, A. A. Puretzky, J. J. Jackson, C. M. Rouleau, G. Eres, and K. L. More, Flux-Dependent Growth Kinetics and Diameter Selectivity in Single-Wall Carbon Nanotube Arrays, *ACS Nano*, 2011, **5**, 8311-8321.

212. S. Kang, M. Herzberg, D. F. Rodrigues, and M. Elimelech, Antibacterial Effects of Carbon Nanotubes: Size Does Matter, *Langmuir*, 2008, **24**, 6409-6413.

213. M. Zheng, A. Jagota, M. S. Strano, A. P. Santos, P. Barone, S. G. Chou, B. A. Diner, M. S. Dresselhaus, R. S. McLean, G. B. Onoa, G. G. Samsonidze, E. D. Semke, M. Usrey, and D. J. Walls, Structure-Based Carbon Nanotube Sorting by Sequence-Dependent DNA Assembly, *Science*, 2003, **302**, 1545-1548.

214. S. Park, M. Vosguerichian, and Z. A. Bao, A Review of Fabrication and Applications of Carbon Nanotube Film-Based Flexible Electronics, *Nanoscale*, 2013, **5**, 1727-1752.

215. P. Avouris, M. Freitag, and V. Perebeinos, Carbon-Nanotube Photonics and Optoelectronics, *Nat. Photonics*, 2008, **2**, 341-350.

216. P. Avouris, J. Appenzeller, R. Martel, and S. J. Wind, Carbon Nanotube Electronics, *Proc. IEEE*, 2003, **91**, 1772-1784.

217. S. J. Han, T. K. Yu, J. Park, B. Koo, J. Joo, T. Hyeon, S. Hong, and J. Im, Diameter-Controlled Synthesis of Discrete and Uniform-Sized Single-Walled Carbon Nanotubes Using Monodisperse Iron Oxide Nanoparticles Embedded in Zirconia Nanoparticle Arrays as Catalysts, *J. Phys. Chem. B*, 2004, **108**, 8091-8095.

218. Y. M. Li, W. Kim, Y. G. Zhang, M. Rolandi, D. W. Wang, and H. J. Dai, Growth of Single-Walled Carbon Nanotubes from Discrete Catalytic Nanoparticles of Various Sizes, *J. Phys. Chem. B*, 2001, **105**, 11424-11431.

219. A. Douglas, N. Muralidharan, R. Carter, and C. L. Pint, Sustainable Capture and Conversion of Carbon Dioxide into Valuable Multiwalled Carbon Nanotubes Using Metal Scrap Materials, *ACS Sustain. Chem. Eng.*, 2017, **5**, 7104-7110.

220. B. Kaplan, H. Groult, S. Komaba, N. Kumagai, and F. Lantelme, Synthesis of Nanostructured Carbon Material by Electroreduction in Fused Alkali Carbonates, *Chem. Lett.*, 2001, **7**, 714-715.

221. H. Y. Yin, X. H. Mao, D. Y. Tang, W. Xiao, L. R. Xing, H. Zhu, D. H. Wang, and D. R. Sadoway, Capture and Electrochemical Conversion of Co2 to Value-Added Carbon and Oxygen by Molten Salt Electrolysis, *Energ. Environ. Sci.*, 2013, **6**, 1538-1545.

222. F. Cervantes-Sodi, T. P. McNicholas, J. G. Simmons, J. Liu, G. Csanyi, A. C. Ferrari, and S. Curtarolo, Viscous State Effect on the Activity of Fe Nanocatalysts, *ACS Nano*, 2010, **4**, 6950-6956.

223. D. M. Tang, C. Liu, W. J. Yu, L. L. Zhang, P. X. Hou, J. C. Li, F. Li, Y. Bando, D. Golberg, and H. M. Cheng, Structural Changes in Iron Oxide and Gold Catalysts During Nucleation of Carbon Nanotubes Studied by in Situ Transmission Electron Microscopy, *ACS Nano*, 2014, **8**, 292-301.

224. K. Hata, D. N. Futaba, K. Mizuno, T. Namai, M. Yumura, and S. Iijima, Water-Assisted Highly Efficient Synthesis of Impurity-Free Single-Walled Carbon Nanotubes, *Science*, 2004, **306**, 1362-1364.

225. Y. H. Miyauchi, S. H. Chiashi, Y. Murakami, Y. Hayashida, and S. Maruyama, Fluorescence Spectroscopy of Single-Walled Carbon Nanotubes Synthesized from Alcohol, *Chem. Phys. Lett.*, 2004, **387**, 198-203.

226. C. L. Pint, S. M. Kim, E. A. Stach, and R. H. Hauge, Rapid and Scalable Reduction of Dense Surface-Supported Metal-Oxide Catalyst with Hydrazine Vapor, *ACS Nano*, 2009, **3**, 1897-1905.

227. C. H. See, and A. T. Harris, A Review of Carbon Nanotube Synthesis Via Fluidized-Bed Chemical Vapor Deposition, *Ind. Eng. Chem. Res.*, 2007, **46**, 997-1012.

228. E. Lamouroux, P. Serp, and P. Kalck, Catalytic Routes Towards Single Wall Carbon Nanotubes, *Cat. Rev. Sci. Eng.*, 2007, **49**, 341-405.

229. D. L. Plata, A. J. Hart, C. M. Reddy, and P. M. Gschwend, Early Evaluation of Potential Environmental Impacts of Carbon Nanotube Synthesis by Chemical Vapor Deposition, *Env. Sci. Technol.*, 2009, **43**, 8367-8373.

230. D. L. Plata, P. M. Gschwend, and C. M. Reddy, Envr 187-Coproducts of Carbon Nanotube Synthesis: Emerging Contaminants Associated with the Nanomaterial Revolution, *Abstr. Pap. Am. Chem. S*, 2007, **234**.

231. W. B. Shi, K. Xue, E. R. Meshot, and D. L. Plata, The Carbon Nanotube Formation Parameter Space: Data Mining and Mechanistic Understanding for Efficient Resource Use, *Green Chem.*, 2017, **19**, 3787-3800.

232. P. Zhai, J. A. Isaacs, and M. J. Eckelman, Net Energy Benefits of Carbon Nanotube Applications, *Appl. Energy*, 2016, **173**, 624-634.

233. *Environmental Protection Agency Inventory of U.S. Greenhouse Gas Emissions and Sinks*, 2019.

234. C. Samaras, and K. Meisterling, Life Cycle Assessment of Greenhouse Gas Emissions from Plug-in Hybrid Vehicles: Implications for Policy, *Environ. Sci. Technol.*, 2008, **42**, 3170-3176.

235. N. Lewis, Powering the Planet: The Future of Energy in the World, *Abstr. Pap. Am. Chem. S.*, 2014, **247**.

236. B. Scrosati, and J. Garche, Lithium Batteries: Status, Prospects and Future, *J. Power Sources*, 2010, **195**, 2419-2430.

237. J. B. Goodenough, and Y. Kim, Challenges for Rechargeable Li Batteries, *Chem. Mater.*, 2010, **22**, 587-603.

238. B. Nykvist, and M. Nilsson, Rapidly Falling Costs of Battery Packs for Electric Vehicles, *Nat. Clim. Change*, 2015, **5**, 329-332.

239. H. Hao, Z. X. Mu, S. H. Jiang, Z. W. Liu, and F. Q. Zhao, Ghg Emissions from the Production of Lithium-Ion Batteries for Electric Vehicles in China, *Sustainability*, 2017, **9**.

240. G. Majeau-Bettez, T. R. Hawkins, and A. H. Stromman, Life Cycle Environmental Assessment of Lithium-Ion and Nickel Metal Hydride Batteries for Plug-in Hybrid and Battery Electric Vehicles, *Environ. Sci. Technol.*, 2011, **45**, 4548-4554.

241. P. Poizot, and F. Dolhem, Clean Energy New Deal for a Sustainable World: From Non-Co2 Generating Energy Sources to Greener Electrochemical Storage Devices, *Energy Environ. Sci.*, 2011, **4**, 2003-2019.

242. J. Dewulf, G. Van der Vorst, K. Denturck, H. Van Langenhove, W. Ghyoot, J. Tytgat, and K. Vandeputte, Recycling Rechargeable Lithium Ion Batteries: Critical Analysis of Natural Resource Savings, *Resour. Conserv. Recycl.*, 2010, **54**, 229-234.

243. M. Zackrisson, L. Avellan, and J. Orlenius, Life Cycle Assessment of Lithium-Ion Batteries for Plug-in Hybrid Electric Vehicles - Critical Issues, *J. Clean. Prod.*, 2010, **18**, 1519-1529.

244. M. Armand, and J. M. Tarascon, Building Better Batteries, *Nature*, 2008, **451**, 652-657.

245. *Amnesty International, Time to Recharge: Corporate Action and Inaction to Tackle Abuses in the Cobalt Supply Chain*, 2017.

246. P. Whoriskey, *In Your Phone, in Their Air*, 2016.

247. K. Moyer, R. Carter, T. Hanken, A. Douglas, L. Oakes, and C. L. Pint, Electrophoretic Deposition of Lifepo4 onto 3-D Current Collectors for High Areal Loading Battery Cathodes, *Mater. Sci. Eng. B*, 2019, just accepted.

248. A. Douglas, R. Carter, M. Y. Li, and C. L. Pint, Toward Small-Diameter Carbon Nanotubes Synthesized from Captured Carbon Dioxide: Critical Role of Catalyst Coarsening, *ACS Appl. Mater. Int.*, 2018, **10**, 19010-19018.

249. *International Energy Agency Global Ev Outlook 2018*, 2018.

250. *U.S. Energy Information Administration Annual Energy Outlook 2019*, 2019.